IMT School for Advanced Studies, Lucca

Lucca, Italy

Surface roughness genomics in contact mechanics

A new method enabling roughness design towards surface prototyping

PhD Program in
INSTITUTIONS, MARKETS AND TECHNOLOGIES
Curriculum in Computational Mechanics

XXX Cycle

By

Paolo Cinat

2018

The dissertation of Paolo Cinat is approved.

Program Coordinator: Prof. Marco Paggi, IMT School for Advanced Studies Lucca

Supervisor: Prof. Marco Paggi, IMT School for Advanced Studies Lucca

Supervisor: -, -

Tutor: Prof. Marco Paggi, IMT School for Advanced Studies Lucca

The dissertation of Paolo Cinat has been reviewed by:

Prof. A. Almqvist, Luleå - University of Technology

Prof. A. Popp, University of the Bundeswehr Munich

IMT School for Advanced Studies, Lucca

2018

To my *father Antonio*,
i felt you by my side
during these three years.

Contents

List of Figures

List of Tables

Acknowledgements

The research presented in this work was carried out at the MUSAM Lab in IMT School for Advanced Studies, Lucca. The research related to this PhD Thesis has received funding from the European Research Council under the European Union's Seventh Framework Program (FP/2007–2013)/ERC Grant Agreement No. 306622 (ERC Starting Grant Multi-field and Multi-scale Computational Approach to Design and Durability of PhotoVoltaic Modules – CA2PVM).

First and foremost, I am grateful to my supervisor, Prof. Marco Paggi, for providing me the opportunity of this work. His support and ideas are the heart of this thesis. He always shown interest in my work and provided my the platform to interact with other important researcher as Vladislav Yastrebov and his PhD students Andrei Shvartz, with whom i spent a very nice and productive period as visiting in the Centre of Materiaux. I want to spend my last acknowledge to Claudia Borri and Giorgio Gnecco to take part of my work.

I am honored to have know Prof. Bemporad and to have worked with his collaborator Daniele Bernardini during my first year at IMT.

I am also grateful to my sister Michela and my girlfriend Rosaria, my aunts Isabella and Maria-Grazia, my uncle Franco and Giampaolo. They all support me during this five years at IMT. Finally, i want to thank also my mother that I know she loved me well, though in her own way.

Vita

1st September, 1985	Pisa (Pisa), Italy
2009	Bachelor degree in Aerospace engineering Final mark: 100/110 Università degli Studi di Pisa, Italy
2012	Master degree in Aerospace engineering Final mark: 102/110 Università degli Studi di Pisa, Italy

Publications

1. Cinat P., Paggi M. "Percolation proprieties of the free volume generated by two rough surfaces in contact below the full contact limit", *Conference Proceedings of the ECCOMAS 2016* in Crete Island (GRE), vol. 1, pp. 1850-1855, 2016
2. Cinat P., Paggi M. "Simulation of fluid flow across rough surfaces in contact", *Conference Proceedings of the YIC-GACM 2015* in Aachen (GER), vol. 1, pp. 59-63, 2015

Presentations

1. "Surface roughness genomics" at *International Conference of Computational Contact Mechanics ICCCM 2017*, Lecce (ITA), 2017
2. "Percolation proprieties of the free volume generated by two rough surfaces in contact below the full contact limit" at *ECCOMAS 2016*, Creta (GRE), 2016
3. "Simulation of fluid flow across rough surfaces in contact", at *ECCOMAS YIC-GACM 2015*, Aachen (GER), 2015
4. "HighTissue project", at *IMT Scuola Alti Studi Lucca*, 2015

Abstract

In actual age of Industry 4.0, the miniaturization of mechanical components is becoming extremely sophisticated, thanks to enhancing techniques such as additive manufacturing technologies. This requires an efficient description of multi-scale roughness to properly characterize the interface contact problem.In this dissertation, a new approach called *surface roughness genomics* is proposed to uniquely characterize surfaces at different length scales, from the topological point of view. Similar to biological systems, where the biological information is encoded in DNA base pairs, surface roughness is decomposed in elementary waves, whose unique ensemble is the *surface genome*. The identification process of the real surfaces genome, the *sequencing* procedure, is based on the solution of a constrained convex optimization problem. A rough profile (*chromosome*), collecting the features of roughness at a fixed length-scale is isolated from the surface genome So, a rough profile is reconstructed by summing up subsequent chromosomes. The top-down and bottom-up approaches are pursued to reconstruct a rough profile, to quantify the role of specific multi-scale features in the frictional normal contact problem. New algorithms are then proposed to generate roughness morphology achieving a target mechanical response, enabling surface prototyping towards morphology real time control.Beside the mechanical contact problem, the fluid sealing between contacting bodiesis herein investigated by proposing a simple algorithm and applying it to a set of fractal rough surfaces. This algorithm evaluates the free networks involved in leakage process, considering different normal contact indentations at various surface resolutions.

Chapter 1

Introduction

In this Chapter the role of contact in technology is introduced. Particular attention is then given to the morphology of surface roughness, that determine the mechanical features of contact. The third Section introduces the main idea behind the research project presented in this work, which is structured as detailed in the last Section.

1.1 Contact problems in technology

The new trend characterizing the current era of Industry 4.0 is radically changing perspectives of industries about the technological manufacturing of components or materials and for cyber-systems, as described by Brettel et al. [2014] and Wang et al. [2015]. The role of boundary between material constituents/phases becomes progressively dominant over the one of bulk properties, thanks to the increasing trend in miniaturization of components and the significant progress in the design of mechanical systems and materials starting from the sub-micrometre scale.

Furthermore, the improving of resources in the current age of Industry 4.0, such us additive manufacturing technologies (Excell [2013]; Taufik and Jain [2014]), are promoting a detailed and unified specific description of roughness over different length scales, to enable rapid manufacturing and morphology in-line control of mechanical components,

as performed by Bora et al. [2005] or Almuramady and Borodich [2017] in the case of MEMS. Contacting surfaces are never flat and present different roughness organizations over multiple scales of observation. This aspect is fundamental during the realization of mechanical components, leading to different modeling of the inherent problem.

For car tires, contact is compulsory to guarantee grip on the road. At the same time partial contact with free gaps is required to guarantee a sufficient drainage of water in case of heavy rain, leading to the pioneering research of Persson [2001] for this coupled problem.

In bearings, contact is necessary to ensure both a good lubrication and to maintain the lubricating oil into the system, without any leakage. This problem requires a good estimation of the leak rate, that involves particular physical quantities to be considered according to the problem size. In small applications, Almqvist et al. [2014] implemented a simple but very efficient model to consider the pressure recovery in journal bearings of a cavitating fluid. With regard to bearings for larger-scales applications, such us railway or avionic shafts, more specific model are needed such the one propose by Fillon et al. [2015] that consider also thermal effects to simulate this system and improve its efficiency.

Also, green energy applications requires different analysis on the role of roughness according to the scale of the problem. In flexible photovoltaic panels the diffusion of moisture or the propagation of superficial cracks at small length scales is investigated to assure durability (see Borri et al. [2017]). Innovative green applications, such as the novel wave energy converter "Ocean Grazer" proposed by University of Groningen, requires a specific design of contacting components to assure a competitiveness in the energy market (Vakis et al. [2014]; Van Roij et al. [2015]).

Today the design of a material micro-structure to achieve a prescribed mechanical response is feasible using the progress in computational methods. In many industrial applications, even simplified rules of mixtures can be used to provide a practical guideline to design of heterogeneous material components such as fiber reinforced or laminated composites.

Some explicative example can be found in the works of Reinoso et al. [2012]; Paggi and Reinoso [2015]; Reinoso et al. [2016]; Carollo et al. [2017], where the mechanical behavior during fracture of these kind of material is considered.

Indeed, the same does not apply to surface roughness. The question on how to design a surface morphology to achieve a prescribed response is a much more complex problem. The reason relies on the fact that the mechanical response is a collective property emerging from the nonlinear interplay of roughness over multiple scales. Therefore, the inverse problem, i.e., define the surface morphology to match a desired emergent response, is not a trivial task by mimicking nature or by parametric studies, as illustrated in Fig. 1.

In some cases, it is well-established that roughness and/or texturing play a beneficial role. For example, Sherge and Gorb [2001] boosted the adhesion effects in adhesives by mimicking the micro-structure of Geko pads. Further, Nosonovsky [2007] and Borri and Paggi [2015] successful attempted to create artificial super-hydrophobic interfaces inspired by Lotus' leaves. Another example was given by the work of Yin et al. [2012], who used dimple-textured interfaces to guarantee better lubrication in diesel-engine.

(a) Sherge and Gorb, 2001 (b) Bushan, 2009 (c) Lucchini et al., 2015

Figure 1: Successful examples of manufactured rough surfaces to achieve desired emergent properties: (a) Sherge and Gorb [2001] manufact super adhesive interfaces, mimicking the Gecko pads; (b) Bhushan [2009] reproduced the skin of a shark to reduce drag in windmill blades; (c) innovative sensors are proposed by Lucchini et al. [2015] forcing surface instabilities.

However, certain forms of roughness could limit the tribological performance of a joint as studied by Zhao et al. [2014] on the interface fracture produced by increasing frictional effects. Another example is provided by Reinoso et al. [2016], who investigated fracture process in thermal barrier coatings bonded to a rough interfaces. The counter effects of roughness in some applications might be reduced by in-field experiments or/and numerical investigations. For example, Vakis [2009] discovered that light contact enable surfing recording in hard-disks.

Nevertheless, the majority of approaches pursued so far to investigate the role of roughness always depart from a surface given as an input. If this surface is acquired by experimental techniques, the generalization of any experimentally measured or simulated emergent property should be attempted with care, since it might be specimen dependent, as investigated by Wendt et al. [2002], Zavarise et al. [2007] and Yastrebov et al. [2015], among others. Alternatively, model surfaces can be numerically generated to satisfy prescribed statistical distributions, or with selected spectral features to represent possible forms of known roughness, see Borri and Paggi [2015]. Also, the parametric study of the mechanical response can provide some interesting insight into the role of roughness, see Vakis [2009]. However, deviations from ideal surface models can play an important role, as recently pinpointed by Paggi and Barber [2011] for thermal and electric contact conductance or by Ciavarella et al. [2017] for the adhesive response of rough spheres.

Regarding the methodology to assess emergent properties of surfaces, the multi-scale characterization of roughness have been addressed according to the state-of-technology of developing period. Greenwood and Williamson [1966] (GW) and Persson [2001] proposed two different approximation of the interface to describe the elastic stress transfer between two bodies in contact. Ciavarella et al. [2008] enriched the GW model introducing asperities interaction. Later on, Paggi and Ciavarella [2010] emphasized these interactions focusing on the statistical properties and the Gaussianity of the height field distribution. Barber [2003] enriched

this model by introducing the thermal and electric contact conductance and other important authors, such as Ciavarella and Demelio [2006] and Paggi and Barber [2011], discussed on their application. Frictional effects in statics and dynamics have been introduced by Nosonovsky and Bushan [2008]. Nosonovsky and Bushan [2008] and Zavarise et al. [2007] emphasized the collective non-linear interaction of multi-scale roughness and a particular attention was given to its effect on the macroscopic performance of interfaces.

The analytical methods described in the above are just some examples of tribological emergent properties, which are detectable also by experimental investigations. Rubinstein et al. [2004] proposed experimental methods about the frictional dynamic response of contacting bodies. Bandis et al. [1981] investigated the real contact area distribution, meanwhile the studies of Lorenz and Persson [2009] concerned on the fluid percolation and leakage. The increasing technologies also overcome some criticism highlighted by Wendt et al. [2002] in the topology acquisition of rough surfaces, even if not all the materials can be still tested since the proper acquisition technique requirer transparency to visualize the interface. However, the inherent technical complexity and costs of the equipment are natural limits of the experimental approach.

Numerical methods have therefore a great potential and they are frequently used, see Yastrebov [2013] for a general overview. Finite Element Methods (FEM) (Anciaux and Molinari [2009]) and/or molecular dynamics methods (Campana and Muser [2006]) allow an accurate problem description, but they are heavy fro a computational point of view. Boundary Element Methods (BEM) are more light computationally speaking but the modeling is limited to the frictionless normal elastic cases(Bemporad and Paggi [2015]), or to coupled problem with adhesion (Pohrt and Popov [2014]). Mortar finite methods provide reliable discretization of interface effects, especially in 3D problems dominated by the scenario hierarchy , such as unilateral contact, friction, thermomechanical interfaces and wear (see Popp et al. [2009]; Popp [2012]).

1.2 The role of surface roughness in contact mechanics

The macroscopic performance of the surface ensemble is a collective emergent property arising from the complex interaction of the multi-scale organization of roughness, that determines the surface morphology. Sayles and Thomas [1978] noticed that surfaces present *self-similar* organization of roughness at different length scales, according to the classical fractal theory as showed later by Mandelbrot [1982] and Peitgen and Saupe [1988]. Later on, Berry and Lewis [1980] and Wu [2001] related the multi-scale behavior of fractal surfaces with a power law function of their power spectral density (PSD) function, expressed by the fractal dimension D. For a given acquisition, this power-law ranges in a wavelength domain is bounded by the lower cut-off frequency ω_ℓ, function of the sampling length L, and the upper cut-off frequency ω_u, function of the sampling interval δ. Actual studies by Bottiglione et al. [2009a] and Persson [2014] demonstrated that almost all real surfaces have a fractal dimension less than 2.5.

Different roughness organization are observed by refining the observation, and it is not always self-similar as for fractals, see Fig. 2 for the Ginko Biloba leaf. This image is referenced to the work of Borri and Paggi [2016], an it is taken using the scanning electron microscope (SEM) Zeiss EVO MA15 available in the laboratory of the research unit MUSAM at the IMT School for Advanced Studies in Lucca.

The images in Fig. 2 were taken in variable pressure, hence the leaf surface was neither metallized, nor graphitized, to preserve its surface properties. Superficial channels of the leaf, that have the function to convey water, are easily seen at low magnification ($60\times$, Fig. 2(a)) and they are not visible anymore by increasing the resolution ($1000\times$, Fig. 2(b)). At this scale, roughness is organized as a set of smaller and smoother asperities that constitutes a new order of organization (Fig. 2(c)).

The Ginkgo Biloba leaf is a very good example of a natural surface with a structural hierarchy characterized by at least three different microstructures. Borri and Paggi [2016] proposed an accurate description of its statistical and fractal properties, according th the pioneering work of Nayak [1971], revised by Greenwood [2006]. They conclude that Random Process theory (see Sayles and Thomas [1978]; Mandelbrot [1982]; Peitgen and Saupe [1988]) cannot fully describe the complex statistical distributions of natural hydrophobic surfaces. Similar limitations have been highlighted for the issue of fractal by Borodich and Mosolov [1992] in different scenarios such as the description of multi-scale roughness (Borodich and Onishchenko [1999]; Borodich et al. [2016]), fractured interfaces (Borodich [1997]) or bio-adhesives Borodich and Savencu [2016].

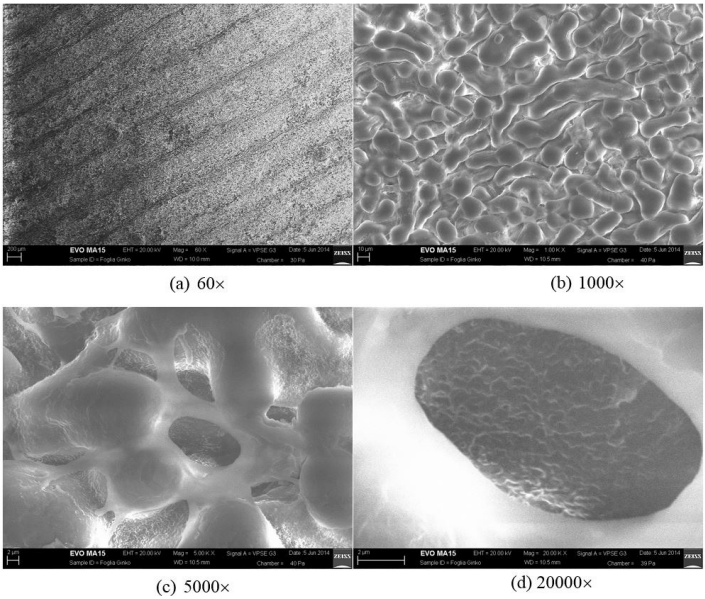

Figure 2: SEM images of a Ginkgo Biloba leaf VPSE 20kV: (a) 60x, (b) 1000x, (c) 5000x, (d) 20000x. Different organization of height can be observed. Courtesy of Borri and Paggi [2016].

The morphology of surface roughness determines the interaction between two contacting bodies. The morphologies of such is such that they lead to *non-conforming* contact when pressed together, i.e., the shapes of the bodies are dissimilar enough that, under zero load, they only touch at a point (see Barber [2010]). The contact area is small compared to the objects size and the stresses are highly concentrated in this area. The mechanical response is determined by many effects, which take place at different length scales (Borodich and Onishchenko [1999]; Borri-Brunetto et al. [1999]). Examining the coupled problem with fluids, network channels generated by hydraulic fracturing, sealing and leakage in mechanical components are just some problems governed by multi-scale surface roughness as investigated by Borri-Brunetto et al. [1999], Bottiglione et al. [2009a], Bottiglione et al. [2009b] and Borri-Brunetto et al. [2001]. In both scenarios, the control the percolating and non-percolating subdomains of free volume generate by the multi-scale roughness characterizing these contacting interfaces is pursued using a specific sealing materials or the application of a squeezing load.

The focus of the current research is to determine the effect of the multi-scale roughness on the main mechanical quantities governing the contact response between rough surfaces. The real contact area, A_r, which is a fraction of the nominal one that would be observed if the surfaces were totally flat, A_0, plays an important role from the mechanical point of view. As surfaces are never ideally flat, asperities (3D maxima of the surface) determine the real contact area for a given normal load p, that is the integral of the local pressure distribution $\sigma_z(x, y)$ over the asperity contact areas:

$$p = \int_{A_r} \sigma_z(x, y) dA \tag{1.1}$$

The connection among the elevation of asperity distribution, the spatial asperity distribution and the pressure distribution is crucial to determine the mechanical response of a rough surface. The deformation induced by the distribution of contact stresses leads to asperities coalescence, determining consistent morphological evolution of the surface during contact.

Recently, Yastrebov et al. [2012] and Dapp and Muser [2015] investigated this coalescence, focusing ton the characterization of the critical section of this free doman, whose morphology it the one of a *saddle point*. As a matter of fact, also leakage and percolation are influenced by this deformation. The gap between surfaces in contact characterizes a free volume V, as detailed by Paggi and He [2015] considering the effect of D and multiple resolutions. A fluid can leak according to the network of channels composing this free volume. Non-communicating channels or voids identifies a sub-domain of this network, the trapped volume V_t, that depends on the percolation properties of the overall. Percolation and leakage depend also on the fluid flow, but for low Reynolds numbers, which is the case for low pressure differences throughout the channels, transient and turbulent phenomena can be considered negligible and the network topology is the most important feature for the characterization of a seal. See, for further details, Bottiglione et al. [2009a], Cinat and Paggi [2015], Kloppel et al. [2011], Pérez-Ràfols et al. [2016a], Pérez-Ràfols et al. [2016b].

The accurate identification of the pressure distribution is fundamental to predict the leak rate, as shown by many authors as Bottiglione et al. [2009a,b]; Dapp et al. [2012]; Lorenz and Persson [2009]; Persson [2001]; Yastrebov et al. [2015]. In this framework, the Persson's theory of leakage Persson [2001] for fractal rough surfaces was pioneering. The surrounding idea beyond of Persson's theory, presented in Fig. 3, is to express the leak-rate as a function of the pressure distribution p_f, i.e. $q = q(p_f, \zeta)$, where $\zeta = \frac{L}{\delta}$ is the surface resolution.

According to Persson's assumptions, the real contact area A_r is related to the pressure distribution by a diffusive relation specifically holding for the full contact regime, thus avoiding the need of invoking the statistical parameters of the surface as routinely needed for partial contact as demonstrated by Mannners and Greenwood [2006]. Zavarise et al. [2007] over-viewed the resolution influence of statistical parameters, given by the specimen length L and the resolution adopted δ, in

contact models, observing different dependencies of the bearing area and pressure distribution evolutions during contact considering different resolution of the same surface. Moreover, recently, Yastrebov et al. [2017a] used a topology preserving smoothing technique, which improves the appearance of contact clusters morphology and he concluded that, generally, numerical methods overestimate the contact area value and then a comprehensive and detailed study is need to clarify the identification of the contact area, as the one performed recently by Solhjoo and Vakis [2015] by using atomistic models.

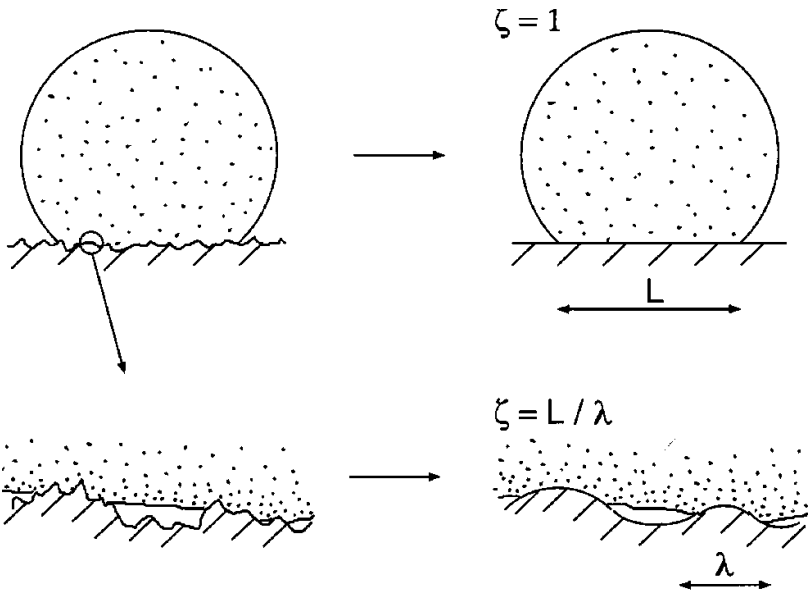

Figure 3: The first image used by Persson [2001] to describe his pioneering theory *"A rubber ball squeezed against a hard, rough, substrate. Left: the system at two different magnifications. Right: the area of contact $A(\lambda)$ on the length scale λ is defined as the area of real contact when the surface roughness on shorter length scales than λ has been removed (i.e., the surface has been "smoothed" on length scales shorter than λ)."*.

Persson's theory contradicts contact models whose predictions relies on micro-mechanical contact theories specific for partial contact as Greenwood and Tripp [1970] and Bush et al. [1975] ones, for which the summit distribution and the shape of asperities play an important role in the contact response. The striking difference between these two lines of research led to a series of investigations from the infinitesimal to the full contact regime Bottiglione et al. [2009b]; Paggi and Ciavarella [2010]; Yastrebov et al. [2015], with an attempt to relate contact predictions to the statistical properties of the undeformed rough surface with a power-law PSD function, proposing corrections to Persson's theory for partial contact applications as done by Yastrebov et al. [2015] that corrects its prediction with the Nayak [1971] parameter α for light pressure contact regime. On this line, corrections to the Greenwood and Williamson [1966] model have been proposed, enriching it with asperities effect by numerical iteration as proposed by different authors Ciavarella et al. [2008]; Paggi and Barber [2011]. These interaction are either introduced statistically by Vakis [2014], who corrected the relative displacement by a coefficient related to the statistical properties of the surface.

A similar approach was proposed by Greenwood et al. [2011], without taking into account the statistical distribution. The results proposed by Vakis [2014] has been also recently extended to the elasto-plastic case by Song et al. [2017], demonstrating that the mechanical response between contacting rough interfaces is affected by the material's plastic properties and by the size of asperities. The reliability of these two approaches to predict the frictionless elastic interaction focused the research interest of many authors, and a final seems to find a conclusion step in the contact mechanics challenge proposed by Muser et al. [2017].

Beside this observations on the connection between pressure distribution and contact area evolution, Persson also noticed that also the evolution of leakage can be treated as percolation phenomena, with a diffusion of information from the saturated domain (in contact) to the unsaturated one (not in contact), with increasing the resolution. As a result, leakage is usually absent for a very coarse surface resolution, while it takes places by refining the surface topology above a certain threshold.

Dapp et al. [2012] found that this resolution threshold correspond to a ratio between the real contact area and the nominal one, i.e., $A^* = A_r/A_0$. To investigate this relation, Dapp et al. [2012] observed that the lower cut-off frequency ω_ℓ of the rough surface mainly affects the topology of the free volume and, consequently, leakage characteristics as highlighted by Bottiglione et al. [2009a] by multi-scale observation of roughness. At the end, Dapp et al. [2012] founded a threshold level for leakage of $A^* = 0.5$ following this approach. At the opposite, Putignano et al. [2013] demonstrated that for elastic contact fluid can percolate for $A^* < 0.5$, by investigated numerically a set of surfaces with different statistical properties Putignano et al. [2012a,b].

1.3 Aims of the present research

The aim of this dissertation is to propose a revolutionary methodology, which is called *surface roughness genomics*, to create a framework combining experimental-theoretical-numerical approaches to investigate unexplored forms of surface roughness, characterize them from the physico-mechanical points of view, identify emergent responses and recursive patterns, and finally allow the production of demonstrators by additive manufacturing technologies.

Surface roughness genomics aims at uniquely characterize the morphology surfaces by following the methodology proposed in Fig. 4. The focus of this dissertation is on arguments framed in blue.

As biological informations are encoded in DNA base pairs, the multi-scale geometrical features of surface roughness is decomposed in its constituents, practically a string of coefficients, called *surface genome*, via a procedure called *sequencing*. Consequently, it is possible to isolate the features at a given length scale in a elementary waves named *chromosomes*. The interaction of chromosomes identifying different lenght scales determines the mechanical response of a surface. Thus, the acquisition of a database of genomes is a fundamental step to give a mechanical multi-scale characterization of roughness. The *cross-over* of genetic features of

different surfaces, leads to innovative or desired surface morphologies (new genomes), designed to achieve target emergent properties by tailoring interface roughness. This methodology is herein developed by integrating computational contact and optimization algorithms.

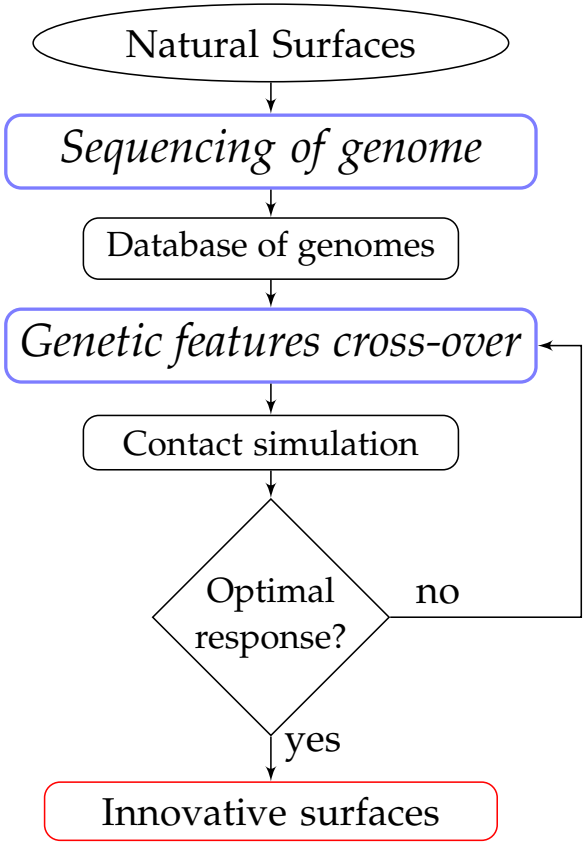

Figure 4: The work-flow of *Surface roughness genomics*, the methodology proposed in this dissertation. The *genome sequencing* will be addressed in Chapter 3, whereas the genome cross-over to design new form of roughness, i.e. new genomes, achieving a target mechanical response will be presented in Chapter 4.

This innovative tool will be essential to answer fundamental questions such as: how many levels of roughness of a natural surface are really necessary to be replicated such that the artificial one has the same response? Are there any relevant genome appearing in some classes of natural (biological) or artificial (induced by machining techniques) rough surfaces? How should we compose a surface when the simultaneous optimization of multiple emergent properties is requested?

1.4 Outline of the dissertation

This dissertation is structured as follows. **Chapter 2** addresses the fundamental methods of contact mechanics used in this work, starting from the generation of rough surfaces and the fundamentals of the boundary element method (BEM), to solve the frictionless normal contact problem. Dimensionless quantities are then summarized, useful synthetically characterize the contact response of rough surfaces.

The leakage in the free volume between rough surfaces in contact is also considered, starting from the pioneering Reynolds equation for the fluid motion in thin films. Those methods are illustrated in relation to a discussion on the coupling between fluid flow and contact mechanics.

Finally, an iterative algorithm is proposed with the aim at investigating the network of channel of the free volume. Particular attention is given to the change of morphology during compenetration, to investigating their percolating and non-percolating features.

The fundamental definitions of surface roughness genomics will be given in **Chapter 3**. The characterization of a single length scales of roughness will be discussed. The definition of chromosome will enable the reconstruction of roughness over multiple length scales by superimposition of them. Among all the possible methods to select individual waves to superimpose, the comparison will be on two different process, the top-down and the bottom-up superimposition approaches, clarifing the different outcome by pursuing these multi-scale techniques.

Then, it will be illustrated the first key step of this new approach, the sequencing of genomes from rough profiles, that leads to the identification of all the coefficients, namely genes, characterizing the features of roughness over multiple scales of observation. The sequencing of genomes is formulated as a constrained convex optimization problem, to be solved with efficient quadratic programming algorithms.

Finally, sequencing will be proved with an artificial rough profile and then it will is applied to a natural rough profile extracted from a fracture surface of steel alloy. The top-down and bottom-up superimposition approaches will be compared to give a first insight into the mechanical interaction of multi-scale roughness features.

Chapter 4 will be focused on the mechanical interaction of multi-scale roughness, to address and prove the cross-over of surface genetic features towards roughness prototyping. To determine the morphological features of a known rough profile, chromosomes determining the stiffness-load curve will be selected to distinguish between macro- and micro- scale of roughness.

Three different approaches to obtain new genomes achieving a target mechanical response will be discussed. The new genomes so obtained are not supposed to be again fractal, that could be just seen as a special class of them. The first methods optimizes the values of genes related to a rough profile. The second method cross-over the complete genome of two profiles, both providing a mechanical response closer to the target one in specified intervals. The third method is similar to the genome cross-over, but it combines only the part of the genome giving the macro-scale roughness. Finally, a combined method to realize a profile satisfying two targets in two different mechanical responses will be presented.

The feasibility of these approaches will be illustrated in relation to exemplary case studies, confirming that it is possible to select particular features of roughness to obtained a specific mechanical response.

Conclusions and further development of this research are provided in **Chapter 5**.

Chapter 2

Numerical methods for contact mechanics

This section addresses the methods used to solve and characterize the contact mechanics problem in this work. Two different fractal-based methods to generate rough surfaces are illustrated: the Random Midpoint Displacement (RMD) algorithm and the Weierstrass-Mandelbrot function technique. Then, the frictionless normal contact problem between rough profiles and/or surfaces is addressed. The mathematical framework herein introduced is based on the boundary element method (BEM). The dimensionless quantity useful to characterize the contact response of rough surfaces are then presented, along with some practical examples.

The last part of this Chapter will be focused on the prediction of leakage in the free volume between rough surfaces in contact, starting from the definition of the Reynolds equation for the fluid motion of a thin film. A brief discussion on the coupling between the fluid motion and contact mechanics is given. At the end, an iterative algorithm is proposed to study the network of channels of the free volume between rough surfaces in contact. Particular attention is given to how the change in morphology of the contact area during contact affects the percolating properties.

2.1 Numerical generation of rough surfaces

2.1.1 Random Midpoint Displacement algorithm

Rough surfaces with fractal properties can be numerically generated according to the Random Midpoint Displacement (RMD) algorithm, proposed by Peitgen and Saupe [1988]. The RMD operating principle is illustrated in Fig. 5. Square surfaces with different resolutions can be generated by successively refining an initial mesh by a successive addition of a series of intermediate heights. A mid point in each square is generated, with elevation set equal to the mean values of the neighboring heights, plus a random number extracted from a Gaussian distribution with zero mean and rescaled variance $\sigma_1^2 = \sigma_0^2/2^{(3-D)/2}$, where $\sigma_0^2 = 1/\sqrt{0.09}$ and D is the surface fractal dimension ranging from 2 to 3. The refinement algorithm depends upon the parameter m, which is related to the number of heights per side of the square generated grid, $2^m + 1$. Given L the lateral size of the surface, the grid spacing is $\delta = L/2^m$ and the resolution can be defined as $\xi = 1/\delta$. The RMD algorithm allows the user to generate different surfaces with different height distributions and statistical features. Specifically, surfaces can be generated with different resolutions by acting on m or with different fractal dimension, D.

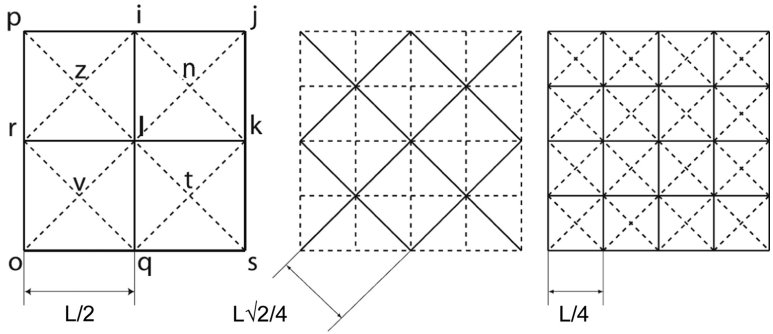

Figure 5: Operating principle of the Random Midpoint Algorithm (RMD), see Peitgen and Saupe [1988] and Paggi and He [2015].

2.1.2 The Weierstrass-Mandelbrot function technique

Mandelbrot [1977] proposed the Weierstrass-Mandelbrot function (WM), as an extension of the discrete Weierstrass series, to describe a stochastic process with a fractal behavior, see also Mandelbrot [1982, 1985]. The real part of the WM function is a geometric series of sinusoids, shifted by a random phase ϕ_k, whose discrete spectral density is ruled by the parameter γ:

$$\mathcal{W}(x) = A \sum_{k=-\infty}^{\infty} \gamma^{-Hk} \left[\cos(\phi_k) - \cos(\gamma^k x - \phi_k)\right]. \tag{2.1}$$

The frequencies amplitude is ruled by the parameter A and the Hurst coefficient $H \in [0, 1]$, that is complementary of the fractal dimension of the surface: $d + 1 = D + \mathcal{H}$, where d is the topological dimension of the profile/surface. For example, a rough surface has topological dimension $d = 2$. Berry and Lewis [1980], to compute the Hurst coefficient H, approximated the logarithmic expression of the discrete PSD spectrum given by Eq. (2.1) with a straight line.

From a real surfaces, a first rough estimation of the amplitude coefficient A ca be obtained according to the classical Nayak [1971] theory of roughness or by considering the value of the PSD function for a prescribed frequency as proposed and discussed by Majumbdar and Bhushan [1990] and Wang and Komvopoulos [1994a].

Regarding the density of the frequency spectrum, it was imposed strictly equal to $\gamma = 1.5$ by Malcai et al. [1997] and Anvir et al. [1998]. However, Borodich and Mosolov [1992]; Borodich et al. [2016] discussed the fact that other values could be identified in nature Borodich and Mosolov [1992]; Borodich et al. [2016]. The condition $\gamma = 1$ is a limiting case to obtain a discrete spectrum for both WM and MWM functions, since the geometrical series diverges.

The finiteness of a rough profile restricts the value of k over k between two integers, k_1 and k_2, see Majumbdar and Bhushan [1991]. The value of k_1 and k_2 are ruled by the discretization adopted by an instrument like a confocal profilometer or an atomistic microscope (AFM).

The WM function in Eq. (2.1) is often used to model stochastic processes with a self-similar behavior as noises or turbulence motion in fluid dynamics, see e.g. Mandelbrot [1977, 1982, 1985]; Versteeg and Malaskera [1995]. However, Eq. (2.1) is limited to modeling 2D fractal process, such as rough profiles as stated by Sayles and Thomas [1978]. So, Ausloos and Berman [1985] proposed to describe higher-dimensionally stochastic processes by generalizing the WM function to a multivariate version, the multivariate Weierstrass-Mandelbrot function (MWM):

$$\mathcal{Z}(\vec{x}) = \sqrt{\frac{\log(\gamma)}{M}} \sum_{m=1}^{M} A_m \times \tag{2.2}$$
$$\times \left\{ \sum_{k=-\infty}^{\infty} \gamma^{(1-k)H} \left[\cos(\phi_{m,k}) - \cos\left(\frac{2\pi}{\lambda} \gamma^{(k-1)} (\hat{\boldsymbol{n}}_m \cdot \vec{x}) + \phi_{m,k}\right) \right] \right\},$$

where, in the absence of a subscript, the notation $\log$ refers to the base 10 logarithm. The length λ defines a dominant frequency $q = \frac{2\pi}{\lambda}$ of the MWM spectrum, that reduces increasing k thanks to γ.

The MWM function in Eq. (2.2) is defined as a weighted, random superposition of M processes described by Eq. (2.1). These M ridges introduced by Ausloos and Berman [1985] in Eq. (2.2) have also a in-plane phase angle determined by the scalar product $\hat{\boldsymbol{n}}_m \cdot \vec{x}$.

In the case of roughness anisotropy, it is approximated in the MWM function assigning a different amplitude A_m of each ridges M, with $A_m = \tilde{a}_m A$. The value of coefficients $\tilde{a}_m$ is comprised between 0.85 and 1.15 for anisotropic surfaces, whereas $\tilde{a}_m = 1$ for isotropic surfaces (Wang and Komvopoulos [1994a]; Yan and Komvopoulos [1998]).

The real part Eq. (2.2) was considered representative of the majority of fractal surfaces showing a multi-scale behavior, for example by Wang and Komvopoulos [1994b]; Lopez et al. [1994]; Komvopoulos and Yan [1997]; Wu [2001]; Paggi and Ciavarella [2010]; Bora et al. [2005]. Many authors, such as Majumbdar and Bhushan [1990]; Wang and Komvopoulos [1994a]; Ciavarella et al. [2000]; Morag and Etsion [2007], used the real part of the multivariate MWM function to model the elasto-plastic contact of fractal profile. The observations given by the above authors on

the asperity deformation modeled with either Eq. (2.1) or Eq. (2.2) lead Greenwood and Wu [2001] to an apology regarding the formulation of its pioneering model (Greenwood and Williamson [1966]).

Contrary to those studies, Wu [2001]; Borodich et al. [2016] suggested that some model assumptions behind the MW and MWM functions are not always fully verified. Thus, the use of both WM and MWM functions has been widely questioned by many authors.

The analogy with a Brownian motion was immediately recognized by many authors, see e.g. Berry and Lewis [1980]; Mandelbrot [1982]; Ausloos and Berman [1985]. Lopez et al. [1994] investigated the theory behind the fractal characterization of real surfaces, demonstrating that the WM function has all the mathematical characteristics to describe a Brownian motion, whereas it does not properly match the stochastic features of a rough surface. This demonstration was addressed properly by Wu [2000], who observed that the MWM function is not a rigorous extension of the WM one, as it can be see by comparing their PSD. Also, Wu [2001] noticed that a profile extracted from an arbitrary section of the surface might not be a profile described by the WM function. However, Wu [2001] concluded that the MWM function gives a overall suitable representation of the multi-scale features of self-affine rough surfaces.

Among all the aforementioned studies, only Ciavarella et al. [2000] gathers the challenge to investigate the multi-scale behavior of Eq. (2.1), proposing a mathematical model to study the superimposition of pressure given by the MW function, considering the pioneering theory of Archard [1957] as base model. In following studies, Ciavarella et al. [2004] investigated the electrical conductance and the heat transfer of the MW profiles, proposing also a "re-vitalized" version of the GW model (Ciavarella and Demelio [2006]). However, Ciavarella et al. [2004], investigating the role of the contact stiffness, noticed that the peculiarity of the multi-scale behavior of MW function is given by the phase randomization $\phi_{m,k}$, that it is impossible to introduce in an analytical functions.

2.2 The frictionless normal contact between rough surfaces

The non-conforming contact problem between two rough surfaces under the assumption of linear elasticity can be approximated by the equivalent problem, introduced by Johnson [2003], of a rigid rough surface with composite topography and a deformable flat half plane, with a composite Young's modulus

$$E = \left(\frac{1-\nu_1}{E_1} + \frac{1-\nu_2}{E_2} \right)^{-1}$$

A rigorous proof of the above equivalence can be found in the work of Barber [2003]. Contact begins when the half plane touches the tallest summit of a rough profile/surface, as depicted with a black dash-dotted solid line in Fig. 6. Contact is forced by imposing an approaching far-field closing displacement Δ, which leads to a rigid body displacement of the half-plane (in red). The displacement Δ corresponds to a rigid-body motion of the half-plane. In this configuration, the asperities (b) and (c) are potentially in contact, while the asperity (a) is certainly not. Elastics interactions among asperities deform the half plane, whose deformed configuration is depicted with the solid black line in Fig. 6. The peak (c) of the profile remains in contact, while the asperity (b) looses contact due to the elastic interactions.

2.2.1 Boundary element method

The frictionless interaction in the normal contact between rough profiles/surfaces can be solved via the boundary element method (BEM) (Bemporad and Paggi [2015]; Johnson [2003]; Borri-Brunetto et al. [1999]). In the 2D framework, the vector x refers to the interface discretization along a reference length L, to which corresponds a height field $h(x)$. During contact, each point has experienced a deformation $u(\boldsymbol{x})$, that is determined by the pressure distribution $p(x)$ as follows Johnson [2003]; Barber [2010]:

$$u(x,y) = \int_{A_r} H(x,y)p(y)dA \tag{2.3}$$

The Green function $\boldsymbol{H} = H(x, y)$ represents the displacement at the point x due to a unit traction in y. Thus, the Green function $\boldsymbol{H}$ can be expressed in a matrix form, writing Eq. (2.3) as $\boldsymbol{u} = \boldsymbol{H}\boldsymbol{p}$. The deformation induced to each couple of points, supposing a uniform normal traction acting over a rounded asperity of radius $\delta/2$ (Borri-Brunetto et al. [2001]), is expressed by the Green function $H_{i,j}$

$$H_{i,j} = \frac{2}{\pi E \delta} \arcsin\left(\frac{\delta}{2||x_j - x_i||}\right) \tag{2.4}$$

The global influence matrix $\boldsymbol{H}$ is obtained by computing the Green function term for each couple of points (i, j). This matrix is symmetric and positive definite by construction. The difference between the 2D or the 3D formulation of the frictionless problem basically relies on the construction of the Green function in Eq. (2.4).

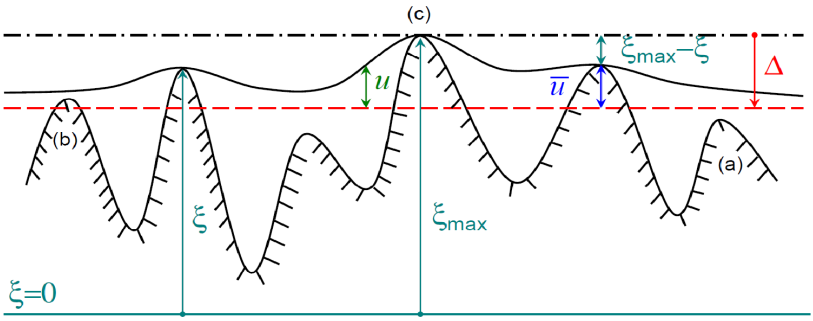

Figure 6: Frictionless normal contact problem between a rigid rough surface and an elastic half-plane. The initial configuration is depicted with a black dash-dot solid line, corresponding to the situation of one point in contact. Then, a far-field closing displacement Δ is imposed, depicted with a red dashed line, corresponds to a rigid-body motion of the half-plane. The deformed configuration (solid black line) may present: (i) heights certainly not in contact from the beginning, type (a); (ii) heights loosing contact due to elastic interactions, type (b); (iii) heights in contact, type (c). Courtesy of Bemporad and Paggi [2015].

The solution of the linear problem $\boldsymbol{u} = \boldsymbol{H}\boldsymbol{p}$ characterize the frictionless normal contact problem in terms of displacements and tractions, once contact constrains are imposed. The pressure vector $\boldsymbol{p}$ must have elements whose value is greater or equal to 0. At the same time, the displacement associated with the asperities in contact is given by the rough geometry. Then, introducing the gap function $\boldsymbol{w} = \boldsymbol{u} - \bar{\boldsymbol{u}}$ (see Fig. 6), all the points in the domain has to satisfy the complementary condition $\boldsymbol{w}'\boldsymbol{p} = 0$, that is called Signorini's condition Bemporad and Paggi [2015]; Johnson [2003]; Yastrebov et al. [2012]. The global problem to be solved is a *Linear Complementary Problem* (LCP):

$$\begin{cases} \boldsymbol{w} = \boldsymbol{H}\boldsymbol{p} - \bar{\boldsymbol{u}} \\ s.t. \quad \boldsymbol{w}, \boldsymbol{p} \geq 0, \quad \boldsymbol{w}'\boldsymbol{p} = 0 \quad \forall \boldsymbol{x} \end{cases} \tag{2.5}$$

The gap $\boldsymbol{w}$ is positive for a point that is not in contact and it is equal to zero for a point in contact. Then the size of the problem associated with the aforementioned system can be reduced by considering only the points than can satisfy this condition, i.e., all the points such that $\boldsymbol{w} \leqslant 0$.

This LCP problem can be solved either by a LU factorization or by a classical greedy method. Bemporad and Paggi [2015] proposed the quadratic programming (QP) technique *Non Linear Least Square* (NNLS) method to efficiently solve the aforementioned contact problem. This is can be done by reformulating the LCP in Eq. (2.5) to the equivalent QP problem, according to the energy minimization principle:

$$\begin{cases} \min\limits_{\boldsymbol{p}} \quad \frac{1}{2}\boldsymbol{p}'\boldsymbol{H}\boldsymbol{p} - \bar{\boldsymbol{u}}'\boldsymbol{p} \\ s.t. \quad \boldsymbol{p} \geq \boldsymbol{0}, \quad \forall x \end{cases} \tag{2.6}$$

The equivalence of the LCP in Eq. (2.5) and the QP in Eq. (2.6) is assured by the fact the Green function H is a symmetric positive definite matrix by definition, which allows the Cholesky factorization $\boldsymbol{H} = \boldsymbol{C}'\boldsymbol{C}$. The NNLS method is very powerful, presenting a speed-up of at least twenty times with respect to the classical greedy method. All the contact problems (2D and 3D) presented in the following are solved using the NNLS formulations.

2.2.2 Mechanical quantities of interest

Once the contact problem is solved, the post-processing of results can be done not only by visualizing the deformation, but also by computing the main mechanical quantities useful to characterize the contact problem. The total load P is computed by summing all the contact tractions. The number of the asperities in contact, n_c, corresponds to the number of the non-zero elements of $\boldsymbol{p}$). Finally, the real contact area A_r is computed as the number of asperities in contact n_c multiplied by the single asperity area that is, for a square 3D grid, equal to δ^2, while for a 2D profile it is equal to δ. Another important mechanical quantity to examine is the contact stiffness K, computed as the partial derivative of the load acting with respect to the imposed displacement Δ:

$$K = \frac{\partial p}{\partial \Delta} \tag{2.7}$$

The role of contact stiffness in contact mechanics has been widely investigated in relation to the interface thermal and electrical conductivities (see e.g. the works of Barber [2003, 2010]; Paggi and Barber [2011]; Ciavarella et al. [2008]), since the contact conductance is proportional to the incremental contact stiffness as discovered by Barber [2003], who rewrote the electrical contact resistance R in therms of electric flux Q. This two quantity are inversely proportional, respect to the composed electrical conductivity of both material in contact $\rho^* = \rho_1 + \rho_2$. Barber [2003] also noticed that the electric flux Q changes as a displacement perturbation $\partial\Delta$ (or ∂p) is imposed to the system, who produces an increment of acting load ∂p (or, vice-versa, of displacement $\partial\Delta$). Barber [2003] derived the seminal relation between the contact stiffness and the electrical resistance of a rough profile:

$$R = \frac{\rho^*}{E} K.$$

Numerical results are often represented by dimensionless quantities to generalize their validity. The dimensionless contact area A^* is the ratio between the real contact A_r and the nominal one, A_n, i.e. $A^* = A_r/A_n$. The dimensionless load is obtained by dividing the applied load p by

a reference length L and the root mean square σ of the distribution of surface heights multiplied by the composite Young's modulus E, i.e. $P^* = pL/(E\sigma)$. The choice of using σ is justified by the fact that, in a linear elastic framework, a rescale of the height distribution by a factor η simply lead to a rescale $\sigma \to \eta\sigma$. Consequently, for a rescaled far-field displacement, $\Delta \to \eta\Delta$, the predicted real contact area is equal to that of the original not rescaled surface. Also, the load rescale $p \to \eta p$, and the contact stiffness K would remain unchanged. See also Zavarise et al. [2007], Paggi and Ciavarella [2010] and Yastrebov et al. [2015] for details.

To show an example of a contact mechanics problem in a nutshell, the RMD algorithm is used to generate a rough surfaces, e.g. with $D = 2.3$ and $m = 7$. The surface lateral size $L = 0.1$ mm. The undeformed surface (Fig. 7(a)) presents a maximum height equal to $h_s = 6.72$ μm. Here, the half-plane is considered rigid and the deformation is treated to the surface. In Fig. 7(b) the case of almost full contact is presented, i.e. $\Delta^* = \Delta/h_s = 1$.

The asperities in contact are visualized by the dark red areas. In this case, the value of the dimensionless contact area, corresponding to Fig. 7(b), is $A^* = 0.25$. From the obtained solution, it is possible to analyze the pressure distribution and compute the applied load, whose dimensional values is $P^* = 0.56$.

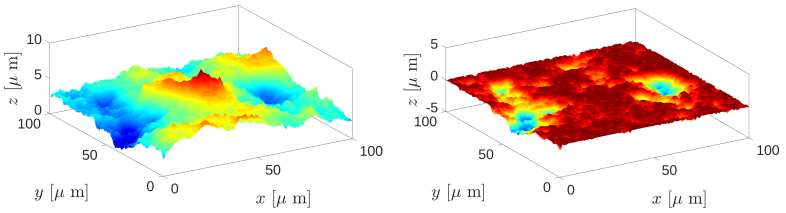

(a) $\Delta^* = 0$ (b) $\Delta^* = 1$

Figure 7: (a) Topography of a surface composed by RMD patches with $m = 7$ (128×128 heights per side) and $D = 2.3$ (b) Its deformed topography in the frictionless elastic normal case, obtained via BEM.

2.2.3 The free volume between contacting rough surfaces

When contact takes places, the gap function $\boldsymbol{w}$ computed at a fixed compenetration level Δ characterizes the free network of channels that governs the percolation of a fluid between the two rough surfaces. This concept is visualized in Fig. 7, for a surface composed by RMD patches. In Fig. 7(a) the surface summit acts has a bluff body in the middle of a wide channel where a fluid can freely percolate.

On the opposite, in Fig. 7(b) a lot of patches are in contact or present a small gap value (dark red zones), determining an indented network with lower probability of fluid leakage.

The geometrical characterization features of this free network of channels affects the fluid percolation between rough surfaces (Darcy [1857]; Moody [1944]; Persson [2001]; Yu and Cheng [2002]), the shape and the area magnitude of the critical cross-section of this network (Lorenz and Persson [2009]; Dapp et al. [2012]; Persson [2001]). Also, the statistical properties of the surface play an important role in this regard as demonstrated by Putignano et al. [2012b, 2013], but mainly regarding the stress distribution and the parent deformation. See also Pérez-Ràfols et al. [2016a,b] for the leakage features associated to different kind of contacting bodies.

A first attempt to relate the features of this free network to the gap function have been done by Paggi and He [2015], who introduced the concept of free volume between rough surfaces in contact. The domain U_v determining the free volume is composed by all the boundary elements whose points have a positive gap $\boldsymbol{w} > 0$ (or greater than a given threshold). The free volume V is computed by summing up all the contributes of those small prisms Paggi and He [2015]:

$$V = \sum v_i \; \forall v_i \in U_v \tag{2.8}$$

Paggi and He [2015] also introduced the dimensionless free volume $V^* = V/(L^2\sigma)$ to exploit the results of different families of surfaces, generated with the RMD algorithm with $m = 8$ and different fractal dimension D.

Moreover, the dimensionless separation between the average plane of the surface and the indenting half-plane, $\frac{d}{\sigma}$, can be introduced as customary in micro-mechanical contact theories to characterize the contact level.

Paggi and He [2015] found a linear dependence between V^* and $\frac{d}{\sigma}$ for high separations (Fig. 8), whereas their relation becomes nonlinear for small separations. This trend is similar for all the fractal dimensions between $D = 2.1$ (black lines) and $D = 2.9$ (red lines). This results highlight the fact that it is important to study the variability $\frac{d}{\sigma}$ of V^*, which cannot simply confused with $\frac{d}{\sigma}$ for small gaps.

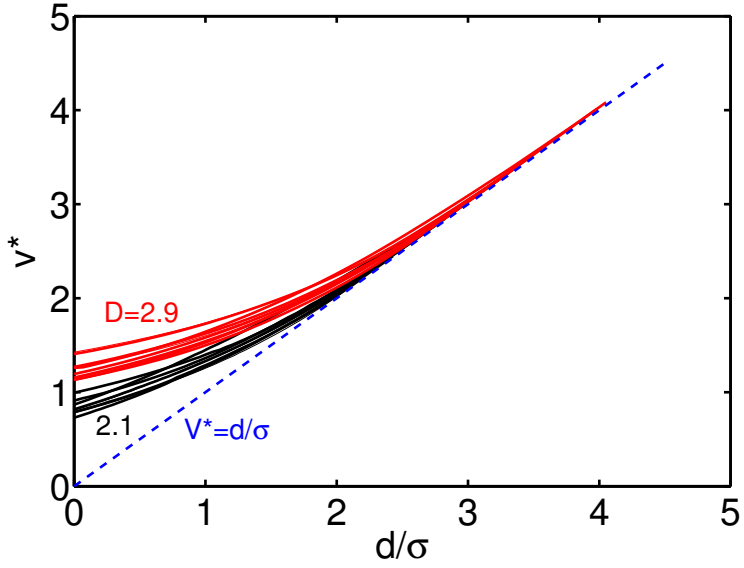

Figure 8: Dependence of V^* on the mean plane separation $\frac{d}{\sigma}$ for $D = 2.1$ and $D = 2.9$. Note the deviation from linearity for small values of $\frac{d}{\sigma}$, courtesy of Paggi and He [2015].

2.3 Computational methods to simulate fluid flow across rough surfaces in partial contact

A seen so far, the leakage phenomena mainly depends on the tortuosity of this network as stated by Darcy [1857]; Colebrook [1939]; Persson [2001] in different works, to whose shape Yu and Cheng [2002] assigned a fractal dimension, the shape and the cross-area of a the critical section of this network Lorenz and Persson [2009]; Dapp et al. [2012]; Persson [2001]. However, a generic fluid percolates if subjected to piezometric potential, i.e., a difference of pressure or height, that determines the inertial properties of the leaking fluid, i.e. the relative Reynolds number (Darcy [1857]; Lorenz and Persson [2009]; Bottiglione et al. [2009a]; Dapp et al. [2012]; Versteeg and Malaskera [1995]). In the following, some numerical approaches are proposed to sketch the fluid wall interaction in the contact between rough surfaces.

2.3.1 Darcy flow in constrained channels

In the case of a fluid flow constrained in a channel with rough boundaries, the average velocity $\bar{v}$ in the fluid is related to the average pressure gradient $\bar{\nabla} p$ in the domain via a Darcy type relation:

$$\bar{\boldsymbol{v}} = -\frac{\boldsymbol{\mathcal{K}}}{\mu}\bar{\nabla} p \tag{2.9}$$

where $\boldsymbol{\mathcal{K}}$ is the permeability tensor. The Darcy relation in Eq. (2.9) has been rigorously demonstrated by Whitaker [1986]. From the operative point, Whitaker [1986] proposed to compute the average pressure gradient $\bar{\boldsymbol{p}}$ from the imposed pressures acting on the free volume boundaries due to simple equilibrium consideration. At the same time, the average velocity $\bar{v}$ can be evaluated by averaging the velocity field over the whole free volume domain where the fluid flows. The relation (2.9) is very useful in constrained flows for engineering problems, such as piping and lubrication Moody [1944]; Colebrook [1939].

Many authors provided numerical schemes for the extension of the Darcy's law to complex networks. Rubinstein and Torquato [1989] pro-

posed an homogenization technique to predict the permeability of a porous media via an homogenization technique, assuming an isotropic medium both at the macro and at the micro length scales. Yu and Cheng [2002]; Yu et al. [2003] proposed a different attempt to extend this techniques to bi-dispersed and unsaturated porous media.

However, the shape of the channels and the transition between laminar and turbulent flow is fundamental to determine the permeability of this particular network as investigated by Papautsky et al. [2001]; Colebrook [1939]. For Stokesian flow (Reynolds number less than 5), the geometry of the channel is more crucial (Papautsky et al. [2001]). Yu and Cheng [2002]; Wu and Yu [2007] tried to assign a fractal dimension to the fluid path to model the channel tortuosity. This fractal dimension is related to the fractal dimension of the surface in contact. As a results, the wall-fluid interaction for Stokesian fluid motions can be expressed by a simple geometrical relation. However, the typical operating conditions of modern instruments, such as bearings, require a more detailed description of fluid-solid interactions and they do not often comply with the assumption for a Stokesian flow, as presented in different situations by Papautsky et al. [2001]; Judy et al. [2007].

2.3.2 Reynolds equation for thin film applications

Let us focus on the mathematical model of an incompressible Newtonian fluid flowing into the free volume between two approaching rough walls which have a relative velocity $U = (U_x, U_y)$, assuming a non-Stokesian flow but in the laminar regime (Reynolds number comprised between 5 and 100). The variable $\boldsymbol{h}$ represents the height distribution of the channel. A generic fluid is characterized by the fluid density ρ (constant on this incompressible case) and by the fluid viscosity μ (constant under the Newtonian assumption). Under the additional hypothesis of adiabatic and stationary flow, the Navier-Stokes equations (Versteeg and Malaskera [1995]), which govern the fluid flow in any environment, reduced to the *Reynolds equation*. The reader is refereed to Hamrock et al. [2004] for its derivation.

The mass balance for a fluid in a channel is expressed as:

$$\nabla \cdot \boldsymbol{q} = 0. \tag{2.10}$$

The mass flow $q(\boldsymbol{x})$ can be derived from the conservation of momentum, considering negligible mass forces and the wall condition $u_x = U_x$:

$$\boldsymbol{q} = \frac{\rho \boldsymbol{h}}{2} U_x - \frac{\rho \boldsymbol{h}^3}{12\mu} \nabla \boldsymbol{p}, \tag{2.11}$$

that has to obey the mass conservation law in Eq. (2.10), yielding to the classical form of the 2D Reynolds equation:

$$\nabla \left(\frac{\rho \boldsymbol{h}^3}{12\mu} \nabla \boldsymbol{p} \right) = \nabla \left(\frac{\rho \boldsymbol{h}}{2} U_x \right). \tag{2.12}$$

The numerical or analytical solution of Eq. (2.12) has been widely used in many engineering applications. Also, many authors focused their attention on how to introduce other effects in this simple model, to provide a more detailed description of the physics behind. Patir and Cheng [1978, 1979] derived a method that rewrites the Reynolds equation in terms of the averaged flow factors for control volumes, and it is applicable to any roughness structure. Later on, Almqvist [1996] extend this homogenization process also to compressible fluids. Following these seminal works on the Reynolds equation, some Computational Fluid Dynamics (CFD) simulation were conducted by Sahlin et al. [2005, 2007, 2010] to study the flow in bearing applications, where a wall is fixed and another moves at its operating velocity. These studies provided a very detailed analysis of the fluid flow, although they are demanding from the computational point of view.

One useful model was provided by Almqvist et al. [2014], who coupled the Reynolds equation (2.12) with a simple cavitation model to study the onset in lubricated bearings. The proposed approach was used to estimate the pressure recovery in journal bearings with a reduced computational demand as compared to CFD simulations. In regions where cavitation takes place, the fluid will be a mixture of liquid and gas bubbles (cavities) and the pressure tends to be more or less constant, i.e.,

$p \approx p_c$, were p_c is the cavitating pressure. However, the fluid density ρ_c is not constant, and it can be approximated according to the Barus law $\rho = \rho_c \exp(\frac{p-p_c}{\beta})$, where β is the bulk modulus of the fluid. Also, the cavitation density ρ_c is related to the saturation variable ξ, that satisfies the condition $0 \leq \xi \leq 1$. The cavitation variable $\eta = 1 - \xi$ is introduced along with the density variable $u = \exp(\frac{p-p_c}{\beta}) - 1$ valid locally in all the domain, with $\boldsymbol{u} \geq 0$. These two variables are complementary in the whole domain ($\boldsymbol{u}\eta = 0$). The mass flow can therefore be rewritten by considering both cavitating and not cavitating areas:

$$\boldsymbol{q} = \rho_c \begin{cases} \frac{\boldsymbol{u}\boldsymbol{h}}{2} U + \frac{\boldsymbol{h}}{2} U - \beta \frac{\boldsymbol{h}^3}{12\mu} \nabla \boldsymbol{u}), & u > 0 \\ \frac{\boldsymbol{h}}{2} U - \eta \frac{\boldsymbol{h}}{2} U, & u = 0 \end{cases} \tag{2.13}$$

Then, applying the mass conservation law in Eq. (2.10) to the mass flow expression in Eq. (2.13), the Linear Complementary Problem LCP is found locally:

$$\begin{cases} \nabla \cdot \left(\beta \frac{h^3}{12\mu} \nabla u - \frac{uh}{2} U \right) = \nabla \cdot \left(\frac{h}{2} U \right) - \nabla \cdot \left(\eta \frac{h}{2} U \right) \\ u \geq 0, \quad 0 \leq \eta \leq 1, \quad u\eta = 0 \end{cases} \tag{2.14}$$

Almqvist et al. [2014] extended the aforementioned LCP to finite domains, by discretizing the continuum according to a finite difference method to compute derivatives, combining the central and upwind schemes for full and cavitated regions, respectively.

2.3.3 Some observation about the coupling of the fluid flow motion with the normal contact problem

Computational methods summarized in Sec. 2.3.1 and Sec. 2.3.2 are the most common approaches to pursuit a fluid-dynamic simulation across the volume of rough surfaces in contact. The Darcy's type relation in Eq. (2.9) is the simplest model, albeit it does not provide any Eulerian information (Sec. 2.3.1). On the opposite, following a fluid dynamic approach, it is possible to obtain any physical information of the flow, but with a significant computational effort.

In Cinat and Paggi [2015], a stabilization of the time oscillations in the average Reynolds number has been noticed by reducing the free volume, as a consequence of the reduction of the hydraulic diameter governing the fluid flow. The convergent Reynolds number in the quasi static-regime tends to be almost independent of the pressure drop as depicted in Fig. 9, justifying the use of either the Darcy model or the Reynolds equation.

After a preliminary time frame where the Reynolds number is very high, due to the algorithm initialization, quasi-stationary regime takes place with a Reynolds number low enough to assure Stokes flow. In that regime the permeability in Eq. (2.9) is computed. The convergent Reynolds number depends on the analyzed deformed surface. By increasing Δ, the Reynolds number has a faster decrease and oscillations amplitudes disappear.

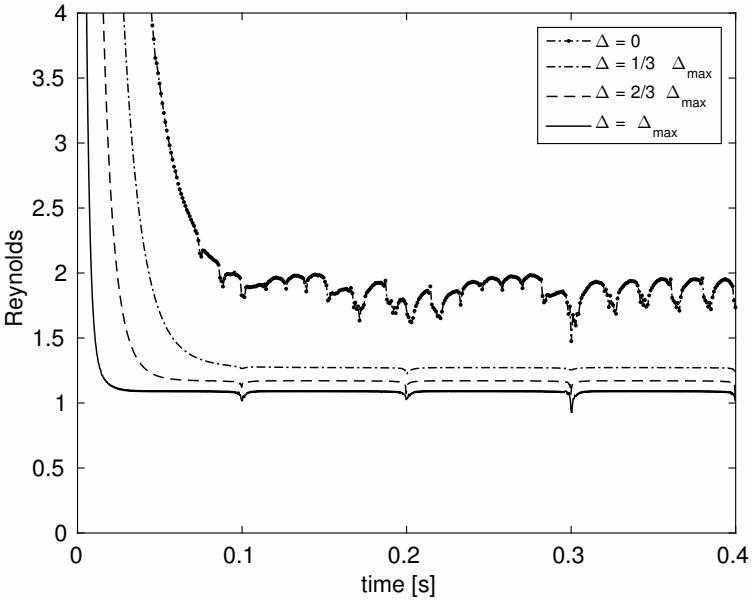

Figure 9: Results obtained by the numerical simulation for the pressure driver condition of $\Delta p = 1$ Pa. ($m = 7$ and $D = 2.3$).

The computational coupling between the fluid flow motion and the mechanical normal contact problem might be achieved thanks to the Reynolds equation (Sec. 2.3.2), either with a monolithic solver or a partitioned one. Partitioning the fluid-structure interaction may leads to instabilities of the solution and difficulties in the numerical methods to be implemented.

A simple illustrative example can be provided by discussing the coupling between the frictionless BEM contact solution, see Sec. 2.2, with the cavitation model provided by Almqvist et al. [2014], see Sec. 2.3.2. The matrices resulting by the two problems present very different features, requiring different numerical methods for their solution.

In the contact problem formulation via BEM, this matrix is symmetric positive, permitting Cholesky factorization $\boldsymbol{H} = \boldsymbol{C}'\boldsymbol{C}$, as illustrated by Bemporad and Paggi [2015]. In the cavitation case, the matrix is not symmetric. Then, Almqvist et al. [2014] used the Lemke's pivoting algorithm to solve the LCP. The Lemke algorithm might be used also to solve the frictionless normal contact problem to simplify the coupling procedure.

However, a staggered approach to solve the fluid structure interaction has to be done with care. Once the geometry is changed due to the fluid pressure, the contact problem has to be solved due to the change in the normal interference. The mathematical formulation of the cavitation problem requires to be adapted and/or refined, significantly increasing the simulation time fo overall convergence.

The monolithic solution scheme to determine the deformation caused by the coupled effect of the fluid and the imposed compenetration is the most reliable procedure. However, it requires a specific numerical method to coherently describe the mechanical fluid-structure interaction. The effect of the trapped fluid is crucial in this concern, since it determines a more complex interaction. Yastrebov et al. [2017b] provided a preliminary approach to address this problem.

2.4 Percolating and non-percolating networks of contacting rough surfaces

The focus of this Section is on the analysis of the trapped volume between rough surfaces in contact. The investigation concerns the geometrical feature of the network of channels composing such a free volume. The localization of closed paths or voids permits to identify regions of the overall volume where the fluid remains trapped. Thus, an algorithm is herein proposed to perform this geometrical study of the channel network. This algorithm, developed in Matlab [2016], is able to distinguish between *percolating* and *non-percolating* domains, by simulating the motion of a hypothetical fluid across such a network.

The proposed algorithm has been applied to 5 different sets of 20 numerically generated rough surfaces, each with a given fractal dimension D (2.1, 2.3, 2.5, 2.7, 2.9), to characterize the percolating properties and also investigate the resolution dependence of the predictions. These surfaces are numerically generated according to the RMD Algorithm (Sec. 2.1.1) over a square of lateral size $L = 0.1$ mm. The same random seed is maintained for each surface at different D, to highlight the effect of the fractal dimension. The resolution dependence is investigated by varying linearly m from 2 to 8. Then, for each surface, the frictionless normal contact problem (Sec. 2.2) is solved at different compenetration levels, considering the rough surface as elastic and the half-space as rigid. The displacement Δ is imposed from the summit of a single surface (infinitesimal contact, $\Delta = 0$) to its smallest elevation (almost full contact, $\Delta = h_s$), considering six equipoised contact steps.

2.4.1 Proposed algorithm to identify the volume networks

The algorithm herein proposed identifies the free network of channels composing this free volume. The computational domain in which a rough surface is discretized is a square grid of n_{div} point by side. The channels are discretized considering the boundary elements not in contact, which have a positive gap, and they determine the set U.

The free channels characterizing the network volume are discretized as follows. A representative rough surface is proposed in Fig. 10, generated with the RMD algorithm (Sec. 2.1.1) in a square of $L = 5$ mm, with $D = 2.3$ and $m = 2$, considering a compenetration Δ equal to the peak-valley distance. Contacting asperities are presented in black squares, centered in the corresponding grid point. Further, red dash-dotted line represents the possible cross-sections normal to the horizontal direction, that is labeled with $i = 1$. On the opposite, cross-sections normal to the vertical direction, $i = 2$, are depicted by blue dash-dotted lines.

A single boundary element is delimited by each pair of lines in Fig. 10(a) and labeled by different letters in Fig. 10(b), where it is also the associated value of free volume is shown.

A channel is limited by two vertical or horizontal cross-sections, the inlet and outlet, according to the fluid motion. These sections are defined at two neighbors grid lines and, then, the length of the channel is δ. The channel volume is the sum of boundary element volumes that are sharing two opposite sides with the inlet / outlet cross-sections.

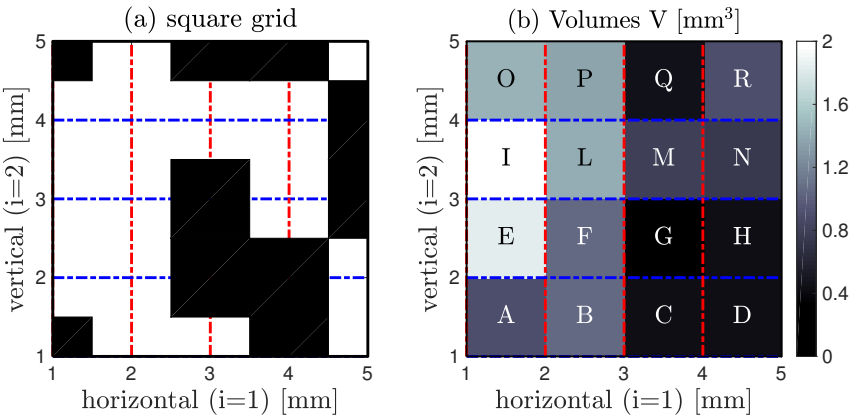

Figure 10: RMD surface with $D = 2.3$, $m = 2$, $\delta = h_s$. (a) black squares are asperities in contact, vertical cross-sections (red lines) for horizontal fluid flow and horizontal cross-sections (blue lines) for vertical fluid flow. (b) volume associated to each boundary element composing.

All the cross-sections are limited by two neighboring asperities, depending on the fluid direction. They are so identified and labeled by numbers in Fig. 11, centered in their mean coordinate. Vertical and horizontal fluid flows are considered. For example, looking at Fig. 11(a), the cross-section 3 and 5 are sharing the boundaries elements E, F, composing a channel. Then, the channel volume is obtained summing up the values of volumes E and F.

Once a channel is identified, its hydraulic diameter D_h is computed by dividing its volume by the square value of its length, i.e., $D_h = V/\delta^2$. The definition of hydraulic diameter allows the introduction of fluid-dynamics constraints according the theory of micro-channel by Darcy [1857] or Moody [1944], revised by Papautsky et al. [2001]. If the hydraulic diameter ratio of two connecting channel is high, it means that there is a consistent constriction and the fluid might not flow. This depends on the fluid viscosity. However, in the investigation herein presented this threshold is not considered, to focus only in the morphology deformation.

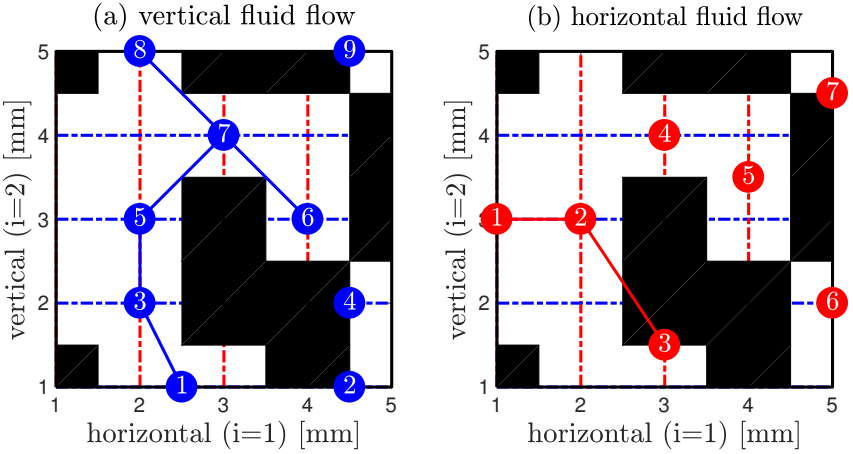

Figure 11: Possible paths to flow into the volume network of the reference surface in Fig. 10. (a) in vertical direction or (b) in horizontal direction.

Considering as example a a vertical flow, the fluid enters the square from the boundary elements A,B,C as the volume D is null. Then, it flows through cross-section 1, going towards cross-section 3 and so on and so forth, exiting the domain through cross-section 8. The connections associated to this path has active role in fluid leakage and, then, the associate volumes are considered in the percolating domain.

Fluid will remain trapped if it flows from cross section 7 to 6. Any other connection allows its flowing motion from cross-section The connection 6-7 has a passive role in fluid leakage and, then, the associate volumes belong to the non-percolating domain.

Percolating domain, identified by retaining only active channels, is shown in Fig. 12(a). It is composed by the boundary elements A, B, C, E, F, I, L, O, P. These boundary elements identify the set U_p, which sum gives the value of the percolating volume V_p. The remaining volumes determine set U_{np}, see Fig. 12(b) and their sum gives the non-percolating volume $\bar{V}_p$.

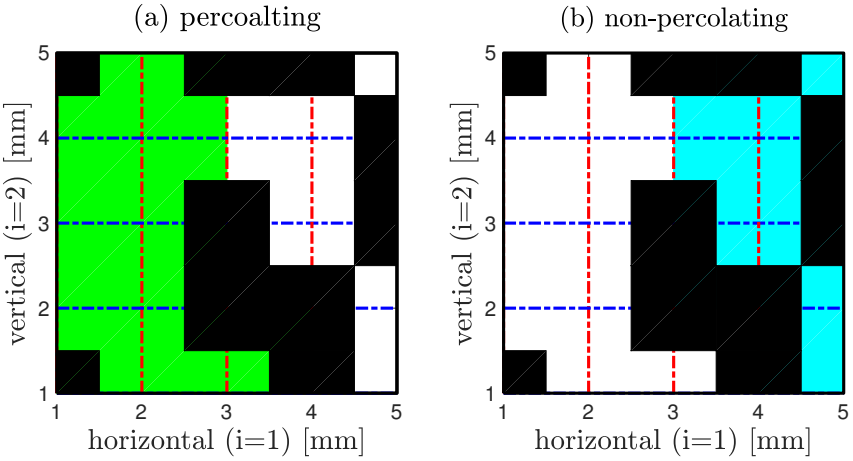

Figure 12: Percolating and non-percolating domains for vertical flow, see Fig. 11(a).

However, looking at Fig. 10, it is possible to notice that the fluid can exit (or enter) the domain from cross-section 7 by passing through cross-section 9. This is possible if, and only if, the central point of boundary element R is a *saddle point*. Dapp and Muser [2015] demonstrated that saddle points are crucial in the leakage of a fluid this free network.

A saddle point is shown in Fig. 13(a), where a boundary element is depicted by a blue continuum line. The central dashed lines are depicted to visualize better saddle point (round red point) that lies on the mean plane (dotted black line) of the boundary element. Vertexes 2 and 3 of the boundary element are in contact.

On the opposite, the vertexes 1 and 4 are not in contact, with a larger gap than the one d_{zc} of the red point, that is a saddle point. In this case, the hydraulic diameter is computed considering a cross-triangular section, i.e. $D_h = \frac{\sqrt{2}}{2}\delta d_{zc}$.

The same boundary element is depicted in Fig. 13(b) but, in this case, the point 4 has lower gap than the red point, that is not a saddle point in this case. This is the case of boundary element R in Fig. 10(b) and so the connection 7-9 is not considered in the connectivity matrix.

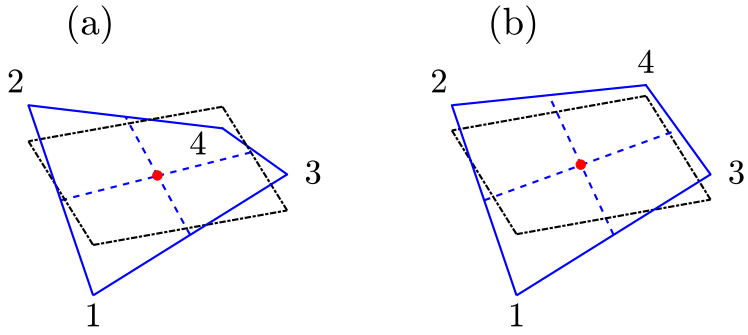

Figure 13: Possible configurations of a boundary element in contact. The central point of the boundary element in Fig. 13(a) is a saddle point. At the opposite, boundary element in Fig. 13(b) does not presents a saddle point.

Operatively, algorithm is summarized in Alg. 1.

The first step is to initialize as empty sets the matrices containing the geometrical characterization of each section $\boldsymbol{S}$ (cross-area, perimeter, hydraulic diameter), the connectivity $\boldsymbol{C}$ between cross-sections and the list of point $\boldsymbol{P}$ identifying each volume.

Then, starting from the selected side ($id_{dir} = 1$ or $id_{dir} = 2$), all cross-sections present in all the n_{div} lines parallel to this side are identified (Steps $3 - 5$). An intermediate matrix $\boldsymbol{A_1}$ is used to store the geometrical characterization of the cross-sections at the j-th vertical/horizontal line. The point bordering such cross-sections are stored in a matrix $\boldsymbol{P_1}$.

The matrices $\boldsymbol{A_0}$ and $\boldsymbol{P_0}$ identifies the set of cross-sections belonging to the previous $(j - 1)$th line (Steps $6 - 7$). If or $\boldsymbol{A1}$ is empty, then the algorithm is stopped because there are no connections is available (Step 29).

Now, all the cross-sections in ($\boldsymbol{A_0}$,$\boldsymbol{P_0}$) and ($\boldsymbol{A_1}$,$\boldsymbol{P_1}$) are compared looking at possible channels in common, retaining the boundary elements with at least $n_c > 2$ discrete points in common on the same side (Steps $12 - 21$). The symbol $\#$ indicates the cardinality of a given set. In such case of two points in common, the connection is possible if these point belong to one diagonal of the boundary elements and the boundary element is a saddle point (Steps $14 - 15$). The matrix C is retained considering positive value of the hydraulic diameter (Steps $22 - 24$).

Once the algorithm is completed, the matrix $\boldsymbol{C}$ express all connection between cross-sections and the value of the hydraulic diameter D_h. Thus, open paths are obtained by iterating $\boldsymbol{C}$ recursively, excluding channels that present only one connection within neighboring cross-sections. Then, boundary elements belonging to this set of channels compose the sub-domain U_p^i.

Algorithm 1 Free volume network algorithm

Input: $\boldsymbol{x}$, $\boldsymbol{w}$, δ, id_{dir} (=1, horizontal & =2, vertical)
Output: geometrical characteristics of the network $\boldsymbol{S}$, connection and fluxes between sections $\boldsymbol{C}$.

$\boldsymbol{C},\ \boldsymbol{S} \leftarrow \emptyset$, $n_{div} \leftarrow size(\boldsymbol{x}, id_{dir})$, $n_0 \leftarrow 1, n_s \leftarrow 1$
for all $j = 1 : n_{div}$ **do**
    $\boldsymbol{A_1}, \boldsymbol{P_1} \leftarrow \emptyset$
    $indends \leftarrow$ indexes of asperities in contact for a section
    $\boldsymbol{P_1} \leftarrow f(indends, \boldsymbol{w}, \delta))$, $\boldsymbol{A_1} \leftarrow f(\boldsymbol{P1})$
    if $\boldsymbol{A_1} \neq \emptyset$ **then**
        $\boldsymbol{S} \leftarrow [\boldsymbol{S};\ \boldsymbol{A_1}]$, $\boldsymbol{P} \leftarrow [\boldsymbol{P};\ \boldsymbol{P_1}]$
        if $j == 1$ **then**
            $\boldsymbol{A_0} \leftarrow \boldsymbol{A_1}$, $\boldsymbol{P_0} \leftarrow \boldsymbol{P_1}$
        else if $j \geq 2$ **then**
            for $t = \#(\boldsymbol{A_0}, 1)$ **do**
                for $k = \#(\boldsymbol{A_1}, 1)$ **do**
                    $\boldsymbol{cmn} \leftarrow$ common points between of two sections
                    $D_h = 0$, $n_c = length(\boldsymbol{cmn})$
                    if $n_c = 2$ **then** *connection if b.e. has a saddle point*
                        if *True* **then**
                            $D_h = d_{zc}\frac{\sqrt{2}}{4}$
                        end if
                    else if $n_c > 2$ **then** *connection available*
                        $V_L = f(\boldsymbol{P_1}, \boldsymbol{P_2}, \boldsymbol{w}, \boldsymbol{cmn}, n_c, \delta)$
                        $D_h = \frac{V_L}{\delta^2}$
                    end if
                    if $D_h >= tol$ **then**
                        $\boldsymbol{C} \leftarrow [\boldsymbol{C};\ t\ k\ D_h]$
                    end if
                end for
            end for
        end if
    else if $\boldsymbol{A1} = \emptyset$ **then**
        exit algorithm, no available paths
    end if
end for

2.4.2 Evolution of percolating networks

In the following the percolating volume V_p, is computed by considering both vertical and horizontal percolation, identifying the sub-domain U_p as the union of all those sub-domains, i.e. $U_p = U_p^1 \cup U_p^2$. Thus, its magnitude is given by

$$V_p = \sum v_i \; \forall v_i \in U_p. \tag{2.15}$$

The dimensionless values of the volume expressed by Eq. (2.15) is considered, i.e. $V_p^* = \frac{V_p}{L^2\sigma}$, as proposed by Paggi and He [2015].

Fig. 14 describes the variation of the mean value of the dimensionless percolating volume V_p^* for each set of surfaces, vs $\frac{d}{\sigma}$, where d is the mean plane separation (see Sec. 2.2.2)

A similar trend as that one noticed by Paggi and He [2015] between the total free volume and $\frac{d}{\sigma}$ is found for the percolating volume V_p^*, see Fig. 8. The dimensionless free volume describing the percolating zones during leakage V_p^* is an increasing function of $\frac{d}{\sigma}$ and it is a decreasing function of the fractal dimension D. All the surface sets converge over the same straight line for infinitesimal contact. On the opposite, for high-compenetrations, V_p^* rapidly increases in a non-linear way. This behavior is more pronounced for higher fractal dimension.

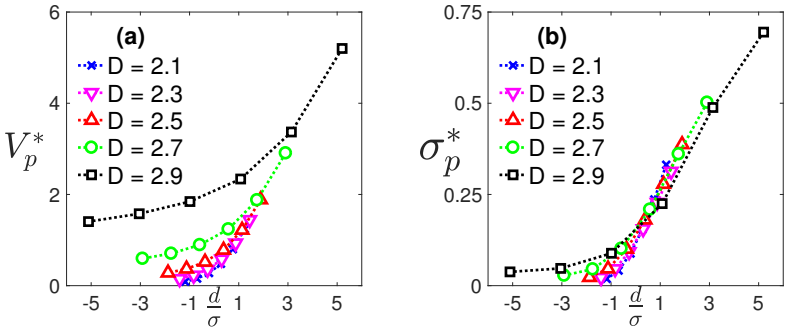

Figure 14: (a) Evolution during contact of V_p^*, the dimensionless percolating domain of the total free volume V^*, in the case $m = 8$. (b) Evolution of the standard deviation σ_p^* of V_p^* for each set of surfaces.

The trend of σ_p^*, the standard deviation of V_p^* for a set at fixed D, is shown in Fig. 14(b) vs $\frac{d}{\sigma}$. Although we found a non linear behavior of V_p^* for negative values of $\frac{d}{\sigma}$, the trend of σ_p^* suggests that V_p^* is quite independent from the height distribution. In fact, all sets have a similar trend regardless D. The main effect of D is to increase the gap between the two surfaces in contact, thus and reducing the number of asperities in contact, leading to a wider network of channels.

2.4.3 Evolution of non-percolating networks

The complementary sub-domain U_{np} of the percolating network U_p identifies the non percolating domains, i.e. $U_{np} = U - U_p$. The magnitude of the non-percolating volume $\bar{V}_p$ is obtained as follows:

$$\bar{V}_p = \sum v_i \; \forall v_i \in U_n. \tag{2.16}$$

Also in this case, $\bar{V}_p$ is made dimensionless with the same parameter used for V_p, i.e., $\bar{V}_p^* = \frac{\bar{V}_p}{L^2\sigma}$.

The trend observed for V_p^* in Fig. 14 is consistent to the one of $\bar{V}_p^*$ and its standard deviation $\bar{\sigma}_p^*$ in Fig. 15. The non-percolating volume $\bar{V}_p^*$ is increased in the almost full contact regime. The transition of $\bar{V}_p^*$

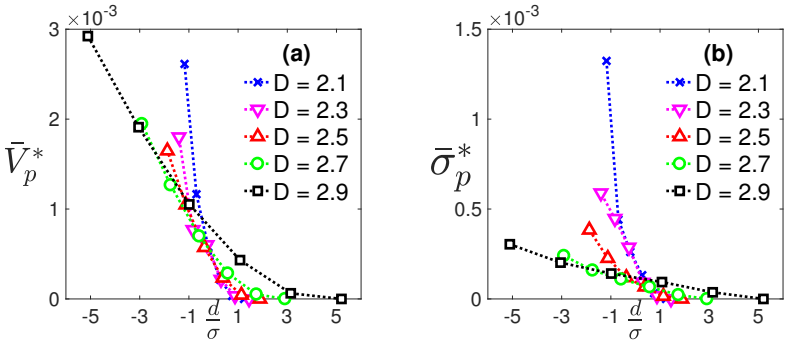

Figure 15: (a) Evolution during contact of $\bar{V}_p^*$, the dimensionless non-percolating domain of the total free volume V^*, in the case $m = 8$. (b) Evolution of the standard deviation $\bar{\sigma}_p^*$ of $\bar{V}_p^*$ for each set of surfaces.

from the infinitesimal contact to the full contact regime is quite sharp for $2.1 \leq D \leq 2.7$, while is less sharp for $D = 2.9$.

The non-percolating volume $\bar{V}_p^*$ is only a small part of the total one V^*, and three order of magnitude occurs between V_p^* and $\bar{V}_p^*$ for low values of D. Around four orders of magnitude exists between V_p^* and $\bar{V}_p^*$, while it increase up to four orders of magnitude for high fractal dimensions. For $D < 2.5$, the dimension of prediction, measured by $\bar{\sigma}_p^*$, is quite high, see Fig. 15(b) in the range $\frac{d}{\sigma} < 0$.

It possible to observe from Fig. 15(b) that fractal sets described with $D < 2.5$ increase the non-percolating volume more rapidly than fractal sets with $D > 2.5$, going through the almost full contact regime. This effect is visualized in Fig. 16 depicts the percolating and non-percolating sub-domains of surfaces, with $m = 8$ and different D. The maximum compenetration level of each surfaces is considered.

The corresponding different topographies are presented in Fig. 16(a), 16(b) and 16(c), correspond to D equal to 2.3, 2.5 and 2.7, respectively. The scaling of the heights field is observable from the different color intensities of the surface. The surface with $D = 2.7$ looks more spiky, with a consequent reduction of the real contact area (dark red zones).

Finally, Fig. 16(d), 16(e) and 16(f) show the percolating (white areas) and non-percolating (red areas) sub-domains of the parent surface. Here, black squares denote asperities in contact.

A consistent reduction of the number of asperities in contact is noticed increasing D. Regarding the percolating and non-percolating domains, the surface increases the percolating domain increasing D, as the gap increases its depth. The different topology of the contact area as D increases, i.e. as the gap increase, determines a more wide and indented network of channels. The non-percolating volume $\bar{V}_p$ is a small part of the overall volume for each case, about three order of magnitude smaller than V_p. Thus, the spatial disposal of contacting asperities is more effective on the percolating properties of a surfaces than the height distribution, as it is possible to conclude comparing Fig. 16 with Fig. 14.

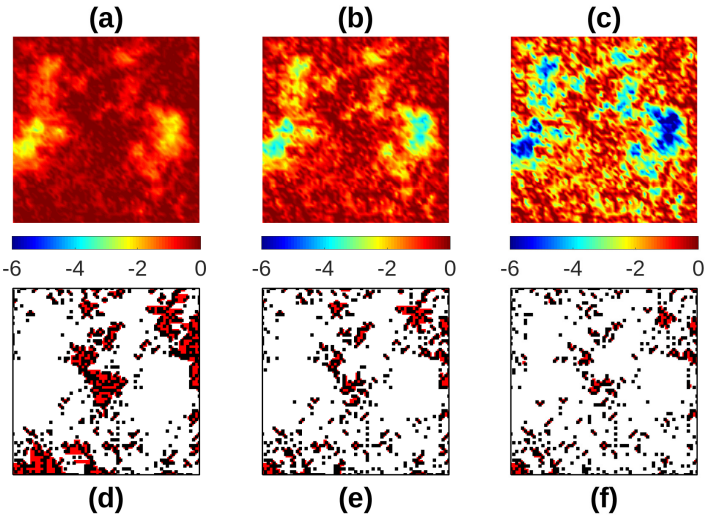

Figure 16: Deformed topographies of the same surface ($m = 6$, $\Delta = h_s$ in each case) with three fractal dimensions: (a) $D = 2.3$, (b) $D = 2.5$ and (c) $D = 2.7$. Black spots are asperities in contact. The white area identifies the sub-part of the free volume involved in the leakage process. Non-percolating volumes are depicted by red squares.

2.4.4 Evolution of surface roughness during contact

The percolating and non-percolating domains are shown vs the surface resolution in Fig. 17, for the same surfaces in Fig. 16(a) with $D = 2.3$. Columns in Fig. 17 correspond to a fixed values of compenetration Δ^*, whereas rows correspond to a given surface resolution. The value $m = 6$ corresponds to a resolution of 64×64 points by side, whereas $m = 8$ correspond to 256×256 points by side.

The non-percolating domains in Fig. 17 are shown in blue for the horizontal direction and in green for the vertical one.

The non-percolating domains in Fig. 17 reduce their size by refining the surface discretization. The morphology of the contact area is also different, determining different features of the channel network. This effect is confirmed also by looking at the non-percolating domains for a

flow along the vertical direction, that vanishes completely with $m = 8$, whereas they are quite extended for $m = 6$ are significant. The same happens for the non-percolating areas in the vertical direction.

The same analysis is repeated for a surface with $D = 2.7$, see in Fig. 18, to investigate the effect of the fractal dimension D. The morphology of the contact area changes consistently from Fig. 17 to Fig. 18. The asperities in contact are more spatially dispersed for $D = 2.7$.

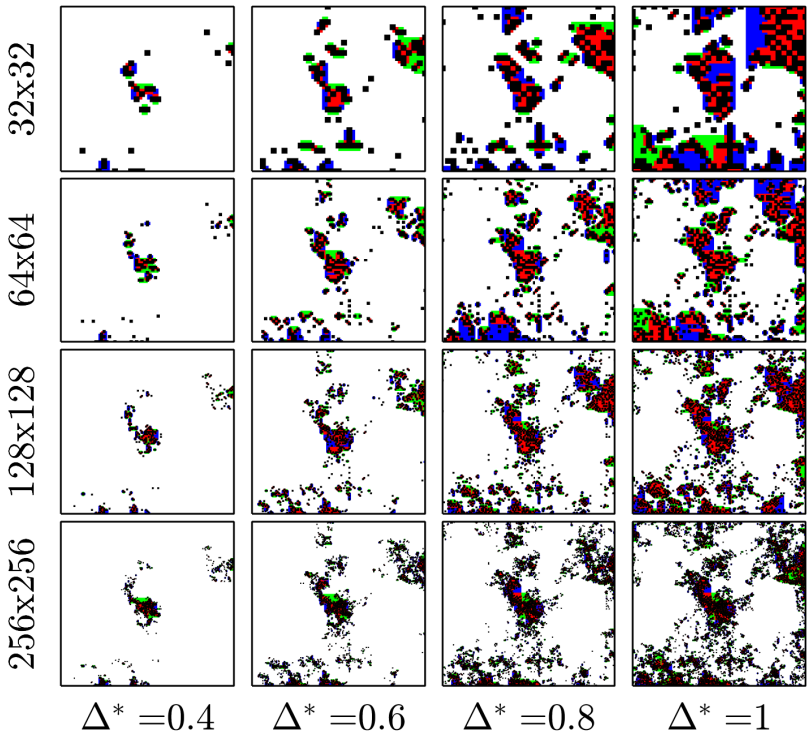

Figure 17: Percolating and non-percolating domains of the surface in Fig. 16 for $D = 2.3$. Blue and green areas depict the non-percolating areas for horizontal and vertical flowing flow respectively.

However, the size of the non-percolating regions seems not to change. Thus, parameters which rule the morphology evolution over contact are herein introduced to clarify their relationship with the percolating and non-percolating domains.

The relation between the contact area and topology of the percolating and non-percolating volumes of a rough surface is now considered. The variation of statistical parameters according to Nayak's theory (Nayak [1971]) is considered to describe the evolution of contact domains be-

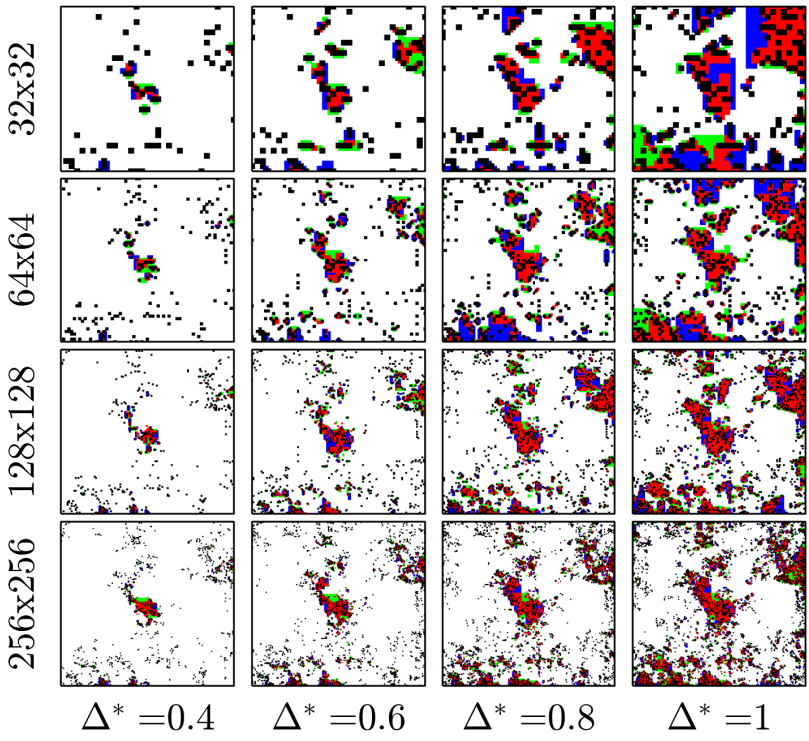

Figure 18: Percolating and non-percolating domains of the surface in Fig. 16 and Fig. 17 for $D = 2.7$. Blue and green areas depict the non-percolating areas for horizontal and vertical flow respectively.

tween rough surfaces. Only the first and second spectral moments are examined. The first moment m_0 is the r.m.s. square of the height field, and it is connected to the height distribution. The second moment m_2 is the r.m.s. square of the slope distribution. Then, it is more connected on the spatial distribution of heights. Their mean value at a fixed fractal dimension D is computed for all surfaces sets at each compenetration, made dimensionless with the initial values of the parent undeformed morphology, i.e., $m_n^* = \frac{m_n}{m_{n0}}$, where m_{n0} is the value of the $n-$th moment of the undeformed surface.

The variation of the statistical parameters during contact is shown in Fig.19. By increasing the contact interference, both statistical parameters diminish, as the surface becomes flatter and flatter and the parent distribution is more compact. At the opposite, m_2^* presents small variations for infinitesimal contact independently of the fractal dimension D, before significantly reducing its value for medium and full contact regimes. This transitional regime takes place when the compenetration is near to the mean plane of the surfaces ($\frac{d}{\sigma} = 0$). In both cases, the reduction of either m_0^* and m_2^* is mitigated as D increase. However, the variation of m_0^* is almost independent of the fractal dimension $D < 2.5$.

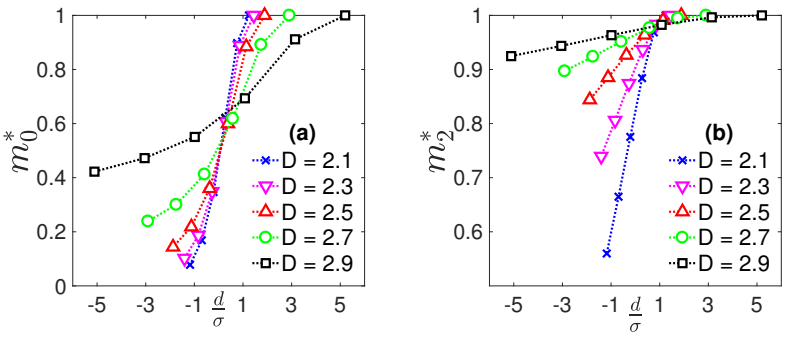

Figure 19: Maintaining Nayak's notation (a) variation of r.m.s. of the height distribution m_0^* for each set of surfaces. (b) of variance of slope distribution m_2^* over contact for each set of surfaces.

The dependencies of the percolating volume V_p^* during contact on m_2^* and on m_0^* are shown in Fig.20. The percolating volume during contact V_p^* is independent of D for $D < 2.5$. In all the cases, going towards the full contact limit, V_p^*.

Fig.21(b) shows the relation between V_p^* and m_2^*, whose curves almost overlap and the percolating volume is almost independent of the variance of the slope distribution. The behavior of V_p^*, observing both dependencies, is connected directly with Persson's theory of leakage (Persson [2001]; Lorenz and Persson [2009]), which states that leakage phenomena do not depend on surface statistics in the full contact regime, mainly if $D < 2.3$)(Persson [2014]).

Finally, the non-percolating volume $\bar{V}_p^*$ is correlated to m_0^* and m_2^* during contact in Fig.21. Examining Fig.21(b), the dependency of $\bar{V}_p^*$ on the variance of height m_0^* presents a highly nonlinear trend over D. On the opposite, the non-percolating volume $\bar{V}_p^*$ tends to be almost independent of m_0^* for $D < 2.5$ (Fig.21(a)). Regarding $\bar{V}_p^*$ and m_2^*, for $D < 2.5$ a quasi parabolic behavior is noticed while, for $D > 2.5$, this behavior is quasi-linear.

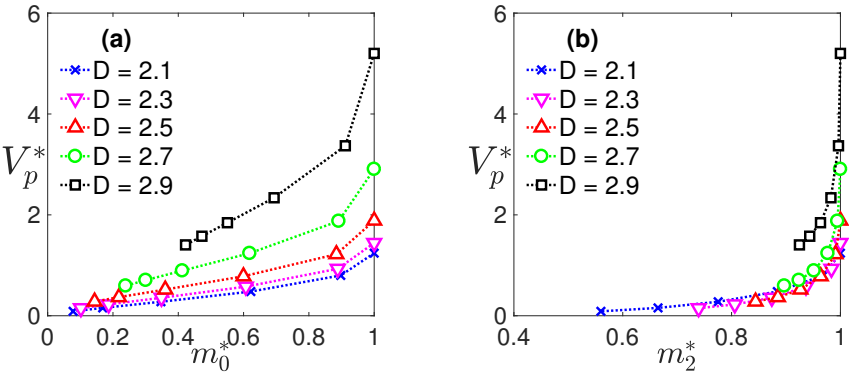

Figure 20: Variation of the percolating volume during contact V_p^*. (a) shows its dependency with respect the dimensionless variation over contact of the variance of heights m_0^*. (b) shows its dependency with respect the dimensionless variation over contact of the variance of height slopes m_2^*.

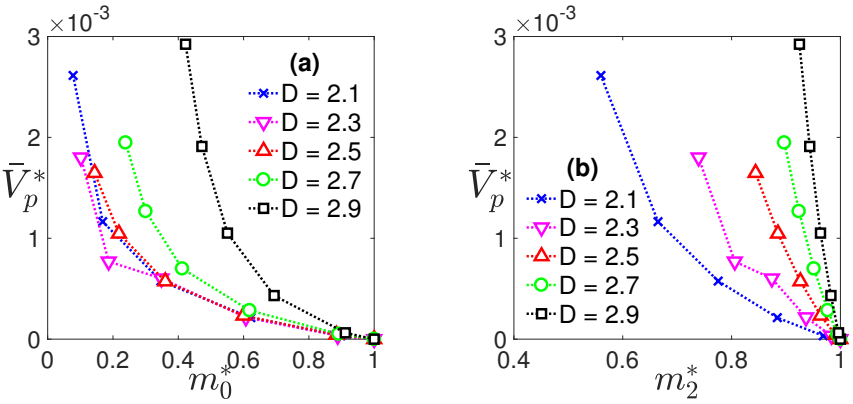

Figure 21: Variation of the non-percolating volume during contact $\bar{V}_p^*$. (a) shows its dependency with respect the dimensionless variation over contact of the r.m.s. of height distribution m_0^*. (b) shows its dependency with respect the dimensionless variation over contact of the r.m.s. of height slopes m_2^*.

2.4.5 The role of surface resolution

Paggi and He [2015] noticed that V^* reduces as A^* increases in the same way, independently of the fractal dimension. On the other hand, they also noticed that the relation V^* vs A^* is strongly resolution dependent, but it is still independent of the fractal dimension. Thus, the same effect that produces a reduction of the contact area, and also influences its morphology, determines a different characterization of the percolating and non-percolating domains over compenetration. This is confirmed the results discussed in the previous sections.

At the same time, the contact area evolution over compenetration depends on the lower cut off ω_ℓ of the parent PSD, that affects directly m_0, see Zavarise et al. [2007]. In the previous subsection, it has been demonstrated that the percolating volume is independent on the variation of m_2 over contact, as shown in Fig. 21(b) for $D \leq 2.5$. The evolution of percolating and non-percolating domains is now investigated focusing into the variation of resolution.

The percolating and non-percolating volume V_p^* and $\bar{V}_p^*$ are shown in Fig. 22 v.s. V^*. Both relations are expressed as functions of the RMD exponent m for the values of three fractal dimension (2.3, 2.5, 2.7). For all the fractal dimensions visualized, increasing the resolution means an increasing of the percolating domain and a decreasing of the non-percolating domain. The same trend has been found for all the other fractal dimensions simulated.

Both percolating and non-percolating volumes V^* and V_p^* increase by increasing D. This effect is connected to the fact that the height field distribution becomes wider. However, the resolution dependency is more pronounced for larger values of D and it is relevant only for the non-percolating volume $\bar{V}_p$, while the percolating one, V_p^*, is almost independent of m and linearly varying with V^*.

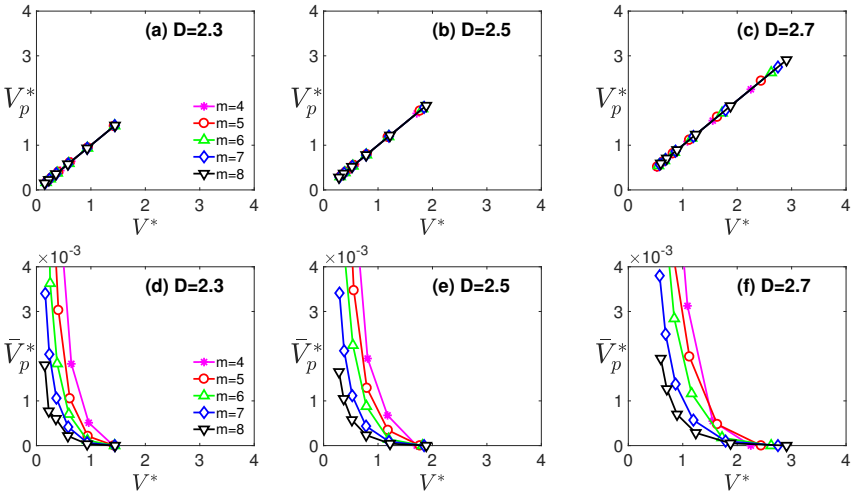

Figure 22: Effect of resolution respect to the percolating V_p^* and non-percolating $\bar{V}_p^*$ volume during contact for $D = 2.3$, (a) and (d), $D = 2.5$, (b) and (e), and $D = 2.7$, (c) and (f).

The evolution of percolating and non-percolating sets U_p and U_{np} over resolution is visualized in Fig. 23, for the same representative surface in Fig. 16 with $\Delta^* = 1$. The increasing value of m reduces in size the non-percolating regions and also, a reduction in size and number is observable for percolating regions identified only for one direction.

The same trend in Fig. 23 is observable also for the morphology of the contact area, that vanishes as the resolution reduces, i.e. m increases. This effect, known as the *lacunarity* effect of the contact area, is typical of fractal models, see Zavarise et al. [2007]; Peitgen and Saupe [1988], and it is connected to the reduction of the boundary elements size, producing a more indented the contact area domain.

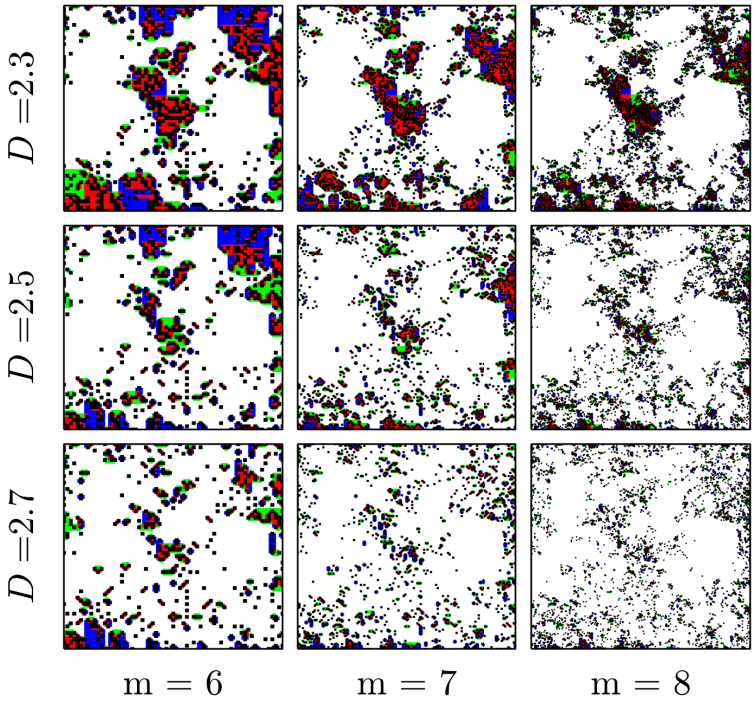

Figure 23: Lacunarity effect of contact area and non percolating domain.

Regarding the free volume domain, the associated network presents more tiny channels as m increases, as previously noticed by Bottiglione et al. [2009b]. The decrease in channel size leads to a reduction of the leak rate (Darcy [1857]). A similar effect appears in Fig. 16, where the asperities in contact forms a more indented shape by increasing D.

A linear relation between V_p^* and V^* and a power-law type relations have been noticed between $\bar{V}_p$ and V^* in Fig. 24, such that:

$$\begin{cases} V_p^* = gV^*, \\ \bar{V}_p = (V^*)^\beta, \end{cases} \tag{2.17}$$

Thus, the best-fitting have been performed to identify the value of g and of the exponent β in Eqs. (2.17). Results of the best-fitting are shown in Fig. 24. The linear coefficient $g = \frac{\partial V_p^*}{\partial V^*}$ is shown in Fig. 24, whose values tend uniformly to the unity by increasing m and it is almost independent of D. A similar trend it is found for β, see Fig. 24(b), with a significant dependency on D. The non-percolating domains tends to a given size by increasing the resolution, $\bar{V}_p \to b$ for $m \to \infty$. From this results it is possible to introduce the following approximation $\frac{\partial V_p^*}{\partial V^*} \cong 1 - \frac{\beta}{10}$.

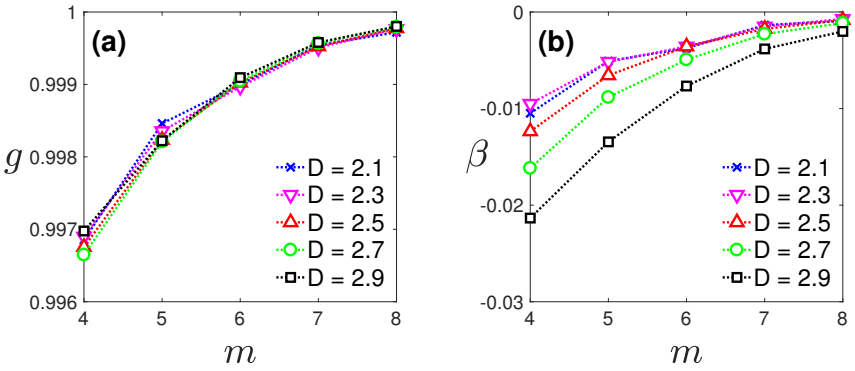

Figure 24: (a) $g = \frac{\partial V_p^*}{\partial V^*}$ evolution over resolution ($\Delta^* = 1$). The same variation over resolution is depicted for the exponent β of the power-law relation between $\bar{V}_p$ and V^* in (b)

2.4.6 Concluding remarks

In this Chapter, an algorithm has been proposed to investigate the feature percolating and non-percolating domains of the free network of channels resulting from a rough in contact with a half space. This algorithm simulates a fluid flow along this network at low Reynolds numbers, keeping track of the areas where a fluid may remain trapped. Once those subdomains have been localized, the contribution of the volume involved in the leakage, V_p^*, is computed, along with the non percolating volume $\bar{V}_p^*$. The problem of detecting a proper grid resolution from a physical point of view is addressed to describe correctly the surface morphology over contact and its characterizing points, as eventual saddle point or critical constrictions.

Percolating and non-percolating properties of the channel network between rough surfaces are related to the height field distribution, especially near the full contact regime in surfaces described by a fractal dimension less than 2.5. In this case, the free volume reduces as the contact level increases. The compenetration effect to the network indentation is not evident for surfaces described by a fractal dimension higher than 2.5. In such a case, the height scaling influences directly the gap between rough surfaces in contact. The network has wider channels and significantly reduce the probability for the fluid to get trapped.

The capabilities of the proposed model to match higher Reynolds flows is done by increasing the piezometric threshold to predict the effectiveness of connections Darcy [1857]. Also, capillarity effects could be taken in into account to evaluate the leak rate of two surfaces in contact following Darcy [1857]; Bottiglione et al. [2009a,b], according to the physical property of a real fluid. In the present study, the main contribution is on the physics of the sealing problem, where the main issue is the separation of components as in bearings (Almqvist et al. [2014]; Fillon et al. [2015]) or in Photo-Voltaic (PV) panels (Gagliardi et al. [2017]). For example, in PV panels the leakage of moisture can also have zones where humidity remains trapped, with a subsequent higher oxidation rate of the Silicon rough surfaces, reducing the efficiency of energy conversion.

Chapter 3

Surface roughness genomics

The focus of this Chapter is the proposal of a new method to characterize surface roughness based on an analogy with genomics. This innovative method, named surface roughness genomics, aims at the characterization each length scale of multi-scale roughness via its constituent waves.

In biology, genetics is the discipline that studies of genes and how they are inherited (King et al. [2006]; Hartl and Jones [2002]). A *gene* is a template for the properties of a specific protein composing the natural organism, following a pre-defined model (Winkler [1920]; Ridley [2006]). This model, in natural biology, is structured as based-pairs of letters (A, T, C and G). Each of these letters refers to chemical characterization of molecule, that carries genetic information (DNA chains) and their combination/evolution. Traditionally, genetic studies have focused on one gene at a time, while *genomics* is the study of large numbers of genes.

Genes compose the hierarchical structures of a natural organism, the *chromosomes*, that determine specific biological properties of natural organisms. The extraction procedure of these genes/chromosome from real organism is called *sequencing*, as it aims at determining the sequence of genetic base pairs in a piece of DNA. The German botanist Winkler

[1920] in 1920 proposed the therm genome to define the hierarchical structure that characterize all living biological systems and, as discovered recently, by exploiting this analogy, also the characterization of materials . Winkler [1920] proposed the word genome by combining the words gene and chromosome: *"I propose the expression Genome for the haploid chromosome set, which, together with the pertinent protoplasm, specifies the material foundations of the species ..."*.

Basically, the genome is the genetic material of a organism/natural system, that contains the biological information for building, running, and maintaining an organism and for passing life on to the next generation. The basic biological system behind the evolution of species is called crossing-over (Ridley [2006]). Variations of the common traits that characterize a natural organism vary and spread through a population due to the effect of crossing over, determining the evolution of species and their ability to survive in new environments (Ridley [2006]; King et al. [2006]).

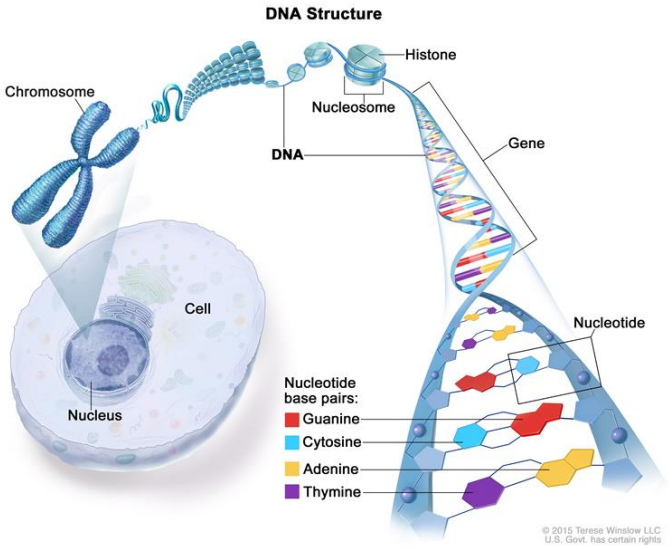

Figure 25: Hierarchy of a biological system. Credits @ Teresa Winslow LCC

In this dissertation, a multi-scale characterization of roughness is proposed considering as base model the MWM function, see Eq. (2.2) in Chapter 2. The MWM function describes roughness over multiple length scales as a series of elementary waves, with a co-sinusoid form, characterizing roughness at a given wavelength. The analogy with biology is exploited to simplify the nomenclature and to follow the same ideas, where it is reasonable.

Starting to the simpler structure in biology, the different parameter entering the MWM function are called *genes*.

The *surface roughness genome*, or simply the genome, is the ensemble of the parameters characterizing a rough surface in all its realizations over multiple length scale of observation. The profile characterizing a given length scale, with fixed frequency, will be named *chromosome*. A surface is therefore seen as the superposition of different chromosomes in a sampling length L. The resolution δ adopted is therefore related to the smallest chromosome belonging to this realization.

In this Chapter, the geometrical characterization of chromosomes over multiple length scales it will be firstly addressed, along with the top-down and bottom-up approach to reconstruct a rough profile.

Then, the identification procedure of genomes, i.e the sequencing, will be discussed. The sequencing of surfaces genome is the first key step of the approach presented in this dissertation. Sequencing is formulated as a constrained convex optimization problem, to be solved with efficient quadratic programming (QP) algorithms.

The normal contact response of each chromosome will be characterized in the frictionless normal elastic case using BEM (Sec. 2.2). Following the top-down approach it is possible to identify dominant chromosomes that determine the contact response of a rough profile.

The combination of different individual genomes or chromosomes will lead to a new genome with is own contact response. Thus, an optimized combination will give the opportunity to prototype a new profile/surface with a target behavior. This aspect will be the focus of Chapter 4, based on the results obtained in this Chapter.

3.1 Genome of the multi-scale roughness

An universal description of rough profiles is herein proposed based on a truncated version of the MWM function:

$$Z(x) = \mathcal{A}\sqrt{\frac{\log(\gamma)}{\mathcal{M}}}\left(\frac{2\pi}{\lambda}\right)^{-\mathcal{H}} \times \\ \times \sum_{m=1}^{\mathcal{M}}\sum_{n=n_s}^{n_f}\gamma^{(1-n)\mathcal{H}}\left[\cos(\phi_{m,n}) - \cos(\frac{2\pi}{\lambda}\gamma^{(n-1)}x + \phi_{m,n})\right] \tag{3.1}$$

where, in Eq. (2.2) it is imposed $d = 1$, obtaining $\hat{\boldsymbol{n}} \cdot \boldsymbol{x} = 1 \; \forall m \in [1, \mathcal{M}]$. The rough profile is described by a series of elementary waves, co-sinusoids, with different amplitudes and wavelength, that are defined by a unique combination of the parameters $\mathcal{H}$, $\mathcal{A}$, λ, γ and $\phi_{m,n}$.

In this framework, these parameters are called *genes*. So, the *surface roughness genome* is the overall ensemble of these genes realizing a surfaces over multiple scale of observation. A matrix Φ is so then identified, containing all known $\phi_{m,n}$, that is composed by $\mathcal{M}$ rows and $n_c = n_f - n_s + 1$ columns.

At a given observation length L, a surface realization is obtained thanks to its genome and n_c frequencies, in the range identified by indexes n_s and n_f. These two indexes are somehow related to the observation scale L and the resolution δ chosen to realize the surface.

This chapter proceed in such a way. The multi-scale characterization of profiles is presented Sec. 3.2. Here, the main features of a chromosome, the rough profile identifying a wavelength, are firstly introduced. Then, the multi-scale approaches to reconstruct a rough profile by superimposition of chromosomes are discussed.

The numerical procedure with the aim to identify the surface genome, i.e. the sequencing, will be detailed in the Sec. 3.3. The sequencing will be applied to an artificial profile and to a natural one, introducing the problem of their mechanical interaction over multiple length scales.

3.2 Genetic multi-scale characterization of rough profiles

The multi-scale description of the MWM function in Eq. (3.1) is expressed by the scaling of wavelengths in the frequency domain. This scaling, determining the multi-scale behaviour of roughness, is governed by the genes $\mathcal{H}$, λ, γ. However, if the index n is fixed a single frequency

$$q_n = \frac{2\pi}{\lambda}\gamma^{(n-1)}$$

is identified that it does not depend on m. By increasing n, the corresponding length-scale $\lambda_n = \lambda\gamma^{1-n}$ reduces. So, it is possible to sum up all the sinusoids with the same frequency q_n to identify a profile $\mathcal{C}_n(x)$ which is a representation of roughness at that length scale, i.e.:

$$\begin{aligned}\mathcal{C}_n(x) =& \mathcal{A}\sqrt{\frac{\log(\gamma)}{\mathcal{M}}}\left(\frac{2\pi}{\lambda}\right)^{-\mathcal{H}} \times \\ &\times \sum_{m=1}^{\mathcal{M}} \gamma^{(1-n)\mathcal{H}}\left[\cos(\phi_{m,n}) - \cos\left(\frac{2\pi}{\lambda}\gamma^{(n-1)}x + \phi_{m,n}\right)\right]\end{aligned} \tag{3.2}$$

In biology (Winkler [1920]; King et al. [2006]), a chromosome a structure composed by some genes. Here, in analogy with such a concept, the rough profile $\mathcal{C}_n(x)$ in Eq. (3.2) is called *chromosome* and it expresses the feature of roughness at a the length scale $\lambda\gamma^{1-n}$.

From the definition of chromosome in Eq. (3.2), is therefore possible to rebuild a rough profile $Z(x)$ by summing n_c chromosomes

$$Z(x) = \sum_{n=n_s}^{n_f} \mathcal{C}_n(x) \tag{3.3}$$

with

$$n_c = \lfloor \log_\gamma (N-1) \rfloor \tag{3.4}$$

where $\lfloor\cdot\rfloor$ denotes a lowest integer part of a real function. The value of n_s denotes the chromosomes with longest wavelength realizing the profile at the chosen length scale of observation.

The number on nodes N describing the shape of the profile is imposed always equal to $N = 512$, that is a typical value for modern microscope. In such a way, the number of chromosomes n_c composing a rough profile will be the same at any realization.

Therefore, the length-scale $\lambda_n \gamma^{1-n}$ can not defined until the reference length λ is fixed. So, this reference wavelength is assigned to the chromosome $\mathcal{C}_1(x)$, i.e., the chromosomes with the longest wavelength realizing the the coarser observation length scale known. Then, it holds $\lambda = \lambda_1$.

Thus, at the observation length scale L_i, with $\delta_i = \frac{L_i}{N-1}$, a rough profile is constructed by ranging n between n_s^i and $n_f^i = n_s^i + n_c - 1$ according to the value of λ_1:

$$\begin{cases} n_s^i = \lfloor \log_\gamma(\frac{\lambda_1}{L_i}) \rfloor + 1 \,, \\ n_f^i = \lfloor \log_\gamma(\frac{\lambda_1}{\delta_i}) \rfloor + 1 \,. \end{cases} \tag{3.5}$$

Practically, the genes γ

$$\gamma = \frac{q_{n+1}}{q_n} \,. \tag{3.6}$$

determines the ratio of the wavelengths of two neighbor chromosomes $\mathcal{C}_n(x)$ and $\mathcal{C}_{n+1}(x)$. Once λ_1 and γ are known, the frequency spectrum is defined and chromosomes composing a surface realization at a given observation length are chosen according to Eq. (3.5).

A representative example is now presented, considering three confocal realizations of a surface, which genome is in Tab. 1. The 2D topographies are shown in Fig. 26, each of them with $N = 512$ nodes, and they are centered on $x = 0$ since it always holds $Z(x = 0) = 0$ for the MWM function in Eq. (3.1).

$\mathcal{A}$	$\mathcal{H}$	γ	$\mathcal{M}$	n_s^{10x}	n_f^{10x}	n_s^{20x}	n_f^{20x}	n_s^{100x}	n_f^{100x}
1	0.75	1.50	8	1	16	2	18	6	22

Table 1: Genes imposed to generate three numerical MWM profile, in $N = 512$ nodes, see Fig. 26. For simplicity, it is imposed $\lambda = L$.

The first realization is named $10\times$, with $L_1 = 1 \times 10^{-4}\,\mathrm{m}$, equivalent to $1\,\mathrm{mm}$, depicted by a blue line in Fig. 26.

The second realization is named $20\times$ describes the central part of the $10\times$ profile, in $L_2 = 5 \times 10^{-4}\,\mathrm{m}$, and it is half of its length, i.e. $L_{10\times} = 2L_{20\times}$. This profile is depicted by a black line in Fig. 26 and its topography is shown magnified in Fig. 26.

The third one is named $100\times$ and it describes the central part of the $10\times$ profile in a length scale ten times finer, i.e. $L_3 = 1 \times 10^{-4}\,\mathrm{m}$. At the same time, this realization is five times finer than L_2. This profile is depicted by a red line in Fig. 26.

The three realizations have three different height fields in Fig. 26 since they are composed by superimposing different sets of chromosomes. However, $n_s^{100\times} - n_f^{10\times} = 10$ chromosomes are in common among these realizations, according to data in Tab. (1). More specifically, different acquisition/realizations of the same surface at two profile at different length scales L_i and L_j shares chromosomes if, and only if, $n_f^j - n_s^i > 0$. This observation will be crucial for the sequencing procedure.

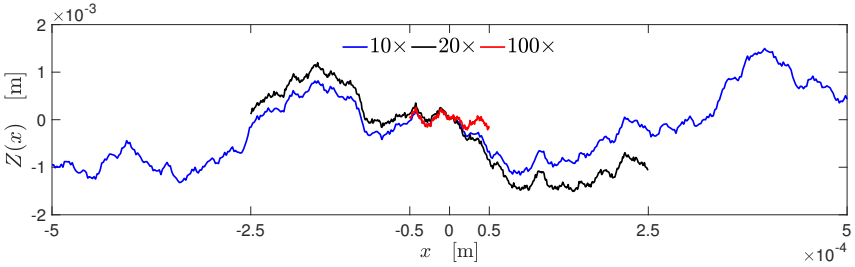

Figure 26: Three confocal realizations, at three different observation length scales, of the same surface with genomes is in Tab. 1 (except phases). The first realization $10\times$ is at the observation length of $L_1 = 1 \times 10^{-3}\,\mathrm{m}$. The second realization $20\times$ is at the observation length of $L_2 = 5 \times 10^{-4}\,\mathrm{m}$. The first realization $100\times$ is at the observation length of $L_3 = 1 \times 10^{-4}\,\mathrm{m}$.

The ten chromosomes in common can be observed from the $\log - \log$ the Power Spectral Density (PSD) of the three profiles (Berry and Lewis [1980]; Wu [2001]. In the the PSDs of this three profiles, which are shown in Fig. 27, these chromosomes must results has peaks in common among all the PSDs.

However, the three realizations present 7 common peaks, highlighted with green arrows. These peaks identify part common chromosomes that contribute to the morphology of each realizations. The remaining 3 chromosomes are the number 5, 6 and 7 since the first part of the PSD at $10\times$ is flat for each realization. These chromosomes are observable from the PSDs at $100\times$ and $20\times$, highlighted with dashed green arrows.

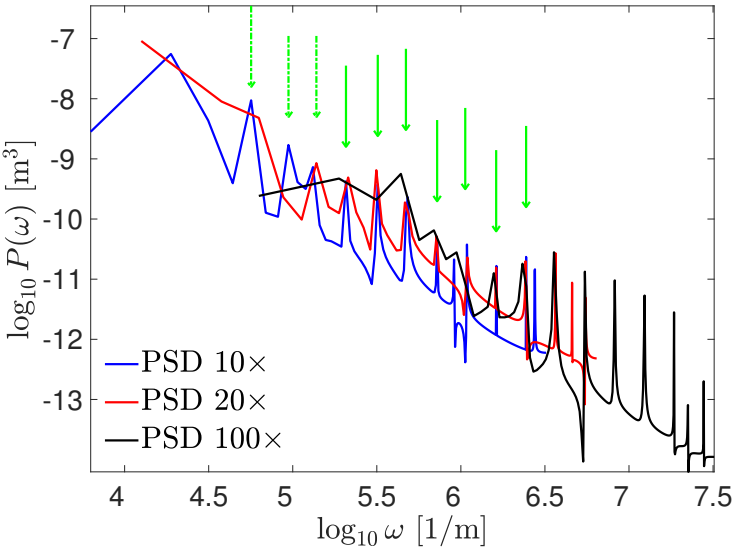

Figure 27: Power spectral densities of the same profile (Tab. 1) visualized at three different realization. Green arrows indicates part of the set of frequencies in common.

3.2.1 Description of a single length scale of roughness

The definition of the chromosome $\mathcal{C}_n(x)$ in Eq. (3.2) allows the description of roughness at each length scale. To visualize this concept, two chromosomes are shown in Fig. 28 for two different values of $n = 1, 2$. Here, the dominant frequency has a wavelength equal to the sample length $\lambda = 100\,\mu\text{m}$ and $\gamma = 1.5$.

The chromosome $\mathcal{C}_1(x)$ is assumed to have a wavelength equal to the sample wavelength, i.e. $\lambda_1 = L = 100\,\mu\text{m}$. This chromosome, depicted by a thick red line in Fig. 28(a), is obtained by summing all the $\mathcal{M} = 8$ co-sinusoids with the associated value $n = 1$ (colored lines) .

The chromosome $\mathcal{C}_2(x)$, depicted by blue line in Fig. 28(b), is obtained as the sum of all the $\mathcal{M} = 8$ co-sinusoids with $n = 2$ (colored lines) . Then, since it is imposed $\gamma = 1.5$, the chromosome $\mathcal{C}_2(x)$ has $\lambda_2 = \frac{\lambda_1}{1.5} = 66.6\,\mu\text{m}$.

The two chromosomes in Fig. 28(a) and 28(b) maintain a co-sinusoidal shape with the wavelength λ_n. A feasible mathematical model of a chromosome in Fig. 28 might be one similar in form to that of the MWM

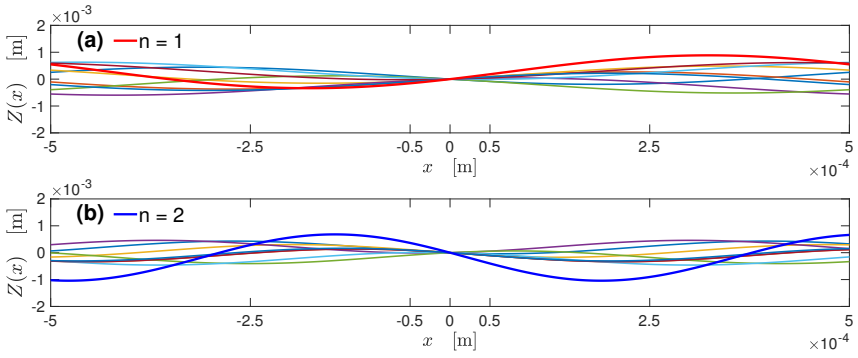

Figure 28: (a) The chromosome $n = 1$ is visualized by the red line and it corresponds to the sum of the other colored cosinusoids. (b) The chromosome $n = 2$ corresponds is shown with a blue line and it corresponds to the sum of the other colored cosinusoids.

function in Eq. (3.1) with $\mathcal{M} = 1$, by introducing the unknown parameters $\mathcal{K}_n, \theta_{n,1}, \theta_{n,2}$:

$$\mathcal{C}_n(x) = \mathcal{K}_n \gamma^{(1-n)\mathcal{H}} \left[\cos(\theta_{n,1}) - \cos\left(\frac{2\pi}{\lambda} \gamma^{n-1} x + \theta_{n,2} \right) \right] . \tag{3.7}$$

A particular case of Eq. (3.7) is when the angles $\theta_{n,1}$ and $\theta_{n,2}$ coincide, say, with the same θ_n. In such a case, a chromosome is described exactly according to the MWM profile in Eq. (3.1) with $\mathcal{M} = 1$. The expressions of $\mathcal{K}_n, \theta_n$ in Eq. (3.7) are obtained imposing $\theta_n = \theta_{n,1} = \theta_{n,2}$ in Eq. (3.7), and are given by:

$$\begin{cases} \mathcal{K}_n = \mathcal{G}_n \sqrt{\mathcal{M} + 2g_{n,3}} \, , \\ \theta_n = \arccos\left(\frac{g_{n,1}}{\sqrt{\mathcal{M}+2g_{n,3}}} \right) , \end{cases} \tag{3.8}$$

where the parameter $g_{n,3}$

$$g_{n,3} = \sum_{i=1}^{\mathcal{M}-1} \sum_{j=i+1}^{\mathcal{M}} \cos\left(\phi_{j,n} - \phi_{i,n} \right) , \tag{3.9}$$

together with the amplitude parameter

$$\mathcal{G}_n = \mathcal{A} \sqrt{\frac{\log(\gamma)}{\mathcal{M}}} \left(\frac{2\pi}{\lambda} \right)^{-\mathcal{H}}$$

and the constants

$$\begin{cases} g_{n,1} = \sum_{m=1}^{\mathcal{M}} \cos(\phi_{m,n}), \\ g_{n,2} = \sum_{m=1}^{\mathcal{M}} \sin(\phi_{m,n}), \end{cases}$$

For its validity, Eq. (3.8) requires

$$|g_{n,1}| \leq \left| \sqrt{\mathcal{M} + 2g_{n,3}} \right| . \tag{3.10}$$

and a numerical simulation has been conducted to verify its validity. This has been evaluated for several values of $\mathcal{M}$, considering each time thousand random choices (uniformly and independently sampled between 0 and 2π) for the phases $\phi_{m,1}$.

Fig. 29 reports, for each such value of $\mathcal{M}$, the percentage of cases for which Eq. (3.10) is satisfied. Its percentage of validity ranges between 88.5% and 98%, with an average value of $\sim 95\%$.

The additional condition $\mathcal{M} + 2g_{n,3} \geq 0$ has not been imposed explicitly, since it always holds. Indeed, $\mathcal{M}+2g_{n,3}$ is the square of the Euclidean norm of the vector with components $(\sum_{i=1}^{\mathcal{M}} \cos(\phi_{i,n}), \sum_{i=1}^{\mathcal{M}} \sin(\phi_{i,n}))$, and this norm is always larger than or equal to 0.

3.2.2 Top-down and bottom-up roughness reconstruction

Chromosomes $\mathcal{C}_n(x)$ are used to reconstruct a realization of a surface by superimposing chromosomes, Eq. (3.3), following a classical top-down (TD) approach or a bottom-up (BU) approach. The TD and BU ways to reconstruct the real profile are just two of the infinite possibilities. Their significance regards the fact they can help in understanding the separation of length scales in contact problems.

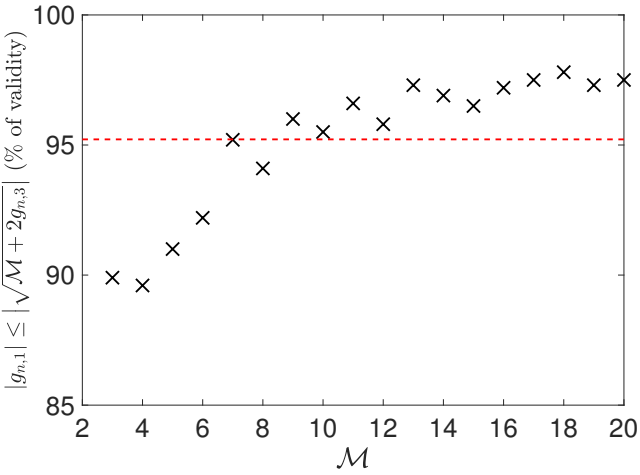

Figure 29: Percentage of validity of Eq. (3.10) over 1000 random choices (uniformly and independently sampled between 0 and 2π) for each value of $\mathcal{M}$. The red line depicts the average range of validity.

An illustrative example of th TD approach is shown in Fig. 30. The superimposition is done starting from the longest wavelength and adding further smaller length towards the finer one.

The rough profile to be reconstructed is depicted through a solid line in Fig. 30, while its successive approximations obtained by summing up all the chromosomes with indexes from n_s up to n_f are depicted through red solid lines. Each chromosome is shown in blue. The resulting profile progressively tends from the top ($n = 1$) to the bottom ($n = 6$). When $n = 1$ holds, the red profile so conceived coincides with $\mathcal{C}_1(x)$.

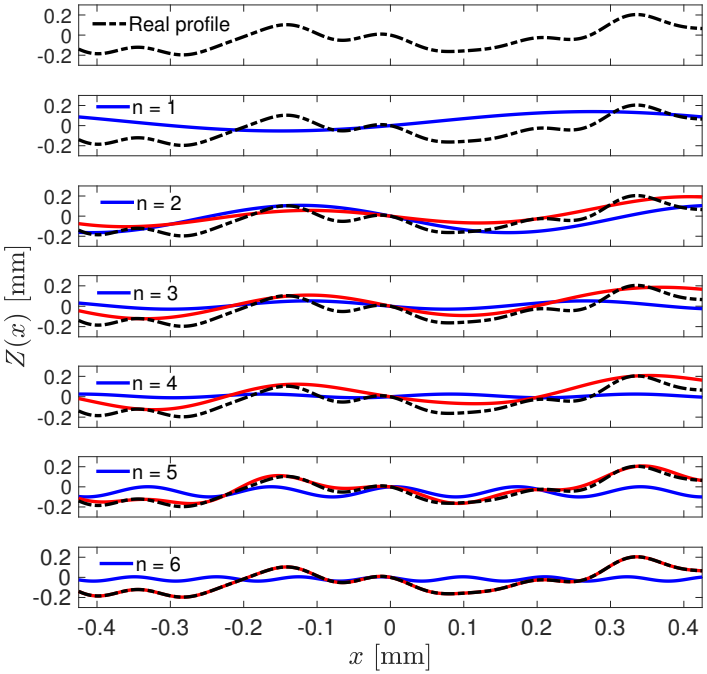

Figure 30: Top-Down (TD) reconstruction of the original profile, represented by the solid or dashed black line.

A Bottom-Up (BU) superimposition approach is also examined. In such a way, the superimposition starts from the shorter wavelength chromosome going towards the longest one. Then the superimposition of chromosomes is made the other way round of the TD approach.

An illustrative example of the BU approach is shown in Fig. 31, considering the same profile used in Fig. 30. Here, the BU starts from the chromosome $\mathcal{C}_6(x)$ and progressively adding, consequently, the chromosome $\mathcal{C}_5(x)$, and so forth. These successive approximations, obtained by adding chromosomes with indexes from n_f up to n_s are depicted through red solid lines. When $n = 6$ holds, the red profile is $\mathcal{C}_6(x)$.

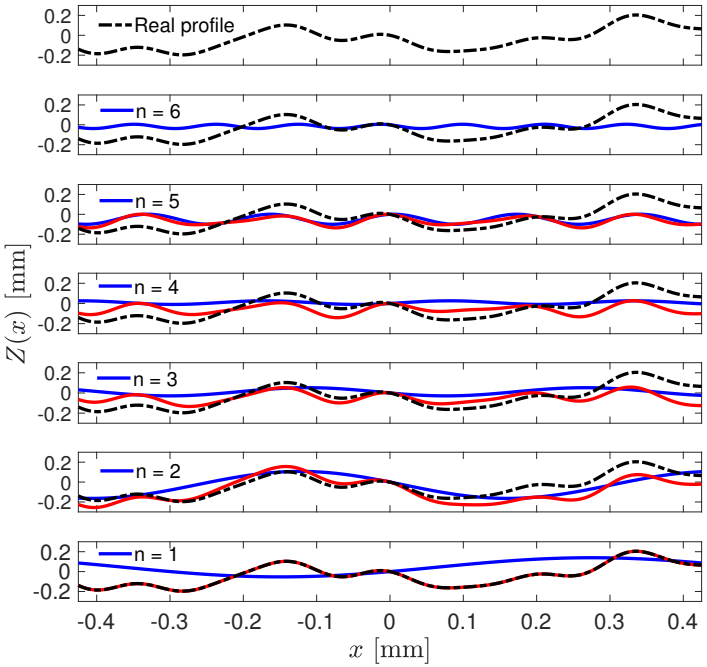

Figure 31: Bottom-Up (BU) reconstruction of the original profile, represented by the solid or dashed black line.

3.3 Genome sequencing

Genome sequencing permits to identify the surface roughness genome, i.e., the genes γ, λ, $\mathcal{H}$, $\mathcal{A}$, $\mathcal{M}$ and $\phi_{m,n}$, which determines the chromosomes of superficial roughness in Eq. (3.1). The number of genes to be identified, $\mathcal{M}n_c$ from Eq. (3.1), is reduced thanks to the definition of chromosome in Eq. (3.2), that is rewritten to Eq. (3.7). In such a case, the sequencing has only $2n_c$, i.e. variables $\theta_{n,1}$ and $\theta_{n,2}$.

However, in the following Section the most general scenario of sequencing is illustrated, for its possible application to 3D roughness, whose mathematical complexity is much higher than for profiles.

3.3.1 Sequencing of a rough profile

A finite series of sinusoids composes a rough profile according to the MWM function in Eq. (3.1). Those sinusoids present a discrete frequency spectrum depending on the index $q_n = \frac{2\pi}{\lambda}\gamma^{1-n}$. Thus, sequencing starts from the analysis of the PSD of a real profile to determine the various parameters that influence the scaling of co-sinusoid in the frequency spectrum: γ, λ and $\mathcal{H}$.

The first step is to identify γ. This parameter determines the density of wavelengths in the frequency domain. The PSD of the MWM function is computed as the square root of the Fast Fourier Transform (FFT), as proposed by Sayles and Thomas [1978]; Berry and Lewis [1980], and takes the following form:

$$\mathcal{P}(\omega) \cong \frac{\mathcal{A}^2}{2}\frac{\log(\gamma)}{\mathcal{M}}\sum_{n=n_s}^{n_f}\frac{2+\delta(\omega-\frac{2\pi}{\lambda}\gamma^{(1-n)})}{(\frac{2\pi}{\lambda}\gamma^{(n-1)})^{2\mathcal{H}}} \tag{3.11}$$

where $\delta(x)$ denotes the Kronecker function only in this case.

As noticed in Sec. 3.2, different realizations of the same profile have a set of wavelengths in common. However, the peaks belonging to each realization do not overlap, due to the non-perfect filtering of the frequency spectrum. To overcome this misalignment, a peak searching algorithm is proposed to locate them, based on the *quickhull algorithm*. This algorithm have been proposed by Barber et al. [1996].

First, the PSD function belonging to each realization is treated separately from the others, to the identify its peaks. Then, the *quickhull algorithm* is applied to retain the common peaks among all the resolutions.

The references peaks are considered to be those of the surface with $20\times$ resolution, because they belong to the central part of the PSD and suffer less on the FFT filtering. This is shown in Fig. 32. Only peaks in the central part of the spectrum overlaps perfectly, and they are used to identify γ.

The frequency density γ is computed as the average distance between the frequencies belonging to this small set of peaks, according to Eq. (3.6). Once the value of γ is determined, the algorithm identifies all the peaks belonging to each acquisition at a distance γ, defining the main wavelengths composing the frequency spectrum. Results of the algorithm are shown by the continuous lines in Fig. 27.

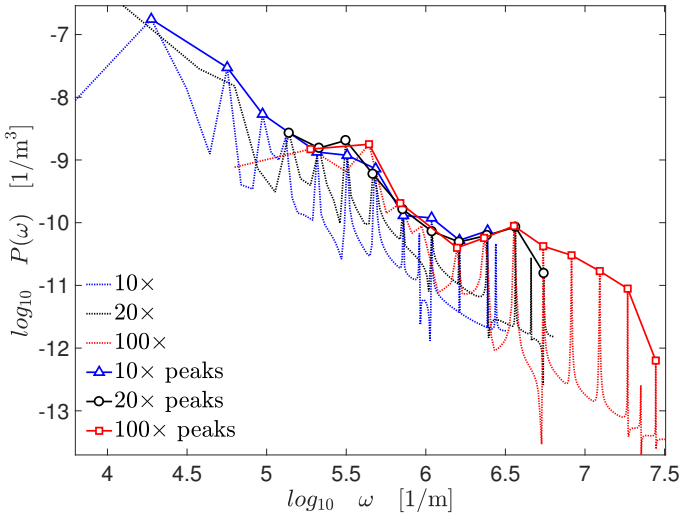

Figure 32: Power spectral densities of the same profile (Tab. 1) visualized at three different realizations, with the results of the algorithm used to identify γ.

The characteristic length λ is determined from Eq. (3.5) by imposing that it belongs the first chromosome corresponds to the first chromosome, i.e. $n^s_{10\times} = 1$.

The gene $\mathcal{H}$ is determined as the slope of the line connecting the peaks retained in the first step of the peak searching algorithm (logarithmic expression of Eq. (3.11)). Here, $\mathcal{H}$ has only a scaling meaning, without any strict self-affine implication. Generally, the parameter $\mathcal{H}$ has the fractal meaning of Hurst coefficient and it is obtained in literature by fitting a continuum form of the PSD in Eq. (3.11)) (see e.g. Berry and Lewis [1980]; Lopez et al. [1994]; Wu [2000, 2001]; Borri and Paggi [2016]).

At this point, the scaling properties of the height field are used to sequence the amplitude $\mathcal{A}$, the number of ridges $\mathcal{M}$, and the phase matrix Φ. Some information of the genome are extracted from two confocal acquisitions $Z_{10\times}(x)$ and $Z_{20\times}(x)$ of the same profile, to reduce the number of variables.

The $Z_{10\times}(x)$ and $Z_{20\times}(x)$ acquisitions have a wide set U_c of chromosomes in common, equal to the difference $n_f^{10\times} - n_s^{20\times}$, as shown in Tab. 1. The set $\bar{U}_c$ is the complementary of U_c and it is the sum of the set U_d containing the frequencies belonging to the $10\times$ realization only, and the set U_t that contains the tail of the PSD of the $20\times$ realization. The set of frequencies U_d plus the ones in U_t but considering its opposite sign, lead to a profile $Z_d(x)$.

From the operative stand point, this profile $Z_d(x)$ is obtained by a purely mathematical subtraction of the height field between the $Z_{10\times}(x)$ and $Z_{20\times}(x)$ confocal realizations, i.e. $Z_d(x) = Z_{10\times}(x) - Z_{20\times}(x)$.

This subtraction is exact because of the MWM model has, by definition, the central point with zero height, i.e. $Z_{10\times}(x = 0) = Z_{20\times}(x = 0) = 0$, that is taken as a origin. The profile $Z_d(x)$ is shown in Fig. 33 by the a continuous red line. The blue line represents the profile $Z_{10\times}(x)$ and the black line represents its finer realization $Z_{20\times}(x)$. The profile $Z_d(x)$ is composed by with $n_c = 3$ chromosomes, one with long and two with short wavelengths but with opposite sign (see Tab. 1).

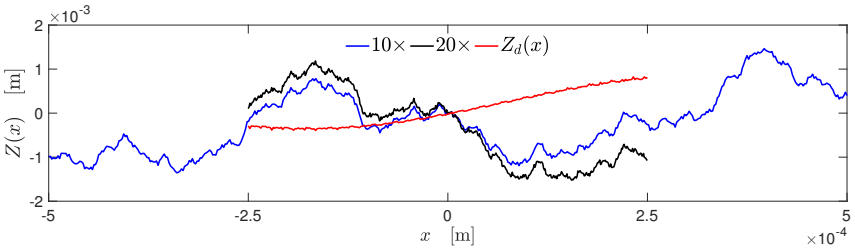

Figure 33: Confocal representation a profile generated with genes in Tab. 1. The profile $Z_d(x) = Z_{10\times}(x) - Z_{20\times}(x)$ is composed by the first chromosome contributing to $Z_{10\times}(x)$, $\mathcal{C}_1(x)$ with long wavelength, and the last two chromosomes, with opposite sign, contributing to $Z_{20\times}(x)$, i.e., $\mathcal{C}_{17}(x)$ and $\mathcal{C}_{18}(x)$ with short wavelength.

An optimization problem to compute $\mathcal{A}$, $\mathcal{M}$ and the first n_c rows of the matrix Φ is now put forward, fitting the real profile $Z_d(x)$ by a parametrized version of the MWM profile. In this way, the identification error is reduced since the profile $Z_d(x)$ gathers data of $\mathcal{A}$ and $\mathcal{M}$ on a small range of wavelengths.

The following parametrized version:

$$\begin{cases} \boldsymbol{Z}_r = \bar{\alpha}\mathcal{A}_0\left[\boldsymbol{A\eta} + \boldsymbol{B\xi}\right] \\ \text{s.t.} \quad \eta_{m,n}^2 + \xi_{m,n}^2 = 1 \end{cases} \tag{3.12}$$

of the MWM is obtained from Eq. (3.1) considering that $\cos(\alpha+\beta) = \cos(\alpha)\cos(\beta) - \sin(\alpha)\sin(\beta)$ and introducing the optimization variables

$$\begin{cases} \eta_{m,n} = \cos(\phi_{m,n}) \\ \xi_{m,n} = \sin(\phi_{m,n}) \end{cases}$$

related to the matrix Φ. The optimization variable $\bar{\alpha}$ is introduced to get a first estimation $\mathcal{A}_0$ of the actual amplitude $\mathcal{A}$, extrapolated from the variance of heights, m_0, of the real profile, along with the hypothesis of an uniform distribution of Φ, see Ciavarella et al. [2004]:

$$\mathcal{A}_0 \simeq \sqrt{\frac{2m_0}{C(\gamma^{-\mathcal{H}})^2}\frac{q^{2\mathcal{H}}}{\log(\gamma)}} \tag{3.13}$$

where

$$C(\gamma^{-\mathcal{H}}) = \frac{\gamma^{-\mathcal{H}n_s} - \gamma^{-\mathcal{H}(n_f^i - n_s^i + 1)}}{1 - \gamma^{-\mathcal{H}}}$$

for the convergence of a geometric series. The matrices $\boldsymbol{A}$ and $\boldsymbol{B}$ in Eq. (3.12) depend on the sampling coordinates as follows:

$$\begin{cases} A_{(m,n),x_j} = \mathcal{G}_n \gamma^{(1-n)\mathcal{H}} \left[1 - \cos(\frac{2\pi}{\lambda}\gamma^{n-1}x_j)\right] \\ B_{(m,n),x_j} = \mathcal{G}_n \gamma^{(1-n)\mathcal{H}} \left[\sin(\frac{2\pi}{\lambda}\gamma^{n-1}x_j)\right] \end{cases} \tag{3.14}$$

The optimization problem used to fit $Z_d(x)$ based on the model function in Eq. (3.12) is such that it minimizes the cost function f:

$$\begin{cases} \min\limits_{\alpha,\boldsymbol{\eta},\boldsymbol{\xi}} & f = || < \frac{(\boldsymbol{Z}_d - \boldsymbol{Z}_r)}{dz} > ||^2 \\ \text{s.t.} & \eta_{m,n}^2 + \xi_{m,n}^2 = 1 \\ \text{with} & n_s^{10\times} \leq n \leq n_s^{20\times} \end{cases} \tag{3.15}$$

where $||\cdot||^2$ indicates the standard Euclidean norm, $<\cdot>$ the mean value and $dZ = \Delta Z_d(x)$ is the profile amplitude.

However, matrices $\boldsymbol{A}$ and $\boldsymbol{B}$ in Eq. (3.14) depend on the number of ridges $\mathcal{M}$. Then, the optimization problem in Eq. (3.15) is solved for each integer of $\mathcal{M}$ between 2 and 20. The best solution among them identifies the number of ridges $\mathcal{M}$, that is the value which minimizes the probability function $P_m(\bar{\alpha}) = \frac{f_m(\bar{\alpha})}{\sum_m^{M_{max}} f_m(\bar{\alpha})}$.

Once $\mathcal{M}$ is sequenced, the parent solution of Eq. (3.15) provides the value of $\mathcal{A} = \alpha_{\mathcal{M}}\mathcal{A}_0$ and the first n_c rows entering the matrix $\boldsymbol{\Phi}$.

Finally, the remaining terms of the matrix Φ are sequenced by imposing a last optimization problem. Reducing the problem only to the two acquisitions $Z_{10x}(x)$ and $Z_{20x}(x)$, the cost function to determine Φ is a weighted sum of the fitting given by Eq. (3.15), where in this case $\bar{\alpha}$ and $\mathcal{M}$ are now known:

$$\begin{cases} \min\limits_{(\boldsymbol{\eta},\boldsymbol{\xi})} & ||f_{10\times} + f_{20\times}||^2 & & \\ \text{s.t.} & \eta_{m,n}^2 + \xi_{m,n}^2 = 1 & & \\ \text{with} & n_s^{10\times} \leq n \leq n_f^{10\times} & \text{for} & f_{10\times} \\ \text{with} & n_s^{20\times} \leq n \leq n_f^{20\times} & \text{for} & f_{20\times} \end{cases} \tag{3.16}$$

The cost function $||f_{10\times} + f_{20\times}||^2$ in Eq. (3.16) might be extended adding other confocal acquisition of the same profile.

Both minimization problems are herein solved by using the *fmincon* function of Matlab [2016], considering only a set of points of the profile for the fitting. Furthermore, all the optimization problems are suitably initialized in the following way to have a faster and more efficient solution. The profile peak is identified and the phase shifting from the origin of the lower frequency sinusoids is computed. The obtained sinusoid is subtracted from the original profile, and the location of its peak is used to compute the phase shifting of the second sinusoids at lower frequencies. Those step has been repeated $\mathcal{M}$ times for each frequency index, to initialize the entries of the phase matrix Φ.

3.3.2 Generalization to rough surfaces

In this subsection the implication on the extension of sequencing to 3D surfaces is discussed. The MWM equation for 3D surfaces has the following expression:

$$Z(x,y) = \mathcal{A}\sqrt{\frac{\log(\gamma)}{\mathcal{M}}}\left(\frac{2\pi}{\lambda}\right)^{-\mathcal{H}} \times \tag{3.17}$$

$$\times \sum_{n=n_s}^{n_c}\sum_{m=1}^{\mathcal{M}} \alpha_m \gamma^{(1-n)\mathcal{H}}\left[\cos(\phi_{m,n}) - \cos(\frac{2\pi}{\lambda}\gamma^{(n-1)}\sqrt{x^2+y^2}\cos(\theta_m)+\phi_{m,n})\right]$$

In this case, the genome parameters are the same as is 2D one. However, ridges are twisted by an in-plane angle θ_m from a reference direction. This angle depends on the inner product $\hat{\boldsymbol{n}}\cdot\boldsymbol{x}$ between the intrinsic phase among ridges θ_m^0 and the direction chosen for the Cartesian axis (O,x,y) for the surface discretization:

$$\theta_m = \tan^{-1}\left(\frac{y}{x}\right) - \theta_m^0$$

However, this does not modify any of the steps related to the sequencing of γ, because of the angles θ_m appear, in the $\log - \log$ realization of the PSD, as a simple difference between the reference frequency. Then, the

peak searching algorithm has not to be modified and γ is be computed as for profiles. In the particular case of a flat PSD, that can be obtained when $\gamma \to 1$, the coefficients characterizing the PSD might be computed from different profiles and takes the average values.

The magnitude $\mathcal{H}$ has to be computed as for rough profiles, considering in this case the x and y direction.

On the other hand, some difficulties arise in the sequencing of $\mathcal{A}$, $\mathcal{M}$, $\mathbf{\Phi}$ and $\mathbf{\Theta}$, the matrix containing the in-plane angles θ_m. Both $\mathcal{M}$, Φ and $\mathbf{\Theta}$ are spatial dependent. Moreover, if the surface is anisotropic, the scaling parameter α_m to modulate the amplitude of each ridge m has to be considered in the optimization problem.

The surface anisotropy can be handled considering a vector $\boldsymbol{\alpha}$ instead of simply the parameter $\bar{\alpha}$ in Eq. (3.12). Also, the coefficients in matrix $\mathbf{\Theta}$ has to be introduced in Eq. (3.12), modifying the related optimization problems in Eq. (3.13) and Eq. (3.16). The MWM parametrized function should read:

$$\begin{cases} \boldsymbol{Z}_{3D} = \boldsymbol{\alpha}\mathcal{A}\left[\boldsymbol{A}\boldsymbol{\eta} + \boldsymbol{B}\boldsymbol{\xi}\right] \\ \text{s.t.} \quad \eta_{m,n}^2 + \xi_{m,n}^2 = 1 \\ \text{with} \quad \Theta_m \in [0, \pi] \quad \forall m \in [1, \mathcal{M}] \\ \text{with} \quad n_s^i \leq n \leq n_f^i \end{cases} \tag{3.18}$$

The condition $\mathbf{\Theta} \in [0, \pi]$ is added, as the problem is symmetric. Angles of the set Θ introduce a nonlinear system to be optimized. This nonlinearity is related to the coefficient matrices $\boldsymbol{A}$ and $\boldsymbol{B}$, whose form is not the same as in Eq. (3.14) and they read:

$$\begin{cases} A_{(m,n),(i,j)} = \mathcal{G}_n \gamma^{(1-n)\mathcal{H}} \left[1 - \cos\left(\frac{2\pi}{\lambda}\gamma^{(n-1)}\sqrt{x_i^2 + y_j^2}\cos(\theta_m)\right)\right] \\ B_{(m,n),(i,j)} = \mathcal{G}_n \gamma^{(1-n)\mathcal{H}} \left[\sin\left(\frac{2\pi}{\lambda}\gamma^{(n-1)}\sqrt{x_i^2 + y_j^2}\cos(\theta_m)\right)\right] \end{cases} \tag{3.19}$$

The parametric form in Eq. (3.18) is used to sequence $\mathcal{A}$, $\boldsymbol{\alpha}$, $\mathcal{M}$ and $\mathbf{\Theta}$, following the same steps as for the profile. As a first step, the optimization problem equivalent to that in Eq. (3.15) is solved to fit $Z_d(x, y)$ with its parametric version in Eq. (3.18).

Two classes of algorithms can be used to efficiently solve the above optimization problems. The *Successive Linear Programming* (SLP) solves iteratively linearized expression of the objective function, see Noceda and Wright [2006]. In this case, the linearized problem is obtained either from ξ and η or preferable from $\boldsymbol{\Theta}$, by updating the coefficient in matrices $\boldsymbol{A}$ and $\boldsymbol{B}$ of Eq. (3.19). However, some difficulties regard in the linearization of the therm

$$\cos(\frac{2\pi}{\lambda}\gamma^{(n-1)}\sqrt{x_i^2+y_j^2}\cos(\theta_m))$$

in Eq. (3.19), introducing recursion.

Another approach could be the *Sequential Quadratic Programming* (SQP) method, whose family of algorithms solves a sequence of optimization subproblems, each one of optimizing a QP of the objective function, see Noceda and Wright [2006].

For example, a very greedy approach of a SQP algorithm to solve the aforementioned problem could be the following. As a first step, the values of $\boldsymbol{\Theta}$ are frozen and the variables to be optimized are $\boldsymbol{\xi}$ and $\boldsymbol{\eta}$. The matrix $\boldsymbol{\Theta}$ is initialized by computing the distance among recursive peaks in the PSD. As a second step, the unknowns become the matrices α and $\boldsymbol{\Theta}$, with the values of $\boldsymbol{\xi}$ and $\boldsymbol{\eta}$ computed as before. Those steps have to be performed iteratively, with the matrices $\boldsymbol{A}$ and $\boldsymbol{B}$ to be updated at each step.

Once $\mathcal{A}$, $\mathcal{M}$ and $\boldsymbol{\Theta}$ are provided by the first algorithm, matrices $\boldsymbol{A}$ and $\boldsymbol{B}$ have fixed coefficient, since $\boldsymbol{\Theta}$ is known from the first optimization problem. Then, only the coefficients in the matrix $\boldsymbol{\Phi}$ are unknown to be identified, exactly in the same way as for the rough profiles.

In the following, the complete sequencing procedure is applied to rough profiles to have a proof of concept about its applicability on surfaces.

3.4 Sequencing and reconstruction of profiles

Two different rough profiles are now considered. The first one has been numerically generated, to validate the sequencing procedure. The second one is sequenced from a fractured alloy surface. Then, for the coarsest realization with these two genomes, the frictionless contact response is investigated (see Sec. 2.2), whose results are compared with the ones of constitutive chromosomes composing them. In both cases, the contact mechanics is investigated only for the $10\times$ realization/acquisition, with $E^* = 210\,\mathrm{MPa}$. To simplify the visualization of results, only the first ten chromosomes are considered. Differences between TD and BU profile reconstructions are discussed, to show the differences between the two approaches from a contact mechanics perspective.

3.4.1 Application to artificial roughness

A representative artificial MWM profile is herein realized over a coarser length scale $L_1 = 1 \times 10^{-4}\,\mathrm{m}$, namely $10\times$, $L_2 = 5 \times 10^{-4}\,\mathrm{m}$ ($20\times$) and $L_3 = 1 \times 10^{-4}\,\mathrm{m}$ ($100\times$). The genome is collected in Tab. 2 and $N = 512$ discretization nodes are used in each realization. Also, the identified genes after sequencing are presented in Tab. 2. The values of genes γ, $\mathcal{H}$ and $\mathcal{A}$ have been accurately identified.

	$\mathcal{A}$	$\mathcal{H}$	γ	$\mathcal{M}$	$n_s^{10\times}$	$n_c^{10\times}$	$n_s^{20\times}$	$n_c^{20\times}$
numerical	1	0.75	1.50	8	1	16	2	18
sequencing	1.04	0.73	1.49	8	1	16	2	18

Table 2: Genes imposed and obtained to generate the numerical profile to prove sequencing.

The numerical profile and the sequenced one are depicted in Fig. 34 for the realization at $10\times$ and in Fig. 35 for the realization at $20\times$.

In both Fig. 34 and Fig. 35, the profiles obtained from the sequencing (dashed–dot red line) overlaps the numerical profile (black line). The relative r.m.s. error between the two profiles at $10\times$ is equal to 5% and, for the realization at $20\times$, is around 3%.

In both cases, the sequencing seems to behave as a low pass filter of the complete one, since the fitting nodes are taken spaced equally in the domain. This low pass filter behavior can be corrected by refining nodes in appropriate regions focusing on the topological features of the profile. Also, the minimum distance between nodes has to be selected according to the shorter wavelength, belonging the latest chromosome in this realization of the surface.

Here, the simplest situation is considered since the aim of this example is to show the general applicability of sequencing, to introduce the study of superimposition of chromosomes realizing a rough profile at the chosen observation length scale.

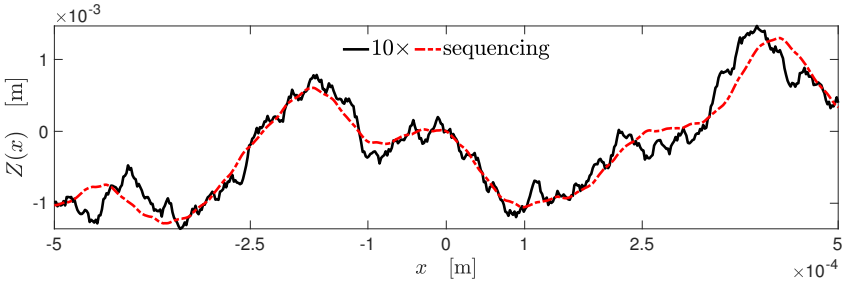

Figure 34: Topography of the $10\times$ realization of the artificial profile (dashed black line) and the one obtained from the sequencing (red dashed line).

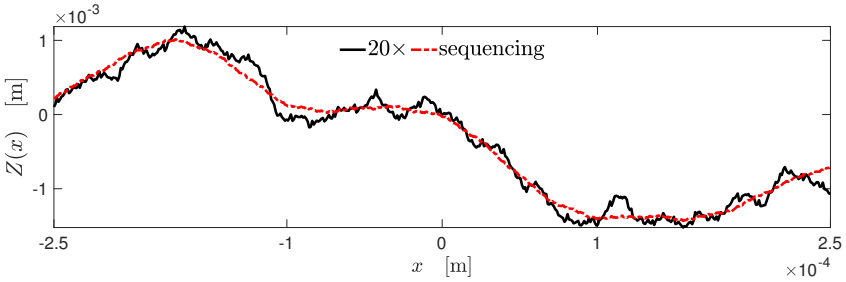

Figure 35: Topography of the $20\times$ realization of the artificial profile (dashed black line) and the one obtained from the sequencing (red dashed line).

So, to investigate the effect of superimposition of length scales, the frictionless normal contact problem is solved via BEM (Sec. 2.2, with twenty equipoised rigid body displacement for each peak-valley amplitude) for both the numerical profile and the one obtained from sequencing. The elastic Young Modulus of a generic alloy is used, i.e. $E = 210\,\mathrm{MPa}$. The mechanical evolutions of the $10\times$ realization are considered, in terms of $A(p)$ and $K(p)$ evolutions, i.e. contact area A and stiffness K vs pressure p.

In Fig. 36, the red line belong to the numerical genome, whereas the red line corresponds to the sequenced one. Both evolutions are very close to each other, although they differs at around $p \approx 1 \times 10^{-4}\,\mathrm{N/m}$.

The mechanical evolutions of the first 10 chromosomes contributing to this realization are also shown in Fig. 36 by different colors. Some chromosomes has a similar trend respect ot the one of the complete profile. For example, for $p > 1 \times 10^{-4}\,\mathrm{N/m}$, the $\mathcal{C}_2(x)$ has a trend parallel to the complete $A(p)$ and $K(p)$.

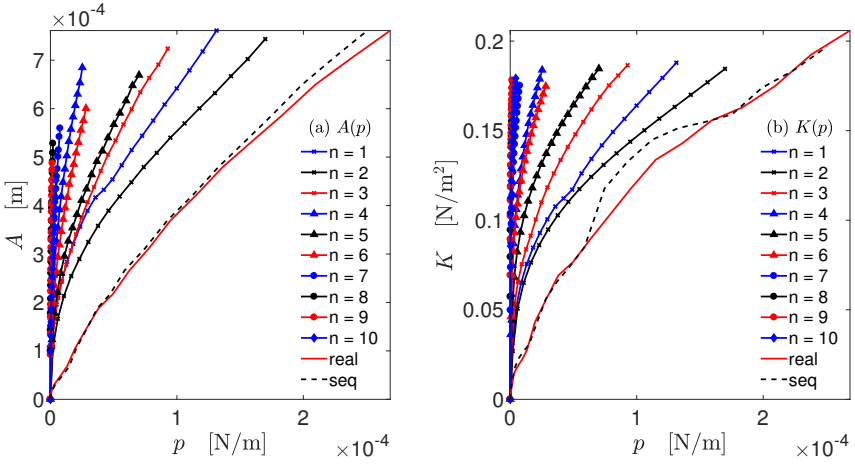

Figure 36: Contact evolutions of the sequenced genome in Tab. 1, for the $10\times$ realization and for the related first 10 chromosomes.

The effect of superimposition is now investigated by considering TD (Fig. 30) or the BU (Fig. 31) approaches. The mechanical response of the intermediate profile composed by superimposing sequentially chromosomes is computed. This intermediate profile is shown by the red lines in Fig. 30 and Fig. 31.

Results are presented in Fig. 37 for the $A(p)$ evolution, where the black line denotes the $A(p)$ evolution of the complete realization.

In Fig. 37(a) the TD approach is considered. The first profile simulated, dashed blue line with cross marker, is obtained by summing up the chromosomes $n = 1$ to $n = 1$. So, in such a case, this curve represent the evolution of $\mathcal{C}_1(x)$. The second evolution, dashed back line with cross marker, refers to the profile obtained by summing up the chromosomes $\mathcal{C}_1(x)$ and $\mathcal{C}_2(x)$. The other evolutions are obtained in the same way.

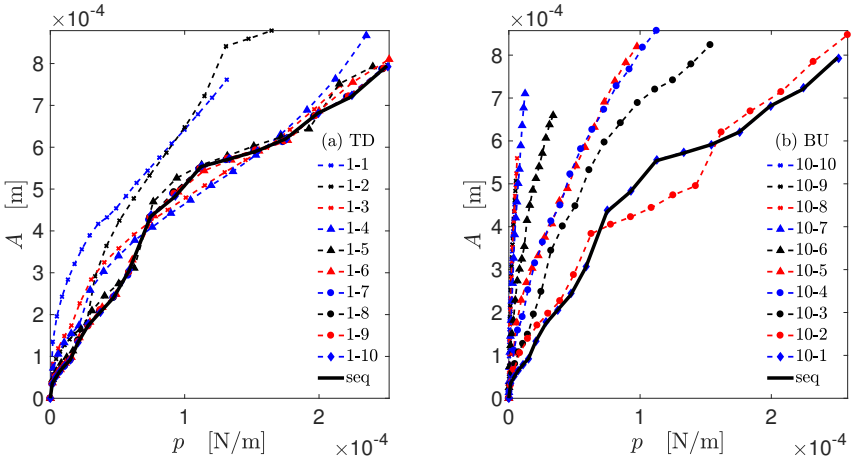

Figure 37: $A(p)$ evolution of the sequenced genome in Tab. 1, for the complete $10\times$ realization and the intermediates profiles reconstructed following the (a) TD approach and (b) BU approach. The intermediate profile is obtained by summing chromosomes from the first to the second index, solving the contact problem in its peak-valley amplitude.

On the other hand, in the BU approach the superposition starts in the opposite way around, see Fig. 37(b). So, the first profile simulated is the chromosomes $\mathcal{C}_{10}(x)$ whereas the the second one is obtained by summing up the chromosomes $\mathcal{C}_{10}(x)$ and $\mathcal{C}_9(x)$.

Only few chromosomes are needed to overlap the $A(p)$ curve using the TD reconstruction, as shown in Fig. 37(a). The $A(p)$ evolution of the reconstructed profile overlaps exactly the complete one after the chromosomes $\mathcal{C}_6(x)$ is superimposed, as for the $K(p)$ evolution in Fig. 38(a).

On the contrary, the BU approach over-estimates $A(p)$ until the chromosomes $\mathcal{C}_2(x)$ and $\mathcal{C}_1(x)$ are added, see see Fig. 37(b) and Fig. 38(b). In this case, both contact area and stiffness are largely over-estimated for low contact pressures, Therefore, the error in approximations is mitigated only by adding at chromosomes $\mathcal{C}_2(x)$ and $\mathcal{C}_1(x)$. For $\mathcal{C}_2(x)$ the difference is still remarkable while the two curve overlaps when chromosome $\mathcal{C}_1(x)$ is superimposed.

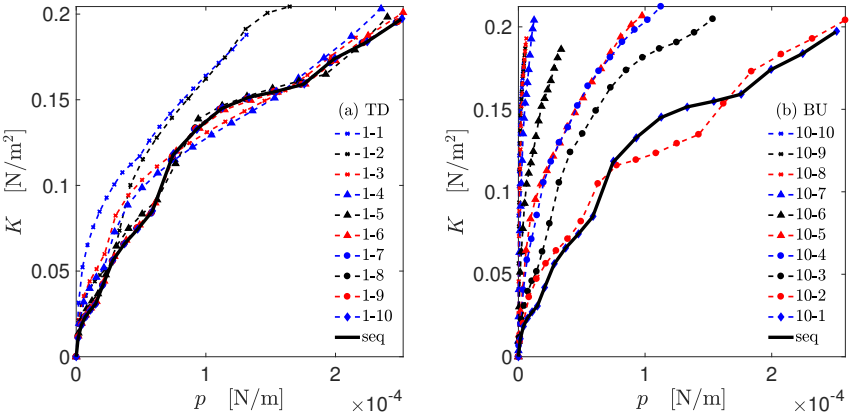

Figure 38: $K(p)$ evolution of the sequenced genome in Tab. 1, for the complete $10\times$ realization and the intermediates profiles reconstructed following the (a) TD approach and (b) BU approach. The intermediate profile is obtained by summing chromosomes from the first to the second index, solving the contact problem in its peak-valley amplitude.

Comparing both approaches, the superimposition of $\mathcal{C}_1(x)$ and $\mathcal{C}_2(x)$ is fundamental to define the mechanical behavior of the complete profile. The rough profile obtained by summing up only chromosomes $\mathcal{C}_1(x)$ and $\mathcal{C}_2(x)$ is enough to give a close approximation to the $K(p)$ and $A(p)$ curves of the original profile. This profile is shown by a dashed black line with red marker in Fig. 37(a) and Fig. 38(a). Only small features of the complete profile are missing, that can be considered adding more chromosomes.

Moreover, it is noticeable that the TD approach is more accurate than the BU to estimate the normal contact stiffness curve, which is a result consistent with the fact that long wavelengths are dominating this quantity over fine scale roughness, see Barber [2003]; Paggi and Barber [2011]. Also, it is possible to appreciate from Fig. 38(a) how much is the error in neglecting some chromosomes, helping in understanding how many components of roughness have to be taken into account for practical engineering applications.

Thus, to highlight the role of single chromosome in the mechanical response, it is computed the correlation coefficient c_n between the mechanical y curve of the complete profile and the intermediate profile y_n. This profile is obtained summing n chromosomes according to a TD or BU approaches. Results are shown in Fig. 39(a) for the TD approach and in Fig. 39(b) for the BU reconstruction approach. The black curves with cross markers denote the $K(p)$ evolutions and the blue one with point markers the $A(p)$ curve.

The TD approach gives a reasonable approximation of the original curve in both $K(p)$ and $A(p)$ evolutions, mostly when chromosome $\mathcal{C}_6(x)$ is considered. The BU approach is not able to describe the $K(p)$ curve until the $\mathcal{C}_1(x)$ and $\mathcal{C}_2(x)$ are summed up, as observed before. Moreover, the $A(p)$ evolution for the BU process has a peculiar trend. The approximation of the $A(p)$ evolution is very efficient also when the latest eight chromosomes with shortest wavelength are considered.

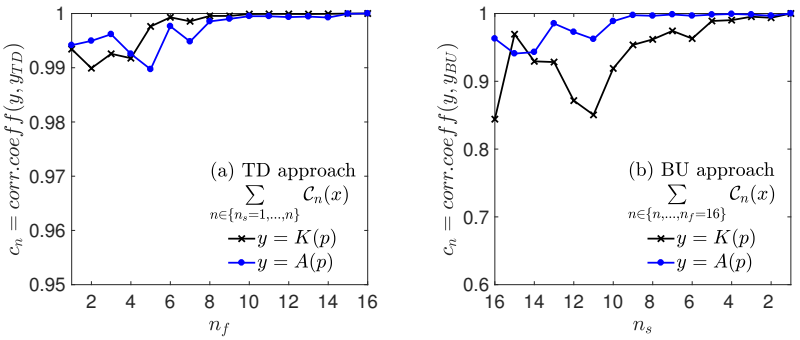

Figure 39: Correlation coefficient between the mechanical evolution y of the complete profile with the one y_n of the intermediate profile obtained following (a) the TD or (b) the BU approach.

The superimposition of chromosome with different wavelength is fundamental to represents the contact area morphology, in accordance on what found by Yastrebov et al. [2015, 2017a], who investigated the contact area evolution during contact. According to his results, obtained by varying the grid resolution, surfaces that present a higher lower cut off develop a bigger contact area. Here, the same experiment is performed by following the BU approach, but considering the same grid resolution, confirming his findings. Also for the $A(p)$ evolutions, the longest waves are crucial to estimate the contact area.

3.4.2 Application to natural roughness

Sequencing is herein applied to a real rough profile extracted from a fracture surface of steel alloy with the LEICA DCM3D confocal profilometer, available in the MUSAM-Lab at the IMT School for Advanced Studies Lucca, to show the general applicability of sequencing also to a real rough profile. The present approach is not limited to a specific technique and any other instrument could be used to sample a surface, such as the Atomic Force Microscope (AFM).

The LEICA DCM3D confocal profilometer is equipped with three different sets of lenses (providing $10\times$, $20\times$ and $100\times$ magnifications, respectively), which enables us to sample the same surface at different resolution, as presented in Fig. 40. The LEICA DCM3D confocal profilometer acquires square surface samples of side L with 512×512 sampling nodes. The in-plane sampling length is $L_1 = 849.42\,\mu\text{m}$, $L_2 = 424.96\,\mu\text{m}$ and $L_3 = 84.99\,\mu\text{m}$ for each magnification, respectively.

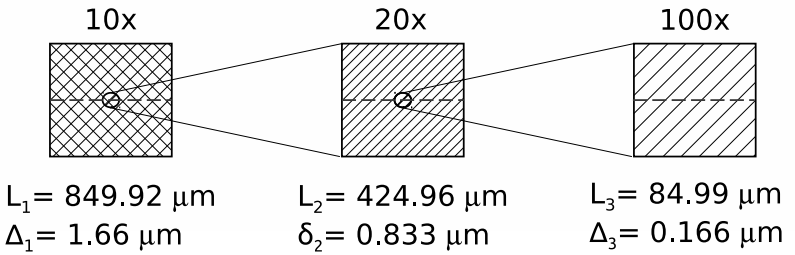

Figure 40: Operating principle of the LEICA DCM3D confocal profilometer available in the MUSAM-Lab at the IMT School for Advanced Studies Lucca. Each acquisition divides the sample L_i in 512 nodes. The vertical resolution is of $2\,\mu\text{m}$, $1\,\mu\text{m}$ or $0.2\,\mu\text{m}$ respectively.

Sequencing is applied to a fracture surface of steel alloy. The central profiles at the three confocal realizations in Fig. 40 are considered. The first step of sequencing is to compute the PSD at each resolution and then to find the peaks of the PSD thanks to a peak searching algorithm. The peaks are at distance γ and the mean slope of lines connecting them is twice the value of the parameter $\mathcal{H}$.

The extracted of the profile $Z_d(x)$ is shown in Fig. 41 (red line). This profile is identified by 6 chromosomes with long wavelength, according to the values of genes obtained presented in Tab 3. The shape of $Z_d(x)$ in Fig. 41 suggests that in reality it is composed by a bigger set of frequencies, confirming what discussed in Sec. 3.3, that sequencing of 3D surfaces should be done by considering additional features.

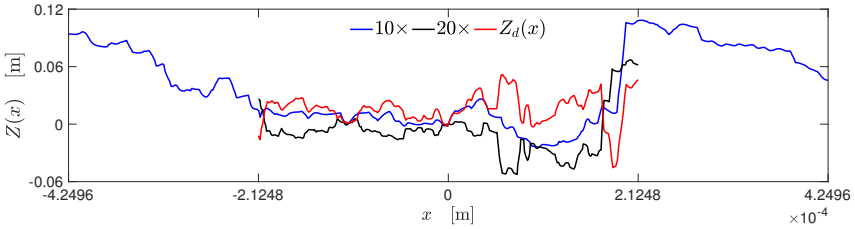

Figure 41: Extraction of the profile $Z_d(x) = Z_{10\times}(x) - Z_{20\times}(x)$ for the fractured alloy considered.

Moreover, it is interesting to notice the effect of superimposition of scales in Fig. 41, focusing on the local peak at $x = 0.05\,\mathrm{mm}$ of the $10\times$ realization. This peak is not present in the realization at $20\times$, but is clearly evident in the profile $Z_d(x)$. This local peak is generated by the superimposition of chromosomes with longest wavelength and it is possible to extract their contribution as done with the profile $Z_d(x)$, changing the resolution of the profilometer.

The profile obtained after the sequencing is shown in Figs. 42 and 43 by the red line for the $10\times$ and $20\times$ acquisition of the profiles. In both cases, the relative r.m.s difference between the sequenced profile and the original one is around the 7%.

The most evident difference is located at around $x = 0.2\,\mathrm{mm}$, where the profile suddenly changes its slope. This region coincides with the last points of the realization at $20\times$ where, also in this case, the sequenced profile is quite different. This is kind of error might be related by many factors. The most feasible one is that, also in this case, 128 points at equipoised distance are taken to perform the fitting.

$\mathcal{A}$	$\mathcal{H}$	γ	q_0 $[\mathrm{m}^{-1}]$	$\mathcal{M}$	$n_s^{10\times}$	$n_c^{10\times}$	$n_s^{20\times}$	$n_c^{20\times}$
457.63	0.90	1.18	5190.5	10	1	38	5	42

Table 3: Genome of the fractured alloy surface

Particularly, this surface was choice to show how it is important to chose correctly the fitting nodes and this it can be done only after a comprehensive investigation of roughness local features. The choice of the number of points, their distance and local refining has to be done considering the chromosome shortest wavelength realizing the rough profile. Also, since the peak at $x = 0.05\,\mathrm{mm}$ is caused by few chromosomes, the refining can be avoided in the $10\times$ fitting but it is needed in the first one of $Z_d(x)$.

The mechanical interaction of chromosomes is herein investigated following the same approach as the artificial profile discussed in Sec. 3.4.1. The frictionless elastic normal contact problem is solved by considering the composite Young modulus of $E^* = 210\,\mathrm{MPa}$.

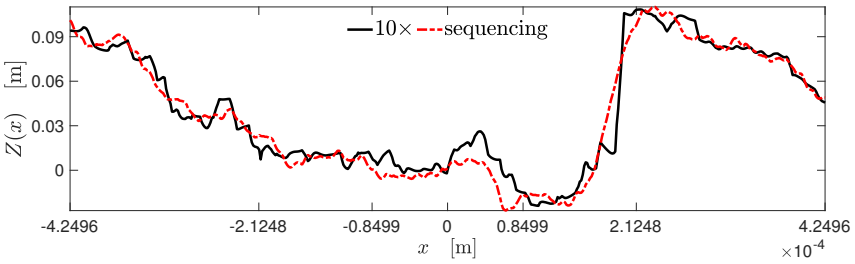

Figure 42: $10\times$ acquisition from fractured interface of an alloy surface.

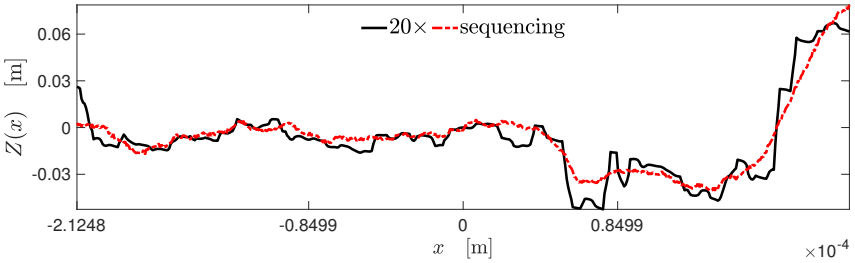

Figure 43: $20\times$ acquisition from fractured interface of an alloy surface.

The $A(p)$ and $K(p)$ evolutions of the sequenced profile (black dashed line) and of the real one (red line) are compared in Fig. 44(a) and in Fig. 44(a) respectively. Also in this case, both evolutions are almost overlapped by the one obtained from the sequenced profile. Moreover, the $A(p)$ and $K(p)$ evolutions of the first 10 chromosomes contributing to this realization are also shown in Fig. 44.

Some chromosomes have features in common to the complete evolution. For instance, the $A(p)$ evolution changes its slope at around $p \approx 2\,\mathrm{N/m}$, see in Fig. 44(a). Chromosomes $\mathcal{C}_2(x)$ and $\mathcal{C}_3(x)$, depicted by the black and red line, respectively, with cross marker are the only presenting a similar change of slope at $p \approx 2.5\,\mathrm{N/m}$.

At the same time, chromosomes $\mathcal{C}_7(x)$ and $\mathcal{C}_{10}(x)$, depicted in Fig. 44 by the blue line with round and diamond respectively, have an asymptotic trend very similar to one of the complete profile after the change in slope at $p \approx 2\,\mathrm{N/m}$.

The same observations holds for both pairs of chromosomes looking at the $K(p)$ in Fig. 44(b).

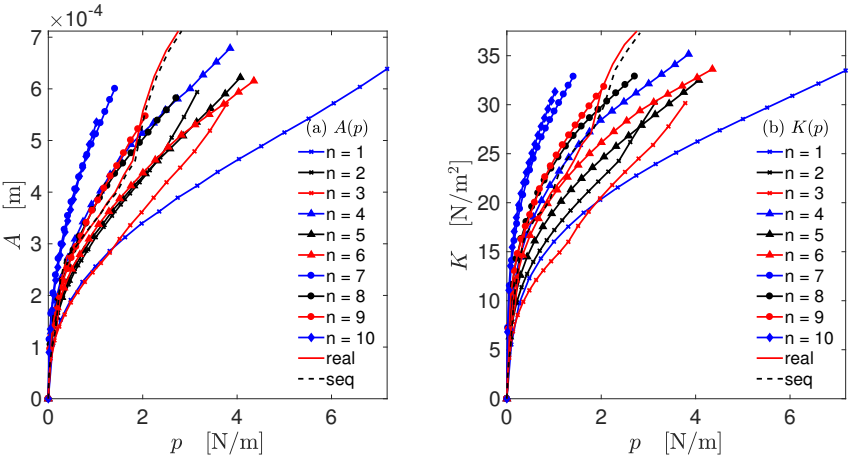

Figure 44: Contact evolutions of the fractured alloy 10× realization, sequenced genome in Tab. 3, considering its first 10 chromosomes.

In this case, instead to compare TD and BU approaches, the following investigation will focus on the influence of chromosomes on the mechanical response of the complete profile. However, also in this case the TD approach shows a better approximation of the contact mechanics of the complete profile than the BU approach for the frictionless elastic normal case, discussed in Sec. 3.4.1.

The first step forward in this analysis is presented in Fig. 45. The correlation coefficient c_n between the mechanical response y_n of the $n-th$ chromosomes with the same mechanical response y of but for the complete realization of the profile. In Fig. 45, the black curve with round marker denotes c_n for each chromosome with the complete $K(p)$ evolution. The blue curve denote it but in the case of the $A(p)$ evolution.

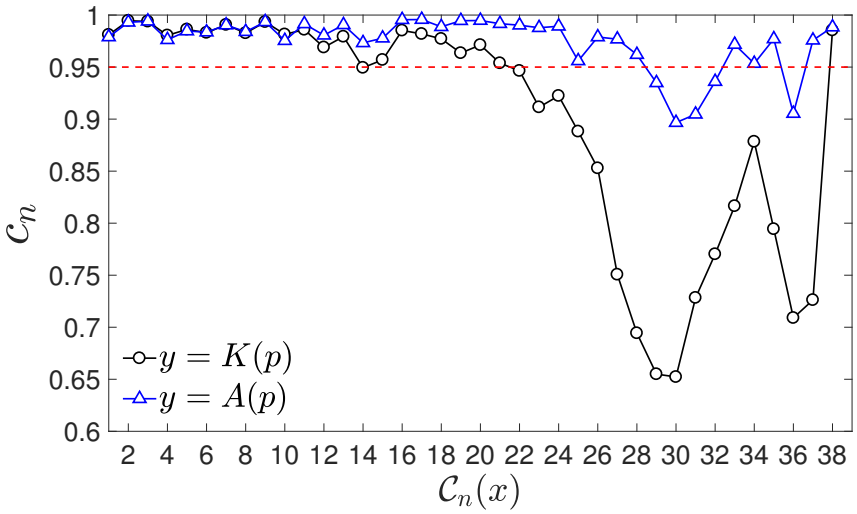

Figure 45: Correlation coefficient between the $K(p)$ and $A(p)$ curves of a single chromosome $\mathcal{C}_n(x)$ the parent one y of the complete 2D realization of the fractured alloy, which genome is in Tab. 3. The red line represent the threshold correlation value of $c_n = 0.95$.

It is possible to observe in Fig. 45 that chromosomes referring to length scales with $n < 20$ have a correlation coefficient greater than $c_n > 0.95$ with $K(p)$ evolution. However, chromosome $\mathcal{C}_{38}(x)$ has a correlation coefficient greater than 0.95, while for $\mathcal{C}_{14}(x)$ is a bit less than 0.95.

For the $A(p)$ curve also all the chromosomes with $n < 28$ and with $n > 32$, except of $\mathcal{C}_{36}(x)$, have a correlation coefficient up to 0.95 with the complete $A(p)$ curve. Also, observing the $K(p)$ correlation, those chromosomes with $n > 32$ have an increasing value of c_n.

Four case studies useful then are proposed in Fig. 46, in terms of $K(p)$ and $A(p)$ evolutions. Here, the evolution related to the complete realization are shown by the black line for both $K(p)$ and $A(p)$ evolutions.

The first $K(p)$ evolution is computed for the rough profile obtained by subtracting chromosome $\mathcal{C}_1(x)$, $\mathcal{C}_2(x)$ and $\mathcal{C}_3(x)$ to the complete realization $Z(x)$. Chromosome $\mathcal{C}_2(x)$ and $\mathcal{C}_3(x)$ might determine the change in slope at $p \approx 2\,\mathrm{N/m}$, observing their trend in Fig. 44. Also, they have the higher value of correlation coefficient with both $K(p)$ and $A(p)$.

The evolution so obtained is shown with dashed blue line with triangle marker in Fig. 46(a) and in Fig. 46(b) for $K(p)$ and $A(p)$, respectively. Both evolutions does not show a change in slope at around $p \approx 2\,\mathrm{N/m}$. Thus, the chromosomes $\mathcal{C}_2(x)$ and $\mathcal{C}_3(x)$ determine this change.

The second $K(p)$ evolution is obtained in a similar way of the previous one. However, in this case, it is computed for the profile obtained subtracting from the genome chromosomes $\mathcal{C}_7(x)$ and $\mathcal{C}_{10}(x)$. These chromosome showed in Fig. 44 a trend parallel to the asymptotic one of the complete curve, after $p \gtrsim 2\,\mathrm{N/m}$.

The evolution so obtained is shown with dashed blue line with round markers in Fig. 46(a) and in Fig. 46(b). In this case, both $K(p)$ and $A(p)$ overlaps the complete curve for $p \lesssim 2\,\mathrm{N/m}$. However, for $p \gtrsim 2\,\mathrm{N/m}$ it diverges from the complete curve in both $K(p)$ and $A(p)$ evolutions. Thus, the chromosomes $\mathcal{C}_7(x)$ and $\mathcal{C}_{10}(x)$ influence the mechanical evolution of the profile for $p \gtrsim 2\,\mathrm{N/m}$.

In the third evolution, the profile realization obtained by neglecting chromosome $\mathcal{C}_{14}(x)$. The evolution so obtained is shown with dashed blue line with low triangle markers in Fig. 46(a) and in Fig. 46(b). The complete curve is completely overlapped by the evolution obtained neglecting chromosome $\mathcal{C}_{14}(x)$. This chromosome, that has $c_n < 0.95$, affects minimally the mechanical evolution of the complete profile.

The four and last evolution is the mechanical response of the profile composed by all chromosomes with a correlation coefficient grater than 0.95 with the $K(p)$ curve. This evolution is depicted with dashed red line with cross markers in Fig. 46(a) and in Fig. 46(b). In these case, both $K(p)$ and $A(p)$ evolutions are approximated accurately all the features visible. Then, the profile composed by summing all chromosomes with $c_n > 0.95$ provides an accurate approximation of the contact mechanics of the complete realization in frictionless normal elastic case.

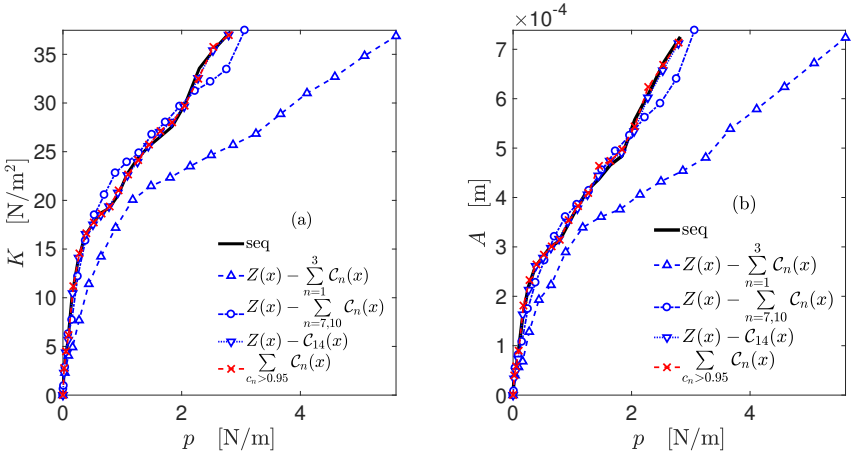

Figure 46: Alloy fractured surface, (a) $K(p)$ and (b) $A(p)$ evolutions of the $10\times$ realization. Four case studies are considered: three different sets of specific chromosomes are removed and the case when only chromosomes with a correlation coefficient greater than 0.95 with the $K(p)$ curve are retained.

3.5 Concluding remarks

In this Chapter, the basis concepts of a genetic analysis of surfaces has been proposed. The fundamental definitions have been provided, simplifying the description of the multi-scale roughness by introducing the chromosome. Roughness has been reconstructed following either the top-down and bottom-up processes. The TD approach is more efficient and accurate to describe the contact mechanics of original profile than the BU one.

Sequencing of the alloy fracture surface highlighted the observation that the simple model provided from the MWM might be not enough accurate in certain cases, where some other genetic features of roughness or textures present. For example, a rough surfaces might be modeled with two different MWM, rather two different combination of chromosomes, to which belongs different pair $(\gamma_1, \mathcal{H}_1)$ and $(\gamma_2, \mathcal{H}_2)$ and different set of angles $\mathbf{\Phi}_1$ and $\mathbf{\Phi}_2$.

Then, methods to combine different genome to obtain specific kind of mechanical response are helpful to enrich the sequencing procedure. For example, the fitting in Eq. (3.15) or in Eq. (3.16) might be coupled with some condition on either of the $K(p)$ or $A(p)$ relations, to identify some *genetic markers* of the profile that give basic informations on the kind of chromosomes that are composing this profile. Also, a practical investigation with the use of any acquisition microscope can be done to empathized the features of roughness over multiple length scales of observations, as discussed for the alloy realizations. Moreover, from a modeling stand point, it might be possible that fracture introduces particular features in the roughness, that can be handled by providing a modified version of the MWM function.

However, a specific analysis of separation of length scale of roughness is needed before addressing efficiently and exhaustively these following steps. Thus, a comprehensive step on this direction will be the focus of the next Chapter.

Chapter 4

Roughness optimization

In this Chapter, the role of different length scales composing the superficial roughness is investigated, considering its constituents, the chromosomes. Roughness has been categorized in two components, macro- and micro-scale contributions, according to their role on the mechanical response of a rough profile.

After that, the focus will be the engineering of surface roughness. It will be shown that new genomes can be generated by combining pre-existing genomes, taken from a database, to obtain a rough profile that presents a target mechanical response. Three different approaches are herein proposed to pursuit this objective. The first method consists in a Simple Optimization of Genes (SOG). The second methods choses the genomes that present a response which is the closest to the target contact behavior to reproduce, within a range of intervals. The combination of this genomes is called Genome Cross-Over (GCO), by exploiting similarity with biology. The third method is similar to the genome cross-over but mixes directly chromosomes, i.e., it is a Chromosomes Cross-Over (CCO). Those methods are compared in relation to two case studies.

Finally, the Mixed Chromosomes Cross-Over (M-CCO) is proposed to roughness achieving two targets on two separate mechanical evolutions.

4.1 Mechanical multi-scale roughness characterization

An accurate characterization of multi-scale roughness will open the possibility to generate new optimal pattern of roughness with a target mechanical response. The first step forward on this topic is given in Chapter 3, where the fundamental definition of surface roughness genome are introduced. In this framework, the geometrical features of roughness at a given observation length scale are associated to the co-sinusoidal topography of a chromosome $\mathcal{C}_n(x)$, see Sec. 3.2, with wavelength

$$\lambda_n = \lambda_1 \gamma^{1-n}$$

that is defined hence the reference wavelength λ_1 is assigned. In Sec. 3.2, the wavelength λ_1 has been assigned to the longest wavelength contributing to larger realization available of a surface, i.e. to the first chromosome $\mathcal{C}_1(x)$ of the genome. Increasing n, the gene γ is responsible to the reduction in wavelength λ_n of the associated chromosome $\mathcal{C}_n(x)$.

Considering a given observation length, roughness is realized superposing different chromosomes, depending also on the resolution used to characterize the profile. The top-down and the bottom-up superimposition approaches are proposed in Sec. 3.2.2. Their comparison of these approaches highlights the role of chromosomes in the mechanical response of a rough profile.

More specifically, it is considered in Fig. 46 the mechanical response of a rough profile from a fractured alloy surface. It is shown that its mechanical behavior have a reasonable approximation in the mechanical behavior of the rough profile obtained summing up chromosomes with a $K(p)$ evolution correlating up to 0.95 with one of the complete profile. These chromosomes are related mainly to the longest wavelengths in the frequency spectrum. In a similar way, Paggi and Barber [2011] demonstrated that the $K(p)$ evolution is ruled by the longest wavelengths of the profile, determining its *waviness*. However, according to the result provided in Fig. 39 at page 81, chromosomes leading to waviness might be not sequentially organized in the power spectrum.

4.1.1 Macro- and micro- categories of surface roughness

Following these observations, it is possible to categorize roughness in two contributions, according to the role of chromosomes in the $K(p)$ evolution. Considering a given observation length scale, the associated rough profile $Z(x)$ is split into two rough contributes

$$Z(x) = Z_L(x) + Z_S(x)$$

The profile $Z_L(x)$, namely the *macro-scale roughness*, is obtained summing up of chromosomes with a $K(p)$ evolution correlating up to 0.95 with one of the complete profile, i.e. $c_n > 0.95$.

The profile $Z_S(x)$, namely the *micro-scale roughness*, is associated to the remaining set of chromosomes, with $c_n \leq 0.95$.

From the operative stand point, in Alg. 2 all the steps performed to assess the macro-scale roughness are detailed. The $K(p)$ evolution of a rough profile $Z(x)$ is computed solving the frictionless normal elastic problem with $n_t = 20$ rigid body displacements in its peak-valley amplitude. This curve is taken as a reference, $y_r = K(p)$, see Step 1. Iteratively, the $y_n = K_n(p)$ evolution is computed for all the n_c chromosomes in the profile spectrum. Then, correlation coefficients c_n is calculated between y_r and y_n (Steps 2-5). Chromosomes with $c_n > 0.95$, i.e. leading to the macro-scale roughness, are retained in the final set U_c (Step 6). The remaining set asses the micro-scale roughness.

Algorithm 2 Macro-scale roughness assessment (i.e. profile waviness)

Input: surface genome, n_s, n_f and $n_t = 20$
Output: U_c: set of chromosomes leading to the macro-scale roughness

1: $y_r \leftarrow K(p)$ with BEM (n_t steps) for $Z(x) = \sum \mathcal{C}_n(x)$ with $n \in [n_s, n_f]$
2: **for all** $n = n_s : n_f$ **do**
3: $\quad y_n \leftarrow K_n(p)$ with BEM (n_t steps) for $\mathcal{C}_n(x)$
4: $\quad c_n \leftarrow$ corr. coeff.(y_r, y_n)
5: **end for**
6: $U_c \leftarrow \mathcal{C}_n(x)$ with $c_n > 0.95$

Following Alg. 2, the macro-scale composition is now assessed for $10\times$ realization of the genome in Tab. 1 that has been used in Chapter 3 to illustrate the multi-scale characterization of roughness.

The value of c_n for each chromosome is shown in Fig. 47, where also the correlation with respect to the $A(p)$ evolution is considered for the sake of explanation. The distinction between macro- and micro-scale roughness is determined using a correlation threshold greater than 0.95, introduced with a red dashed line.

Considering the $K(p)$ curve (black line with round marker), the correlation is higher for the chromosomes contributing to the longest wavelengths, i.e., chromosomes $n = 1$ to $n = 5$.

On the opposite, if the real contact area-pressure $A(p)$ relation is con-

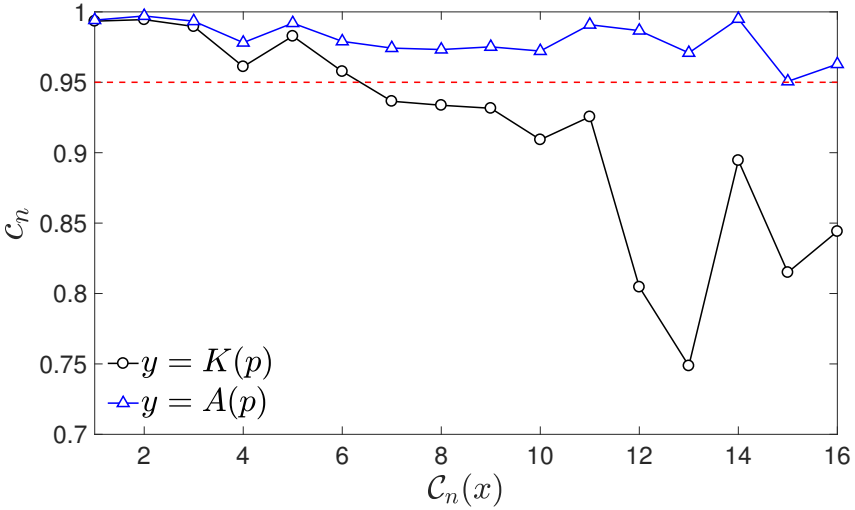

Figure 47: Correlation coefficient c_n between the mechanical evolution of a single chromosome $\mathcal{C}_n(x)$ with one of the complete realization of a surface, which genome is in Tab. 1. The red line represents the threshold value of 0.95 to identify the waviness of the rough profile.

sidered (blue line with triangle marker), both the longest and the shortest wavelengths have an influence on the evolution of the $A(p)$ evolution, and the correlation is always greater than 0.95.

The distinction made in Fig. 47 is now used to split roughness in the macro-scale contribution $Z_L(x)$ (red line) and the micro-scale one $Z_S(x)$ (blue line). Here, the concept of waviness is clear. In Fig. 48, the complete rough profile $Z(x)$ (black line) is shown and it is completely overlapped by the macro-roughness one $Z_S(x)$. The macro-scale roughness $Z_S(x)$ reproduces the "wavy" characterization of the rough profile and the micro-scale roughness $Z_S(x) = \sum_{n_s=7}^{16} \mathcal{C}_n(x)$ behaves more like a "noise" superimposed to the main signal, given by $Z_L(x) = \sum_{n_s=1}^{6} \mathcal{C}_n(x)$.

However, the role of $Z_L(x)$ is important for the $K(p)$ evolution and, then, the mechanical response of the macro- and micro- roughness are shown in Fig. 49. Regarding the $K(p)$ relation, the one provided by macro-scale roughness almost overlaps the one of the complete profile. The same observation can be done for the $A(p)$ evolution for small pressures. However, the two curves diverge for $p \gtrsim 1 \times 10^{-4}\,\mathrm{N/m}$.

To have a base-line understanding on the role of $\mathcal{H}$, the same realiza-

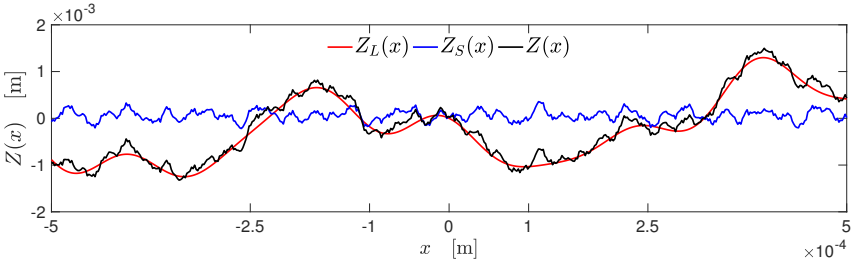

Figure 48: Topography of the rough profiles determining the multi-scale features of roughness of the in profile Tab. 1. It holds $Z(x) = Z_L(x) + Z_S(x)$.

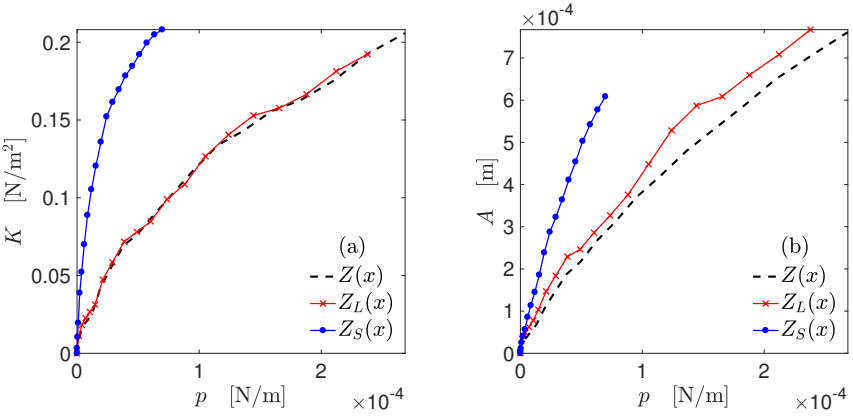

Figure 49: Mechanical evolution of the rough profile in Fig. 48 and of its macro- and micro- roughness.

tion is proposed by considering the same genome in Tab. 1 but imposing $\mathcal{H} = 0.85$. The same $\mathbf{\Phi}$ of the rough profile in Fig. 48 has been used. The waviness is also assessed by following Alg. 2.

The correlation coefficients c_n of each chromosome $\mathcal{C}_n(x)$ composing this new profile is reported in Fig. 50. In this case, more chromosomes are needed to reproduce its waviness, since chromosomes from $\mathcal{C}_1(x)$ to $\mathcal{C}_{10}(x)$ has a correlation coefficient greater than 0.95.

However, in this case not all the chromosomes contributes to the $A(p)$ evolutions as for the profile with $\mathcal{H} = 0.75$. Chromosomes $\mathcal{C}_{15}(x)$ has a value $c_{15} < 0.95$ and, even if its value is very close to this limit threshold, it does not contribute to the to the $A(p)$ evolution.

Fig. 51 shows the topographies of the macro- and micro scale roughness obtained with the results in Fig. 50. In this case, the height field is reduced in amplitude respect to the case with $\mathcal{H} = 0.75$, see Fig. 48. The macro-roughness profile $Z_L(x) = \sum_{n_s=1}^{10} \mathcal{C}_n(x)$ overlaps almost completely

the complete profile $Z(x)$. The micro-roughness $Z_S(x) = \sum_{n_s=11}^{16} \mathcal{C}_n(x)$ is also smoother, around one order of magnitude in difference.

This difference on profile amplitude, and on the related macro- micro roughness approximation, due by the fact that an increasing of $\mathcal{H}$ reduces in the chromosomes amplitude. In this case, this effect is more marked for chromosomes with shortest wavelength that longest ones.

However, the fact that values of $\mathcal{H}$ close to unity realize smoother profiles is true only if the same distribution of genes $\phi_{m,n}$ is adopted. A more detailed investigation on the coupled effect of $\mathcal{H}$ and the $\phi_{m,n}$ distributions is required to understand their interaction.

The reduction in amplitude observed Fig. 51 produces also a reduction of contact pressure range in the peak-valley amplitude of the profile. This is observable comparing Fig. 52 with Fig. 49.

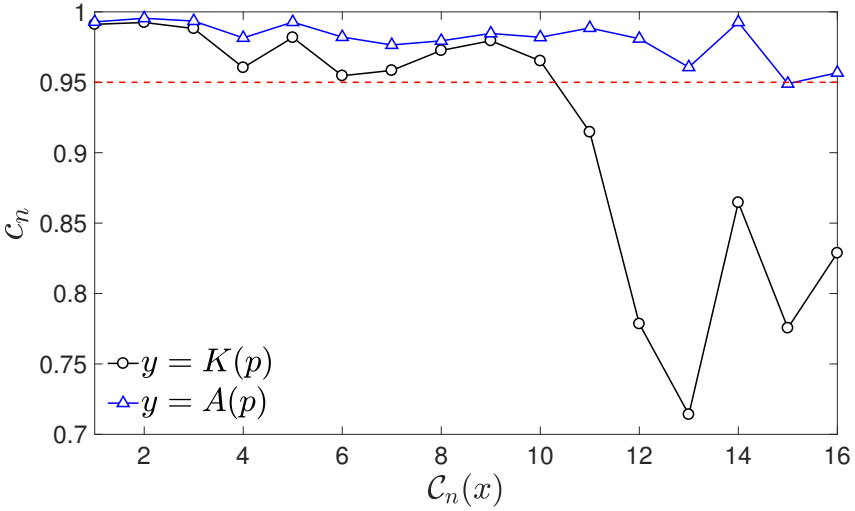

Figure 50: Correlation coefficient c_n between the mechanical evolution of a single chromosome $\mathcal{C}_n(x)$ with one of the complete realization of a surface, which genome is in Tab. 1, but with $\mathcal{H} = 0.85$. The red line represents the threshold value of 0.95 to identify the waviness of the rough profile.

The maximum pressure achieved with $\mathcal{H} = 0.85$ is the half of the one obtained with $\mathcal{H} = 0.75$. The $K(p)$ relation provided by macro-scale roughness almost overlaps the one of the complete profile. In this case, the $A(p)$ relations are more similar than the case with $\mathcal{H} = 0.75$, unless a small difference is observed.

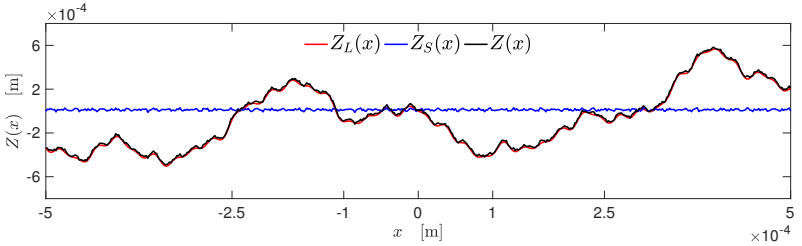

Figure 51: Topography of rough profiles determining the multi-scale features of roughness of the in profile Tab. 1, $\mathcal{H} = 0.85$.

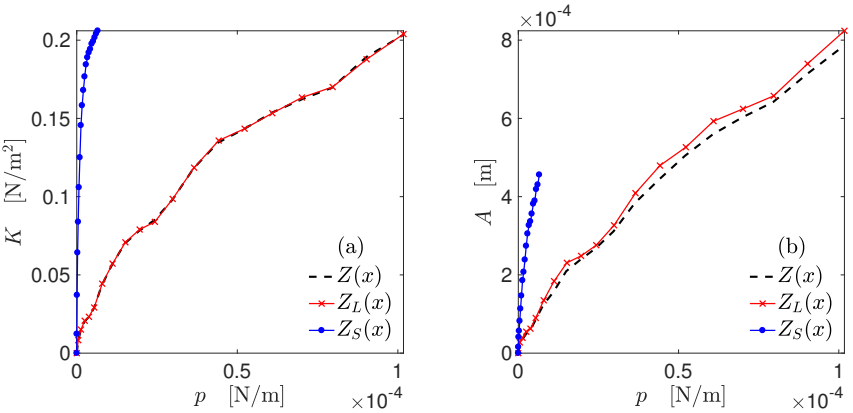

Figure 52: Mechanical evolution of the rough profile in Fig. 51 and of its macro- and micro- roughness.

4.1.2 Genetic mapping of surface roughness

In the previous subsection, the macro- and micro categories of roughness are defined to characterize the topography of rough profiles from a mechanical point of view. It has been observed that the composition of macro-roughness, i.e. waviness, of a profile is determined by the coupling of γ, $\mathcal{H}$ and the $\phi_{m,n}$ distribution. The coupling of different values of these genes leads to different type of chromosomes. Thus, to gain a wider understanding on the interaction of different length scales of roughness, waviness is assessed thanks to Alg. 2 for the profiles in a database of n_g genomes. This analysis will produce a *genetic map* of natural surfaces roughness by collecting genes thanks to the sequencing procedure presented in Sec. 3.3.

The genome database is herein numerically generated to highlight the coupled effect to empathize the coupling among γ, $\mathcal{H}$ and the $\phi_{m,n}$ distribution. Thus, for all profile the amplitude genes is fixed, $\mathcal{A} = 1$, and the main wavelength is set equal to $\lambda = 849.42\,\mu\mathrm{m}$.

Twenty different pairs of values $\mathcal{H}$ and γ are considered, generated according to a Sobol sequence (Niederreiter [1992]).

The phase matrix $\mathbf{\Phi}$ is composed by one column, since $\phi_{1,n}$ holds because of it is imposed $\mathcal{M} = 1$ for all genomes. This is a particular case of a chromosome (see Sec. 4.1), then it depicts a realistic realization of a rough profile reducing the computational costs. Three vectors $\mathbf{\Phi}$ of thirty elements are generated, with values from 0 to 2π, extracting sequentially the values from a Sobol sequence.

Finally, $n_g = 60$ genomes are generated combining the twenty pairs (γ, $\mathcal{H}$) with three vectors $\mathbf{\Phi}$.

The genomes so conceived are shown in Fig. 53. All pairs of genes (γ, $\mathcal{H}$) are shown in Fig. 53(a), with $\mathcal{H}$ ranging between 0.5 and 1.5, and γ between 1.2 and 2. The value of γ is chosen in such a way to keep small the number of frequencies composing the profile spectrum (see Eq. (3.5)), limiting the computational costs.

Furthermore, the first thirteen elements of the three vectors Φ are shown in Fig. 53(b). These phases refers to chromosomes which are in common to each realizations. A larger number of phases is considered for smaller values of γ (e.g.., for $\gamma < 1.6$), but they are not reported since they mostly contribute to the micro-scale roughness.

A this point, the n_g rough profiles $Z_i(x)$ are discretized in a length $L = \lambda = 849.42\,\mu\text{m}$ with $N = 512$ nodes, considering the chromosomes given by Eq. (3.5). The frictionless normal contact problem is therefore solved for each profile in the database via BEM, considering a Young Modulus equal to $E = 1\text{MPa}$ for all genomes.

The waviness is assessed with Alg. 2 for all these profiles, and result are summarized in the genetic map presented in Fig. 54. Each column corresponds to a rough profile, identified with the pairs (γ, $\mathcal{H}$) in Fig. 53(a) and the Φ distribution in Fig. 53(b). Each chromosome that identifies the macro-scale roughness is depicted by red squares. On the opposite, chromosomes determining the micro-scale roughness are depicted by blue squares.

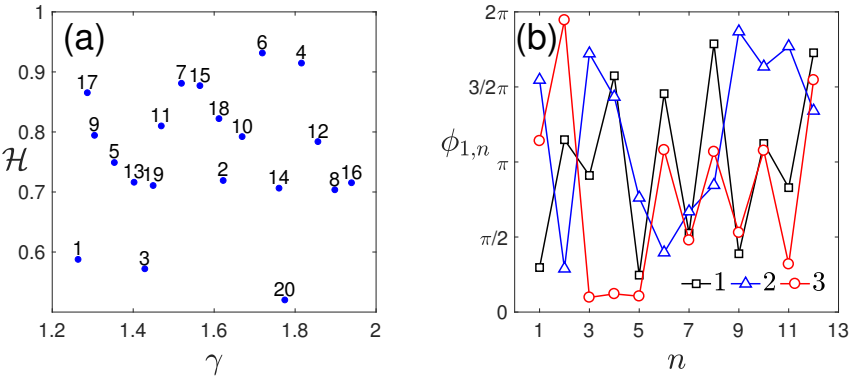

Figure 53: Genome database: (a) enumeration of all the pairs γ and $\mathcal{H}$ generated. (b) first thirteen elements of the three vectors Φ ($\mathcal{M} = 1$), which are common to each combination. A larger number of phases is considered for smaller values of γ (e.g.., for $\gamma < 1.6$).

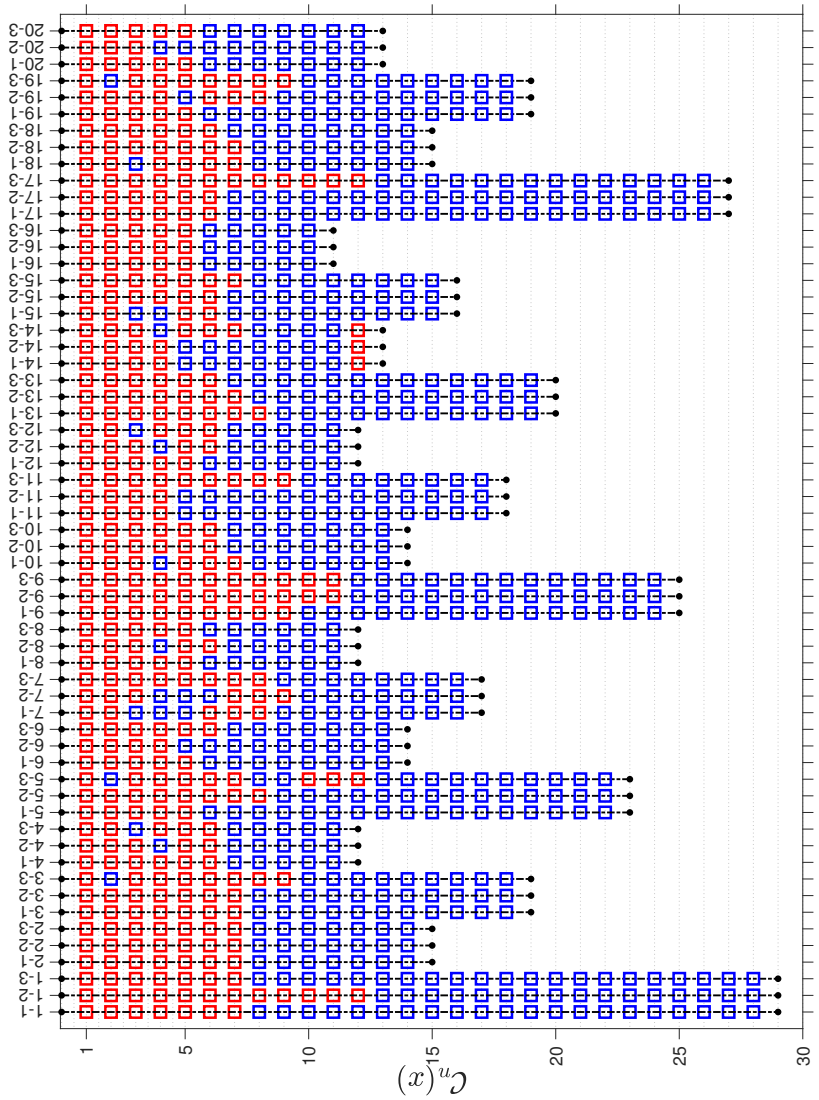

Figure 54: Genetic map showing the macro- (red) and micro-scale (blue) contribution of individual chromosomes to the profiles realized in a length $L = 849.42\,\mu\text{m}$, with genomes in Fig. 53.

A closer analysis of Fig. 54 shows that the waviness of a rough profile is not given exclusively by long-wave chromosomes, mainly when γ is high, see for example the genomes $14-1$, $14-2$ and $14-3$. For these profiles, the chromosome $\mathcal{C}_{12}(x)$ always contribute to the macro-roughness, even if in other genomes contribute to micro-roughness.

Moreover, considering the genomes $5-*$ and $7-*$, the phase matrix Φ adopted affects the waviness but in combination with the genes $(\gamma, \mathcal{H})$, even if the two pairs 5 and 7 are similar in value, see Fig. 53(a).

As last observation, the $\mathcal{C}_2(x)$ are leading to micro-waviness only if the rough profile is realized with the third set of ϕ.

The genetic map in Fig. 54 is summarized in Fig. 55. The first ten chromosomes are considered, moving their amount of contribution to macro- or micro-scale roughness. As n increase, the effect of a chromosome is dominant on the micro-scale roughness over the macro-scale one. However, an universal trend is not observable since their mechanical interaction is a high nonlinear problem and it is difficult to distinguish, a priori, between chromosomes influencing macro- or micro- scale roughness solely by their morphology.

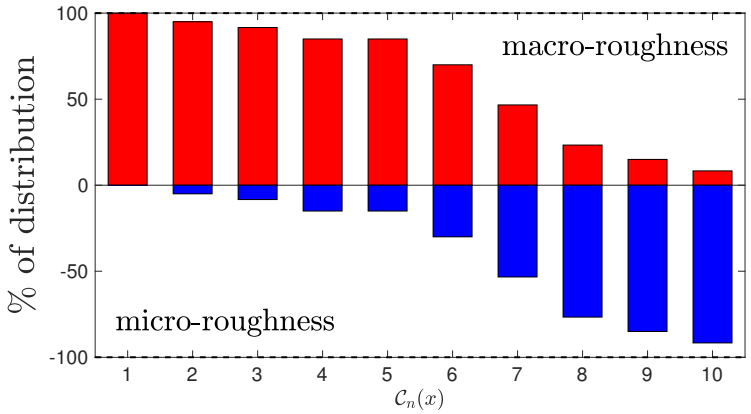

Figure 55: Distribution of macro- and micro- roughness contributions of the results in Fig. 54

4.2 Algorithms to design roughness with a target mechanical response

According to the observation done so far, it is possible to cross-over genomes to design a rough profile able to achieve a target mechanical response $y_t(\xi)$, where t stands for "target". This target evolution might depend on the specific needs of the problem and it can be, e.g., either the stiffness-load curve $K(p)$ or the contact area-displacement curve $A(\Delta)$. In the following, the variable ξ is considered as the contact pressure p, simplifying the notation with $y_t = y_t(p)$. Moreover, this target evolution is represented in a discrete set of n_t values of p and y_t . Thus, the frictionless elastic normal contact problem has to be solved in n_t equipoised far-field displacements Δ in the peak-valley amplitude of each profile.

In the following, three different algorithms to design the prototype profile are proposed and discussed. In the first algorithm, a genome is selected, from a known database of genomes, that realize a rough profile with the closest mechanical response to y_t. The related genes are then optimized in value to achieve more accurately the y_t imposed.

In the second algorithm, two genomes are selected from a known database of genomes. These genomes leads to two profiles that match the target response in two ranges Δp, imposed with a threshold value $\bar{p}$ of contact pressure. The value of $\bar{p}$ can be either imposed or by the problem or by the user. These genomes so selected are combined using an optimized cross-over mechanism.

Also in the third algorithm, two genomes are selected from a known database of genomes. Further, also in this case these two genomes leads to two profiles that match the target response in two ranges Δp, imposed with a threshold value $\bar{p}$ of contact pressure. However, in this case, chromosomes leading to the waviness are combined instead of the complete genomes, using an optimized cross-over mechanism.

Before discussing these three algorithms, the numerical set-up of the problem is addressed.

4.2.1 Numerical set-up of the problem

The first step is to identify a suitable function able to quantify how much the mechanical evolution y_i of the profile, realized at the observation scale chosen from the i-th genome, is similar to target one y_t. To do that, the similarity score

$$s_i = s(y_t, y_i) = 1 - \left|\left| \frac{y_t(\xi) - y_i(\xi)}{y_t(\xi)} \right|\right|_\infty \tag{4.1}$$

is defined, where $\|\cdot\|_\infty$ denotes the l_∞-norm. The i-th evolution coincides with the target one when $s_i = 1$ holds. Otherwise, it is similar to the target one when $s_i \simeq 1$ holds.

However, to compute consistently the similarity score in Eq. (4.1), the two evolutions has to insist in the same range of pressures, i.e. $p^i_{\max} = p^t_{\max}$. The maximum pressure level $p^t_{\max}$ is achieved by solving the contact problem with a far-field displacement equal to the target profile amplitude. The same consideration holds also for $p^i_{\max}$ of the i-th genome.

The condition $p^i_{\max} = p^t_{\max}$ can be achieved by varying the Young modulus E, see Eq. 2.4 for the BEM formulation presented in Sec. 2.2. However, the material is fixed from the problem and/or on the technologies chosen to realize the surface, such as 3D printing or additive manufacturing techniques (Excell [2013]; Taufik and Jain [2014]). Consequently also the value of E has to remain fixed in the physical and numerical formulation of the problem.

It is therefore possible to satisfy the condition $p^i_{\max} = p^t_{\max}$ rescaling the gene $\mathcal{A}_i$ of the i-th genome as

$$\mathcal{A}_i \leftarrow \frac{p^t_{\max}}{p^i_{\max}} \mathcal{A}_i \,, \tag{4.2}$$

because of the gap function $\boldsymbol{w}$ in the BEM formulation scales linearly with the height field, and so $\boldsymbol{p}$ (see Sec. 2.2). At the same time, the gene $\mathcal{A}_i$ could also be rescaled based on the maximum displacement level required, or based on any pressure/displacement value required.

Practically, the numerical steps performed to select the best genome from the database are described in Alg. 3. The similarity score in Eq. (4.1) is computed for all the n_g rough profiles obtained with genomes in the database, at the observation length L chosen, each of them rescaled with Eq. (4.2), see Step 2. The y_i evolution is computed via BEM, considering n_t different far-field displacements, from 0 to the new profile amplitude (Steps 3-5). Finally, $s_i = s(y_t, y_i)$ in Eq. (4.1) is computed (Step 6).

Algorithm 3 Similarity score extraction from a database of genomes

Input: target mechanical response y_t, database of n_g genomes (genes, p^i_{max}), observation length L
Output: $\boldsymbol{s} = s_i(y_t, y_i)$ with $i \in \{1, \dots, n_g\}$

1: **for all** $i = 1 : n_g$ **do**
2: $\quad \mathcal{A}_i \leftarrow$ Eq. (4.2)
3: $\quad$ **for all** $j = 1 : n_t$ **do**
4: $\quad\quad y_i^j \leftarrow$ BEM results at Δ_i^j
5: $\quad$ **end for**
6: $\quad s_i \leftarrow$ Eq. (4.1)
7: **end for**

4.2.2 Simple optimization of genes

The *Simple Optimization of Genes* (SOG) algorithm is now presented. Three genomes with the largest associated values of $s(y_t, y_i)$ are extracted from a database of genomes according to Alg. 3. At this point, the related genes are optimized using the Globally Convergent Method of Moving Asymptotes (GCMMA) algorithm (Svanberg [1987, 2002]). This is an iterative optimization algorithm, which is often used in optimal design for mechanical problems. For example, see Bacigalupo et al. [2016, 2017] for some of its recent applications to band gap optimization.

A MATLAB implementation of the GCMMA has been used, which technical details are given in Svanberg [2007]. The objective function has been chosen to be the square of the similarity score, i.e., $s^2(y_t, y_i)$, in order to increase its smoothness.

The GCMMA iterative solution is obtained after a number n_{it} of steps, starting from an initial choice for the vector of optimization variables. At each step, the partial derivative of the objective function is computed with respect to all the optimization genes, introducing a small perturbation $\epsilon > 0$ on the corresponding gene. Moreover, the gene $\mathcal{A}$ is scaled according to Eq. (4.2) every time the partial derivative is computed, to maintain the profile into the target pressure range.

Then, the number of genes considered in the optimization problem is reduced to save computational resources as time and allocating space. The genes $\mathcal{H}$, λ and γ determine the frequency spectrum, i.e., the interaction among different chromosomes. Therefore, they are not considered as genes to be optimized and their values is maintained fixed to their original one.

Consequently, only the phases $\phi_{m,n}$ can be considered as optimization variables. Their values are constrained in the range between $\mp 10\%$ of their initial one, to preserve the main features of the original chromosomes. Furthermore, according to what observed in Sec. 4.1.1, only the genes $\phi_{m,n}$ of chromosomes determining the profile waviness are considered. Such genes are selected according to Alg. 2.

Finally, the Simple Optimization of Genes (SOG) algorithm is summarized in Alg. 4, to get a comprehensive review of all its steps. Starting with a profile scouting from an available database (Step 1), the three profiles whose mechanical responses are most similar to the target y_t are chosen (Step 2).

The genes of each such genome are then optimized using the GCMMA algorithm (Steps 3-6), limiting the optimization variables only to the chromosomes determining the main features of the $K(p)$ evolution, as determined by Alg. 3. The resulting optimized genomes are denoted by $\hat{U}_1^i$.

Finally, among such genomes, the new genome is chosen as the one with the best (square of the) similarity score with respect to the target response (Step 7). In this last step, $\mathrm{argmax}(f_i)$ denotes the index i associated with the largest f_i.

Algorithm 4 *Simple Optimization of Genes* (SOG)

Input: target mechanical response y_t, genome database, realization length L
Output: new genome U_{SOG} with mechanical response close to y_t

1: $\boldsymbol{s}$ from Alg. 3
2: $U_1 \leftarrow 3$ genomes with the largest similarity score (Eq. (4.1))
3: **for all** $i = 1 : n_1$ **do** ($n_1 = card(U_1)$)
4: $\quad U_c^i \leftarrow$ Alg. 2 applied to U_1^i
5: $\quad f_i \leftarrow s(y_t, y_i)$, $\hat{U}_1^i$, both from GCMMA(U_c^i)
6: **end for**
7: $U_{SOG} \leftarrow \hat{U}_1^{\text{argmax}(f_i)}$

4.2.3 Genome cross-over

The Genome Cross-Over (GCO) algorithm mixes two genomes to obtain a new genome matching the target response y_t. These two genomes are chosen in relation to their similarity scores in two specific ranges of the target response y_t, ruled by $\bar{p}$, a threshold value of the contact pressure range. The value of $\bar{p}$ can be or fixed by the user ot imposed by the problem,in a case such a a sudden change in the target evolution.

In Fig. 56 it is explained how the two genome are selected. Here, a target response y_t is shown by the red line and also two evolutions y_1 (dashed black line) and y_2 (dashed dot blue line) are presented. These two evolutions are manually generated for the sake of explanation. They have a similarity score with respect to y_t equal to $s_1 \simeq 0.89$ and $s_2 \simeq 0.88$, respectively.

The curves y_1 and y_2 describe quite accurately the curve y_t in different ranges of pressures, if a threshold pressure $\bar{p}$ is defined. The value of $\bar{p}$ can be chosen arbitrarily, or might be imposed by the problem. In the specific case shown in the figure, in the interval $[0, \bar{p}]$, the curve y_1 represents with good accuracy y_t ($s_1(y_t, y_1) \simeq 0.97$). The same happens in the interval $[\bar{p}, p^t_{\max}]$ for the curve y_2 ($s_2(y_t, y_1) \simeq 0.99$).

It is reasonable to expect that a new profile obtained by combining the two genomes associated with y_1 and y_2, respectively, should provide a mechanical response closer to y_t over the whole range of pressures.

However, mixing these two genomes may also lead to a very different roughness organization. For this reason, the GCO iterative scheme checks if the new genome models a rough profile with a mechanical evolution similar y_t. As for the SOG, see Sec. 4.2.2, the GCMMA algorithm is used to increase the value of the similarity score.

The GCO structure is now presented in Alg. 5. The value of $\bar{p}$ is supposed to be known at priori, or fixed by the problem or by the user.

According to the value of $\bar{p}$, two different sets U_1 and U_2 are identified from the database of genomes (Steps 1-4).

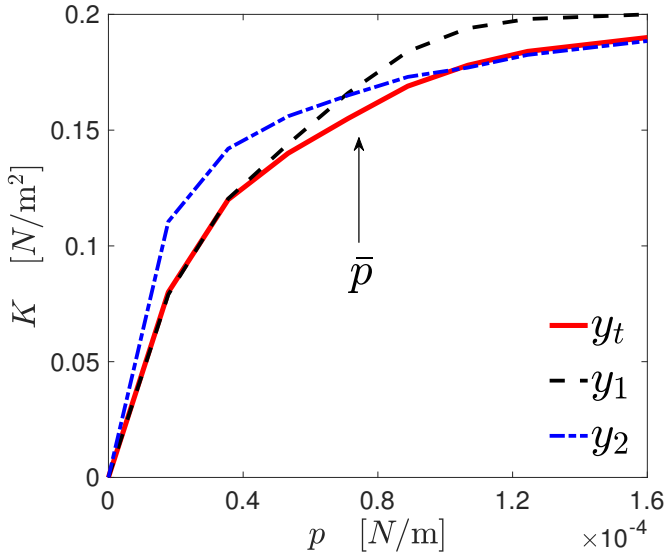

Figure 56: A generic profile y_1 approximates the target response y_t accurately under a certain level of pressure $\bar{p}$, and diverges after it. Another profile y_2 provides a good approximation of y_t only above $\bar{p}$.

The first set U_1 contains the genomes realizing rough profiles with a similarity score larger than 0.95 in the interval $[0, \bar{p}]$ (Steps 1 and 3).

The second set U_2 contains the genomes realizing rough profiles with a similarity score larger than 0.95 in the interval $[\bar{p}, p^t_{\max}]$ (Step 2 and 4).

All possible combinations of genomes from the two sets above are now considered, defining the set U_3 (Step 5-11). The value of the similarity score is computed with respect to the target response (Step 9).

The three new genomes showing the largest values of the similarity score are used as inputs to the GCMMA algorithm, defining the set U_4 (Step 12). Only genes $\phi_{m,n}$ giving the waviness of the two realization respectively are considered as optimization variables (see Alg. 2). The new genome U_{GCO} with the maximum value of the similarity is finally identified (Step 17).

Algorithm 5 *Genomes Cross-Over* (GCO)

Input: target y_t, threshold pressure $\bar{p}$, genome database, reference L
Output: new genome U_{GCO} with mechanical response close to y_t

---

1: $\boldsymbol{s}^{(1)}$ from Alg. 3, with similarity score computed in $[0, \bar{p}]$
2: $\boldsymbol{s}^{(2)}$ from Alg. 3, with similarity score computed in $[\bar{p}, p^t_{\max}]$
3: $U_1 \leftarrow$ genomes with $s_i^{(1)} > 0.95$
4: $U_2 \leftarrow$ genomes with $s_i^{(2)} > 0.95$
5: **for all** $i_1 = 1 : n_1$ **do** ($n_1 = card(U_1)$)
6: **for all** $i_2 = 1 : n_2$ **do** ($n_2 = card(U_2)$)
7: $U_3^{(i_1,i_2)} \leftarrow U_1^{i_1} + U_2^{i_2}$
8: $U_3^{(i_1,i_2)}$ rescaled according to Eq. (4.2)
9: $s(i_1, i_2) \leftarrow s(y_t, y_{(i_1,i_2)})$ from Eq. (4.1) applied to $U_3^{(i_1,i_2)}$
10: **end for**
11: **end for**
12: $U_4 \leftarrow$ the three genomes in U_3 with the largest s_i (from $\boldsymbol{s}$)
13: **for all** $i = 1 : n_4$ **do** ($n_4 = card(U_4)$)
14: $U_c^i \leftarrow$ Alg. 2 applied to U_4^i
15: $f_i \leftarrow s(y_t, y_i)$, $\hat{U}_4^i$, both from GCMMA(U_c^i)
16: **end for**
17: $U_{GCO} \leftarrow \hat{U}_4^{\text{argmax}(f_i)}$

4.2.4 Chromosomes cross-over

The Chromosomes Cross-Over (CCO) algorithm is now presented. In such an algorithm, only chromosomes determining the main features of the mechanical response of two different genomes are mixed to match the target response y_t. As done for the GCO, two genomes are selected that have the largest values of the similarity score in specific ranges of the target response y_t. The chromosomes of these two genomes are selected assessing their waviness with to Alg. 2.

The CCO iterative scheme is summarized in Alg. 6. According to the value of the threshold pressure $\bar{p}$, two different sets U_1 and U_2 of reduced genomes are identified, starting from the given database (Steps 1-4).

The set U_1 is obtained as follows. Genomes realizing rough profiles with a mechanical evolution similar ($s_i > 0.95$) in the interval $[0, \bar{p}]$ are selected, using Alg. 3. From each of these genomes, the chromosomes giving the waviness of the related realization are selected thanks to Alg. 2, obtaining the set U_1 (Steps 1 and 3). The second set U_2 is obtained in the same way as U_1, but computing the similarity score in the interval $[\bar{p}, p^t_{\max}]$ (Steps 2 an 4).

All possible combinations of these reduced genomes from the two sets U_1 and U_2 are now considered, defining the set U_3 (Steps 5-11). A new genome corresponds to each of these combinations. Its amplitude gene $\mathcal{A}$ is rescaled according to Eq. (4.2), to match the pressure requirement (Step 8). Then, the value of the similarity score is computed with respect to the target response (Step 9).

The three new genomes showing the largest values of the similarity score are used as inputs to the GCMMA algorithm, defining the set U_4 (Step 12). Only in the case of the CCO algorithm, all genes of this new genome are considered as optimization variables in the GCMMA algorithm, as the size of the optimization problem has been already reduced in Steps 3-4.

Finally, the new genome U_{CCO} with the maximum obtained value of the similarity score is identified (Step 16).

Algorithm 6 *Chromosomes Cross-Over* (CCO)

Input: target y_t, threshold pressure $\bar{p}$, genome database, reference L
Output: new genome U_{CCO} with mechanical response close to y_t

$\boldsymbol{s}^{(1)}$ from Alg. 3, with s_i computed in the interval $[0, \bar{p}]$
$\boldsymbol{s}^{(2)}$ from Alg. 3, with s_i computed in the interval $[\bar{p}, p^t_{\max}]$
$U_1 \leftarrow \mathcal{C}_n(x)$ from Alg. 2, for those genomes with $s_i^{(1)} > 0.95$
$U_2 \leftarrow \mathcal{C}_n(x)$ from Alg. 2, for those genomes with $s_i^{(2)} > 0.95$
for all $i_1 = 1 : n_1$ **do** ($n_1 = card(U_1)$)
    for all $i_2 = 1 : n_2$ **do** ($n_2 = card(U_2)$)
        $U_3^{(i_1,i_2)} \leftarrow U_1^{i_1} + U_2^{i_2}$
        $U_3^{(i_1,i_2)}$ rescaled according to Eq. (4.2)
        $s(i_1, i_2) \leftarrow s(y_t, y_{(i_1,i_2)})$ from Eq. (4.1) applied to $U_3^{(i_1,i_2)}$
    end for
end for
$U_4 \leftarrow$ the three genomes in U_3 with the largest s_i (from $\boldsymbol{s}$)
for all $i = 1 : n_4$ **do** ($n_4 = card(U_4)$)
    $f_i \leftarrow s(y_t, y_i)$, $\hat{U}_4^i$, both from GCMMA(U_4^i)
end for
$U_{CCO} \leftarrow \hat{U}_4^{\text{argmax}(f_i)}$

4.3 New genomes to achieve a single target mechanical response

Algorithms described in Sec. 4.2 are herein discussed with to two representative examples. To initialize these algorithms, the same database of n_g genomes of Fig. 53 is used. The rough profiles $Z_i(x)$ are realized in a length $L = 849.42\,\mu\text{m}$ μm with $N = 512$ nodes. However, a natural database could be more suitable to this kind of procedure, since genes would have values more adapt to the natural application fields.

The mechanical evolutions of all the profiles $Z_i(x)$ are visualized in Fig. 57. Also, two targets $y_t^1 = K_1(p)$ (black line) and $y_t^2 = K_2(p)$ (red line) are shown in Fig. 57(a). This targets will be used to compare the SOG, GCO and CCO algorithms.

The target evolution y_t^1 has a trend similar to the ones belonging to the database. The second target y_t^2 is more particular.

In such target y_t^2, the $K(p)$ relation grows linearly with the contact pressure for $p \leq 0.53 \times 10^{-4}\,\mathrm{N/m}$. Then after this limit, it has a fixed value. Then, in such a case the threshold value in the problem is fixed, i.e. $\bar{p} = 0.53 \times 10^{-4}\,\mathrm{N/m}$.

This kind of target y_t^2 could be an optimal evolution required in applications where the interface electrical conductivity should remain constant for high pressures, as, e.g., for a micro-conductor.

The comparison proceeds as follows. Firstly, the discussion on the target y_t^1 is proposed, comparing the new-genomes obtained from the methods herein presented. The choice of $\bar{p}$ is also discussed for both GCO and CCO algorithms. The spectral features and the topographies of these best profiles are investigated.

At the end, the genomes leading to profiles achieving target y_t^2 will be discussed. In such a case, the choice of $\bar{p}$ is given by the problem.

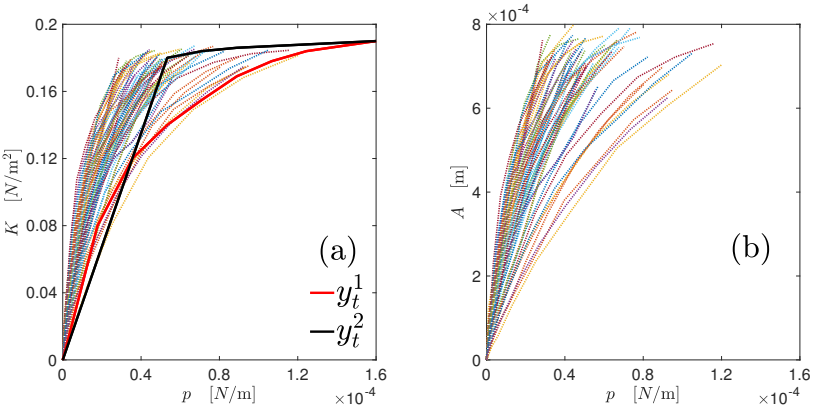

Figure 57: Mechanical evolution of the profiles ($L = 849.42\,\mu\mathrm{m}$) with the genomes in Fig. 53. (a) shows $K(p)$ evolutions. The target y_t^1 is depicted by red line. The target y_t^2 is shown by black line. (b) shows the $A(p)$ evolutions.

4.3.1 Single target: a first example

The results of the algorithms presented in Sec. 4.2 is now discussed, considering as target the function y_t^1. The threshold pressure used for both the GCO and CCO is set equal to $\bar{p} = 0.8 \times 10^{-4}\,\mathrm{N/m}$.

The values of the similarity score s obtained using the SOG (black dashed line), GCO (red line) and CCO (blue dashed-dot line) algorithms are reported in Fig. 58.

For each algorithm, the three best final solutions are reported and they are represented in the figure by a triangle, circle and cross, in decreasing value of similarity score.

The comparison in Fig. 58 is done reporting the similarity score (of these solutions) at three different steps of each algorithm, distinguished by the application of the GCMMA optimization method.

The first step, denoted by "GCMMA 0", corresponds to the first stage of each algorithm, before the application of the GCMMA. For the SOG, this first step corresponds to the three best values obtained from the scouting of the database (Step 2 in Alg. 4). For both the GCO and the CCO algorithms, it corresponds to the computation of the similarity score after cross-over (Step 12 in both Alg. 5 and Alg. 6).

The second step, denoted by "GCMMA 1", correspond to the application of the GCMMA at the genome obtained at "GCMMA 0". This step coincides con the output of SOG, GCO and CCO respectively. For the SOG, the GCMMA algorithm is applied with $n_{it} = 5$ iterations. For the GCO and CCO is imposed $n_{it} = 3$. In both cases, the number of iteration used for the GCMMA algorithm is fixed to have similar simulation times, since the number of optimization parameters are different in the various problems.

A third step is introduced, denoted by "GCMMA 2". At this step, the GCMMA algorithm is applied again for the SOG and GCO algorithms, to optimize the genes belonging only to micro-scale roughness. Then, the GCMMA is applied with $n_{it} = 1$ iterations only to those chromosomes that have a major contribution on to the micro-scale roughness, which

were not considered "GCMMA 1". The GCMMA is not applied again for the CCO which does not take into account the micro-roughness contribution. Then, a fictitious step "GCMMA 2" is introduced, whose value of the similarity score coincides with "GCMMA 1".

All the algorithms are quite efficient in matching the target mechanical response y_t, achieving large values for the similarity score. The application of the GCMMA after "GCMMA 0" is generally beneficial for the algorithms, even if in some cases any improvement of the result is observed, see for example GCO (2) and CCO (1).

The application of the GCMMA to the micro-roughness is beneficial only for genomes obtained with the GCO. For the solution given by the SOG, any improvement of the similarity score is observed. However, the GCO and CCO algorithms might provide even better solutions by varying the value of the threshold pressure $\bar{p}$.

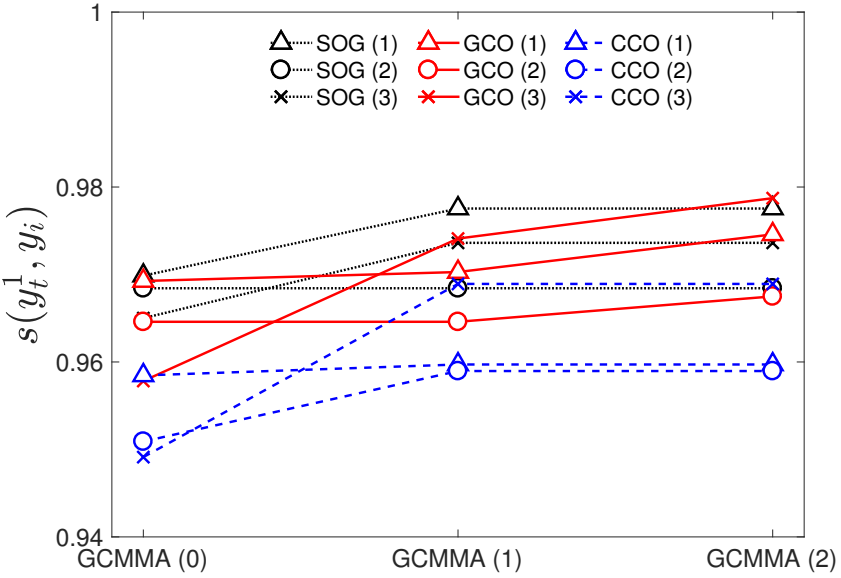

Figure 58: For the outputs of the SOG, GCO and CCO algorithms, values of the similarity scores with respect to the target y_t^1. For both the GCO and CCO, the threshold pressure is imposed equal to $\bar{p} = 0.8 \times 10^{-4}\,\mathrm{N/m}$.

Effect of the threshold pressure $\bar{p}$

The effect of the threshold pressure $\bar{p}$ is now considered for the GCO and the CCO algorithms. To assess the sensitivity of them with respect to such a parameter, additional simulations have been made.

Both the GCO and CCO algorithms have been applied ranging $\bar{p}$ between $0.5 \times 10^{-4}\,\mathrm{N/m}$ and $1.1 \times 10^{-4}\,\mathrm{N/m}$. The maximum value of the similarity score obtained for each value of $\bar{p}$ is shown in Fig. 59(a). For the GCO, a variation of about 1% of the similarity score is observed.

On the contrary, the CCO is not affected by the value of $\bar{p}$. Moreover, the new genomes obtained by the CCO algorithm are composed of the same starting genomes, independently of the threshold pressure $\bar{p}$. This may be due to the fact that our investigation has been conducted starting from a small database of genomes.

In Fig. 59(b), the cardinality of the set U_3 is presented, for both the GCO and CCO algorithms. This set contains the new genomes obtained after the crossing-over, before the application of the GCMMA. The white part indicates, for both algorithms, the number of new genomes with a similarity score with respect to the target curve y_t^1 is larger than 0.95. The cardinality of the set U_3 varies significantly with $\bar{p}$ for both algorithms.

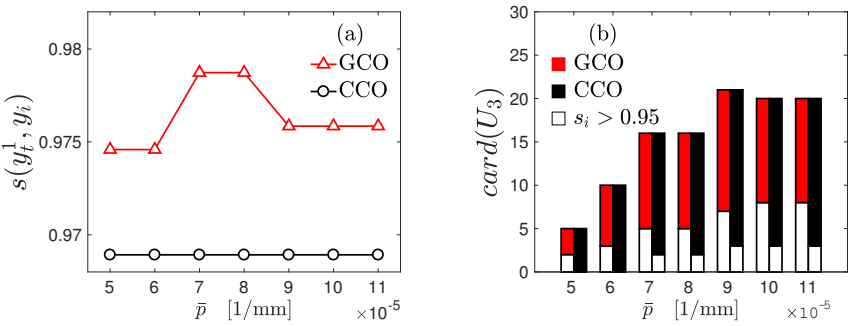

Figure 59: Sensitivity for the GCO and CCO respect to $\bar{p}$ (a) Best similarity scores obtained for each algorithm (b) Cardinality of the set U_3 obtained at the end of Step 11 of each algorithm ("Step 1" in Fig. 58).

Description of the optimized genomes representing y_t^1

The spectral features of the profiles with the best similarity score are now considered. For both the GCO and CCO algorithms, these solution are obtained with a threshold pressure equal to $\bar{p} = 0.8 \times 10^{-4}\,\mathrm{N/m}$, see Fig. 59. Thus, these three profiles have the higher value of similarity score among the ones presented in Fig. 58. The higher similarity score is obtained with GCO (3) solution, of about 0.98. The SOG (1) similarity score is a bit smaller of that. The smaller value is obtained with GCO (3) solution, of about 0.97.

These three profiles have mechanical responses overlapping significantly with the target curve, see Fig. 60(a). However, the three genomes present different $A(p)$ evolutions, as shown in Fig. 60(b). Only the $A(p)$ curves obtained by the SOG and GCO are similar. This may be due to the fact that, in the case of the CCO, high-frequency features of the rough profile have been neglected.

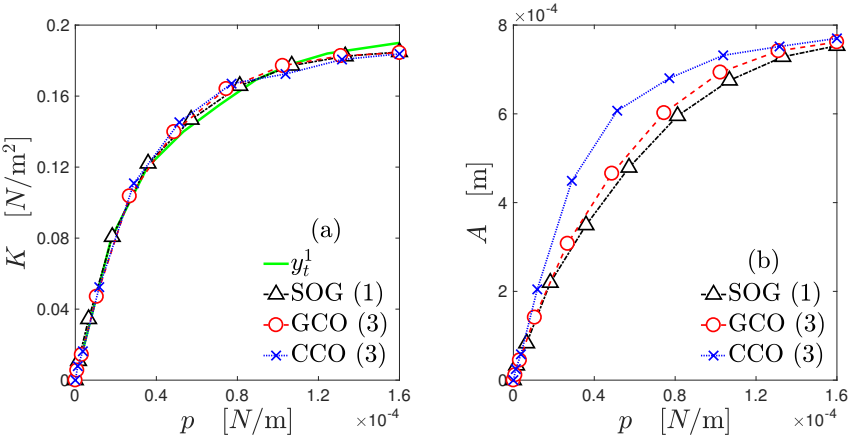

Figure 60: Mechanical evolutions of the best rough profiles, obtained from each algorithm presented in this dissertation to achieve the target curve y_t^1. For the topography of these profiles see Fig. 61.

The topography of these rough profiles is presented in Fig. 61. The profiles obtained by the SOG, GCO and CCO algorithms are depicted, respectively, through a black dash dot-line, a red dashed line, and a blue continuous line. All these profiles have very similar geometrical features, regarding the locations of peaks and valleys. Moreover, it is interesting to notice that the profile provided by the CCO algorithm is a good approximation of the profile given by the GCO algorithm, which presents more high-frequency features.

To conclude, the discrete power spectral density $P(\omega)$ of the new obtained genomes is shown in Fig. 62, and it is represented by markers in all sub-figures. The continuous PSD function obtained through the FFT filtering (Berry and Lewis [1980]; Wu [2001]) is shown by a continuous line. The FFT is computed according the procedure detailed in Borri and Paggi [2015].

For the SOG, see Fig. 62(a), the peaks of the continuous PSD function match the discrete one accurately for high frequencies. No good matching is found for low frequencies, since any peak is present. This error given by the FFT filtering was firstly observed when the feature of multi-scale roughness have been discussed in Chapter 3, Sec. 3.2. For high frequencies, the discrete spectrum overlaps the peaks obtained from the FFT filtering.

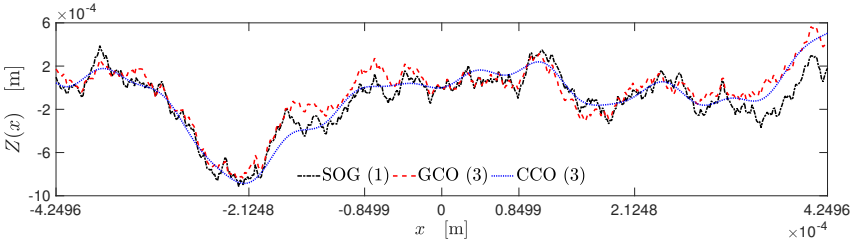

Figure 61: Topography of the best rough profiles approximating the target curve y_t^1, see Fig. 60.

A similar trend is found for the genome obtained in the case of the GCO, see Fig. 62(b). Here, the spectrum is more dense and, only for high frequencies, peaks of the continuous PSD function are located in the same positions of the chromosomes wavelengths. In this case, a consistent difference in $P(\omega)$ amplitude is observed.

Finally, the spectrum of the profile obtained by the CCO, that is composed of a small set of frequencies, is shown in Fig. 62(c). In this case, the discrete power spectral density is nearly proportional to the one of the SOG in the low-frequency range. The high-frequency part of the PSD is flat, and some peaks are found in correspondence of chromosomes.

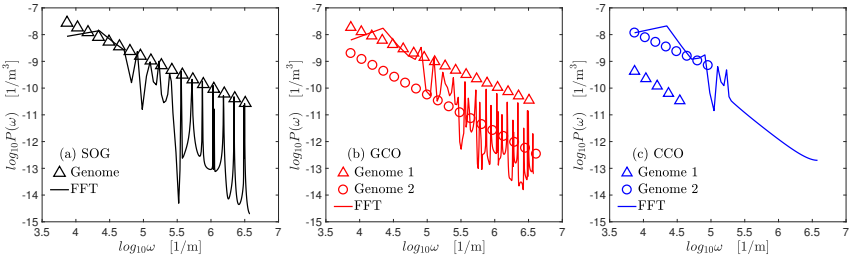

Figure 62: Logarithmic (base 10) evolution of the power spectral densities of the obtained new genomes, whose associated profiles are shown in Fig. 61.

4.3.2 Single target: a second example

Results obtained from the SOG, GCO and CCO algorithms are now discussed, using as target the function $y_t^2 = K(p)$, see Fig. 57. The threshold pressure fixed by the problem and it is equal to $\bar{p} = 0.53 \times 10^{-4}\,\mathrm{N/m}$.

The evolution y_t^2 is optimal in application that has to maintain constant the electrical conductivity of a joint. For example, a micro-conductor that have to assure a fixed energy transmission in a specific range of clamping pressure. Also, in sealing application, an electric sensor monitor if a certain clamping pressure level, $\bar{p}$, is assured. If the clamping pressure goes below this critical limit $\bar{p}$, the conductivity rapidly decreases.

The similarity scores $s_i = (y_t^2, y_i)$ for the different methods are visualized in Fig. 63, maintaining the same notation of Fig. 58. The solution with the best similarity index is given by the SOG algorithm, with an increase of at least 3% in the end. Also the GCO and the CCO show an increase of the similarity score at least 3% in the end. The GCO and SOG methods looks more appropriate for this kind of problems.

Moreover, all the methods benefit on the application of the GCMMA to the macro-roughness. Regarding the application of the GCMMA to the micro-roughness, both the SOG and the GCO benefit on this step. However, also in this case (see Fig. 58), one solution of the SOG does not increase the similarity score by applying the GCMMA to the micro-roughness.

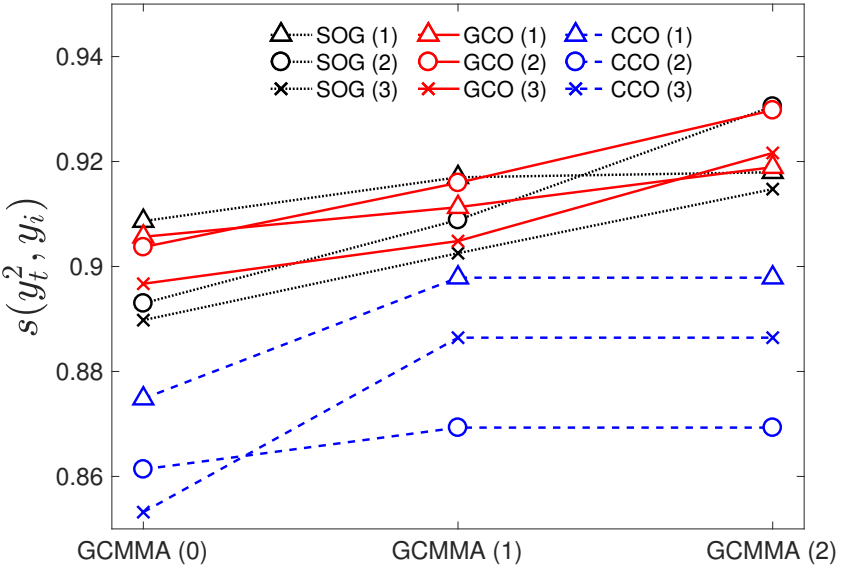

Figure 63: For the outputs of the SOG, GCO and CCO algorithms, values of the similarity scores with respect to the target y_t^2. The threshold pressure is $\bar{p} = 0.53 \times 10^{-4}\,\mathrm{N/m}$ for both the GCO and CCO, fixed by the problem.

The mechanical evolutions of the best rough profiles are shown in Fig. 64. All the solutions are not able to approximate the flat behavior of y_t^2 for $p > 0.53 \times 10^{-4}\,\mathrm{N/m}$. However, the solution given by the CCO is more suitable to represent this asymptotic behavior, showing a more flat trend in this range. Is also interesting to notice how the $A(p)$ evolution for the profile given by the CCO algorithm has a very similar trend to its $K(p)$ evolution.

The topographies associated to this new genomes are shown in Fig. 65. Also in this case, those profile have a lot of common characteristics, for example the location of valleys and peaks. However, the profile given by the CCO is very smooth respect to the other two, while it is able to give a very good approximation of y_t^2.

Finally, the logarithmic expressions of the spectral features related to the profiles in Fig. 65 is shown in Fig. 64. For the SOG (see Fig. 65(a)), the frequencies obtained thanks to the FFT filtering are overlapped by each chromosome, even if a difference in magnitude is found.

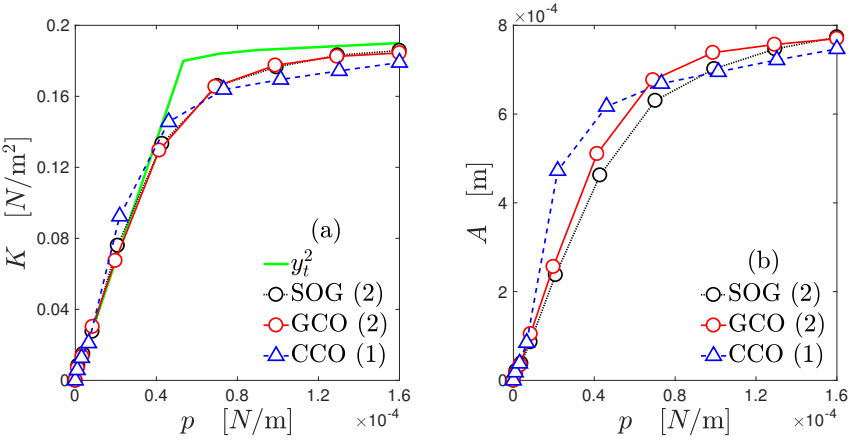

Figure 64: Mechanical evolutions of the best rough profiles, obtained from each algorithm presented in this dissertation to achieve the target curve y_t^2.

Moreover, also in this case studied, no good matching is found for low frequencies, since any peak is present.

For the GCO, see Fig. 65(b), the FFT filtering overestimates in amplitude the discrete spectrum. The spectrum is dense and, only for high frequencies, peaks of the continuous PSD function are almost located in the same positions of the chromosomes wavelengths.

Finally, the spectrum of the profile obtained by the CCO is shown in Fig. 65(b), and it composed of seven frequencies. The PSD obtained with the FTT technique is completely flat. However, the $P(\omega)$ amplitude is matched, for low frequency, by Genome 2.

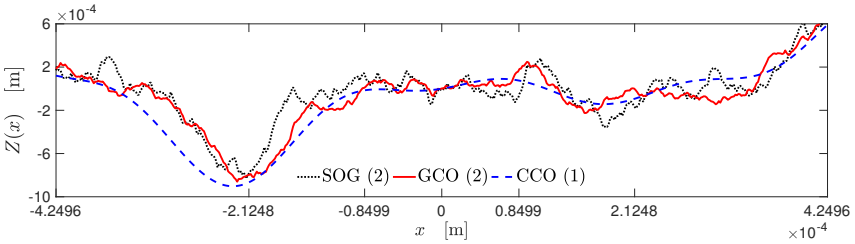

Figure 65: Topography of the best rough profiles approximating the target curve y_t^2, see Fig. 64.

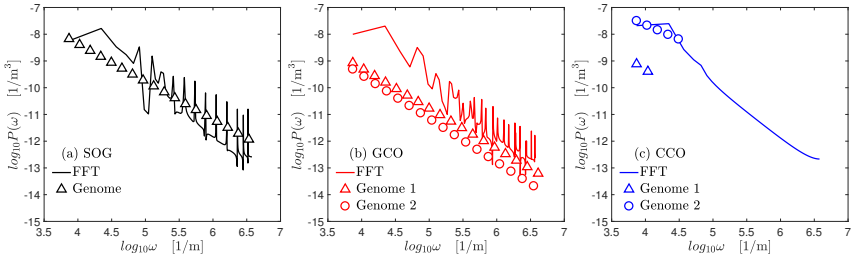

Figure 66: Logarithmic (base 10) evolution of the power spectral densities of the obtained new genomes, whose associated profiles are shown in Fig. 65.

4.4 Algorithms to design roughness with a multi-target mechanical responses

In this last section, a combined problem is proposed. The new-genome has design roughness in a realization length $L = 849.42\,\mu\text{m}$ such that it achieve two targets respect two different evolutions. For instance, the first target could be the normal contact stiffness, $y_t^1 = K(p)$, while the second could be the real contact area, $y_t^3 = A(p)$. These two target y_t^1 and y_t^3 are presented in Fig. 67. The same target y_t^1 discussed in Sec. 4.3.1 is used for the $K(p)$ evolution, see Fig. 57.

The results presented for y_t^1 in Sec. 4.3.1 shows that the similarity score given by the CCO algorithm is a bit smaller than the SOG and the GCO, see Fig. 58. However, even if the related $K(p)$ evolutions are close to y_t^1, the related $A(p)$ evolutions are different, see Fig. 60 and Fig. 64. The CCO approximation of y_t^1 is obtained with only chromosomes leading to macro-roughness. However, the GCO algorithm design roughness with a closer evolution to the target one, since micro-roughness is considered.

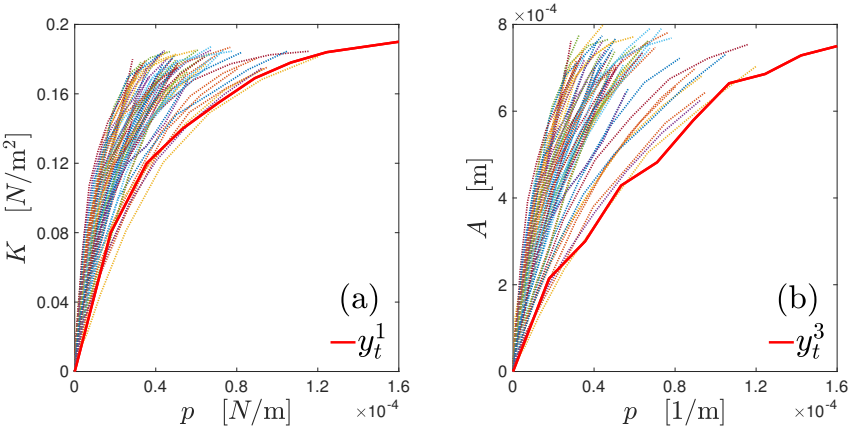

Figure 67: Mechanical evolution of the profiles ($L = 849.42\,\mu\text{m}$) with the genomes in Fig. 53. (a) shows $K(p)$ evolutions. The target y_t^1 is depicted by red line. (b) shows $A(p)$ evolutions. The target y_t^3 is depicted by red line.

4.4.1 Mixed chromosomes cross over

According to these observations, a particular variation of the CCO algorithm is therefore proposed for the coupled problem with two target y_t^1 and y_t^3. In this algorithm, chromosomes leading to macro-roughness (to achieve the $K(p)$ target) are mixed to chromosome leading to micro-roughness (to achieve the $A(p)$ target). This algorithm can be extended to all combination of chromosome possible, each of them leading to the target evolution to be achieved.

The main steps of this algorithm, namely the *Mixed Chromosomes Cross-Over* (M-CCO), are presented in Alg. 7. The similarity score in Eq. (4.1) is computed separately between the y_t^1 and y_t^3 targets and all the realization obtained from the database in the reference length L imposed, obtaining vectors $\boldsymbol{s^{(1)}}$ and $\boldsymbol{s^{(2)}}$ (Step 1-2).

Then, the waviness is firstly assessed with Alg.2 to genomes with a similarity score greater than $s_i^{(1)} > 0.95$, computed thanks to Alg. 2. The related sets of chromosomes leading to macro-roughness are stored in set U_1 (Step 3).

For genomes with a similarity score greater than $s_i^{(2)} > 0.95$, computed thanks to Alg. 2, chromosomes leading to micro-roughness are stored in set U_2 (Step 4).

The resulting sets U_1 and U_2 contain the information about different chromosomes. All possible new genomes among all the combinations between sets U_1 and U_2 are stored in set U_3 (Step 7). The rough profile so obtained in the reference length chosen is rescaled to satisfy the maximum pressure, Eq. (4.2). The contact mechanics problem is solved via BEM for the resulting profile, computing the $K^{(i_1,i_2)}(p)$ and $A^{(i_1,i_2)}(p)$ evolutions (Steps 8).

Two similarity scores are now computed, $s_{(i_1,i_2)}^{(1)}$ and $s_{(i_1,i_2)}^{(2)}$ of the evolutions $K^{(i_1,i_2)}(p)$ and $A^{(i_1,i_2)}(p)$ with the corresponding target response y_t^1 and y_t^3. A mixed similarity score is computed by multiplying these similarity scores, i.e. $s_{(i_1,i_2)}^{(3)} \leftarrow s_{(i_1,i_2)}^{(1)} \times s_{(i_1,i_2)}^{(2)}$ (Steps 9-11).

Now, these three genomes with larger mixed similarity score are stored in set U_3 (Step 14). The GCMMA optimization method is applied before to the part of the genome leading to macro-roughness (Step 16). Then, considering the so updated version of the genome, it is applied to the part of the genome leading to micro-roughness (Step 17). The objective function chosen is the multiplication between the two relative similarities, i.e. $f_i = s_i(y_t^1, K(p)) \times s_i(y_t^3, A(p))$.

Finally, the new genome U_{MIX} with the maximum obtained value of the similarity score is finally identified (Step 16).

Algorithm 7 *Mixed Chromosomes Cross-Over* (M-CCO)

Input: targets y_t^1, y_t^3, genome database, target y_t, threshold $\bar{p}$, genome database, reference length L
Output: new genome U_{MIX} with evolutions close to y_t^1 and y_{t3}^3

1: $\boldsymbol{s^{(1)}}$ from Alg. 3 with y_t^1
2: $\boldsymbol{s^{(2)}}$ from Alg. 3 with y_t^3
3: $U_1 \leftarrow \mathcal{C}_n(x)$ from Alg. 2, for those genomes with $s_i^{(1)} > 0.95$ with y_t^1
4: $U_2 \leftarrow \mathcal{C}_n(x)$ from Alg. 2, for those genomes with $s_i^{(2)} > 0.95$ with y_t^2
5: **for all** $i_1 = 1 : n_1$ **do** ($n_1 = card(U_1)$)
6: **for all** $i_2 = 1 : n_2$ **do** ($n_2 = card(U_2)$)
7: $U_3^{(i_1,i_2)} \leftarrow U_1(i_1)$ +$U_2(i_2)$
8: $K^{(i_1,i_2)}(p)$, $A^{(i_1,i_2)}(p)$ for $U_3^{(i_1,i_2)}$ rescaled with Eq. (4.2)
9: $s_{(i_1,i_2)}^{(1)} \leftarrow$ Eq. (4.1) of $K^{(i_1,i_2)}(p)$ with y_t^1
10: $s_{(i_1,i_2)}^{(1)} \leftarrow$ Eq. (4.1) of $A^{(i_1,i_2)}(p)$ with y_t^3
11: $s_{(i_1,i_2)}^{(3)} \leftarrow s_{(i_1,i_2)}^{(1)} \times s_{(i_1,i_2)}^{(2)}$
12: **end for**
13: **end for**
14: $U_4 \leftarrow$ the three genomes in U_3 with the largest s_i (from $\boldsymbol{s^{(3)}}$)
15: **for all** $i = 1 : n_4$ **do** ($n_4 = card(U_4)$)
16: $f_i \leftarrow s_i(y_t^1, K(p)) \times s_i(y_t^3, A(p))$ GCMMA on macro-roughness
17: $f_i \leftarrow s_i(y_t^3, K(p)) \times s_i(y_t^3, A(p))$ GCMMA on micro-roughness
18: **end for**
19: $U_{MIX} \leftarrow \hat{U}_4^{\text{argmax}(f_i)}$

4.4.2 New genome to match a multi-target mechanical response

The three best genomes leading to the profiles obtained with the M-CCO algorithm are presented in Tab. 4. In this table are reported, for each solution obtained, the objective function score, f_i, and the relative similarity score with the two targets. Also, the starting genomes used as macro- and micro- roughness, see Fig. 53. The first index refers to the pair $(\gamma, \mathcal{H})$, the second to the vector of phases used $\boldsymbol{\phi_{1,n}}$. The assessment of macro- roughness is reported into the genetic map in Fig. 54.

genome	f_i	$s_i(y_t^1, K^i(p))$	$s_i(y_t^3, A^i(p))$	macro-	micro-
y_1	0.863	0.955	0.903	5-1	2-2
y_2	0.838	0.952	0.88	11-1	2-2
y_3	0.811	0.943	0.86	5-1	2-1

Table 4: Resulting genomes of M-CCO algorithm in terms of similarity score, f_i, and the relative similarity score with the two targets. Also, the genomes used for the macro- and micro- roughness are used.

The best approximation of the contact response is given by the genome y_1, shown by a blue curve with round marker in Fig. 68. Looking at the $A(p)$ evolution in Fig. 68(b), all of these three solution diverges consistently the y_t^3 in the range of contact pressure between $p > 0.2 \times 10^{-4}\,\mathrm{N/m}$ and $p \leq 0.9 \times 10^{-4}\,\mathrm{N/m}$.

As far as the $K(p)$ evolution is concerned in Fig. 68(a), the y_1 and y_3 evolutions shown overlapping trend to the target y_1^1. The second solution y_2 is the only with a different genome leading to macro-roughness and its trend is not close to y_t^1 in the range of $p > 0.2 \times 10^{-4}\,\mathrm{N/m}$ and $p \leq 0.8 \times 10^{-4}\,\mathrm{N/m}$.

The y_1 evolution almost overlaps y_3 for $p \gtrsim 1 \times 10^{-4}\,\mathrm{N/m}$. These two profiles hare composed by the same starting set of chromosomes leading to macro-roughness. They also presents a very close evolution of the $A(p)$ one, see Fig. 68(a), that is also close to the target one. Both trend diverges for $p \gtrsim 1.2 \times 10^{-4}\,\mathrm{N/m}$.

For both y_1 and y_3 evolution, the starting micro-roughness is composed by the same pair $(\gamma, \mathcal{H})$, but with different vector of phases. These observations highlight again the dominant role of macro-roughness in the frictionless elastic contact response.

The three rough profiles are visualized in Fig. 69, emphasizing the role of macro-, Fig. 69(a), and micro-, Fig. 69(b), roughness. Each rough profile in Fig. 69(c) is obtained by summing up these components, with the same color and line type.

In Fig. 69(a) the macro-roughness of each solution is presented. The dashed blue and the dash-dotted red profiles, y_1 and y_3 genomes respectively, have a similar macro-roughness topography, with small differences. See, for example, the different topography in the range $x \gtrsim 0.4 \times 10^{-4}\,\mathrm{N/m}$ and $x \lesssim 2.125 \times 10^{-4}\,\mathrm{N/m}$

The related micro-roughness of genomes y_1 and y_3 in Fig. 69(b) have and overlapping topography, as they are composed by the same starting pair (γ,$\mathcal{H}$) and vector of phases $\boldsymbol{\phi_{1,n}}$.

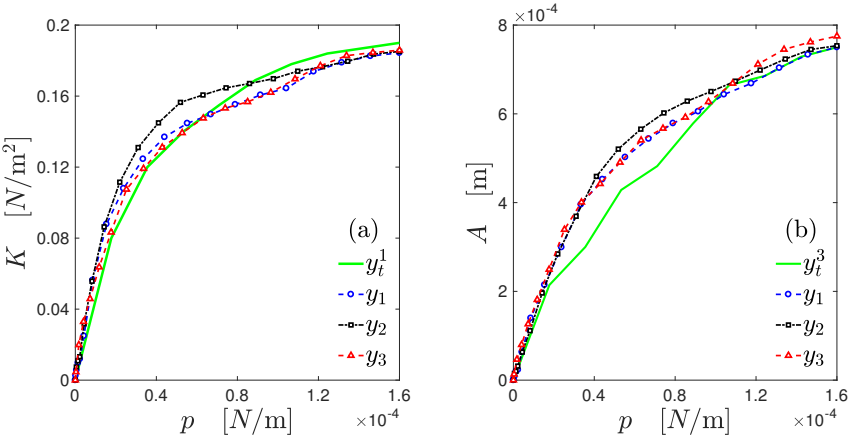

Figure 68: Mechanical evolutions of the best rough profiles, obtained from the M-CCO algorithm presented in this dissertation to achieve two target evolutions y_t^1 and y_t^2. For the topography of these profiles see Fig. 69.

The resulting topographies of genomes y_1 and y_3 in Fig. 69(c) are similar. They have also a close mechanical response, see Fig. 68.

The topographies related to y_2 are different to the ones of y_1 and y_3, as the macro-roughness component is different.

Finally, the spectral composition of these new genome is shown Fig. 70. The difference in amplitude is given by the different value of $\mathcal{A}$ applying Eq. (4.2) to respect the threshold pressure.

All the FFT filtering methods shows a PSD of the complete profile with a lot of peaks. In all of these cases, the first part of the PSD so obtained does not present any evident peak. For the solution y_2 these are close to the discrete spectrum of the genome, see the squares in the central part of the spectrum in Fig. 70(b).

Moreover, these squares in Fig. 70(b), representing the micro-roughness, are six and the peaks observed from the FFT filtering are five.

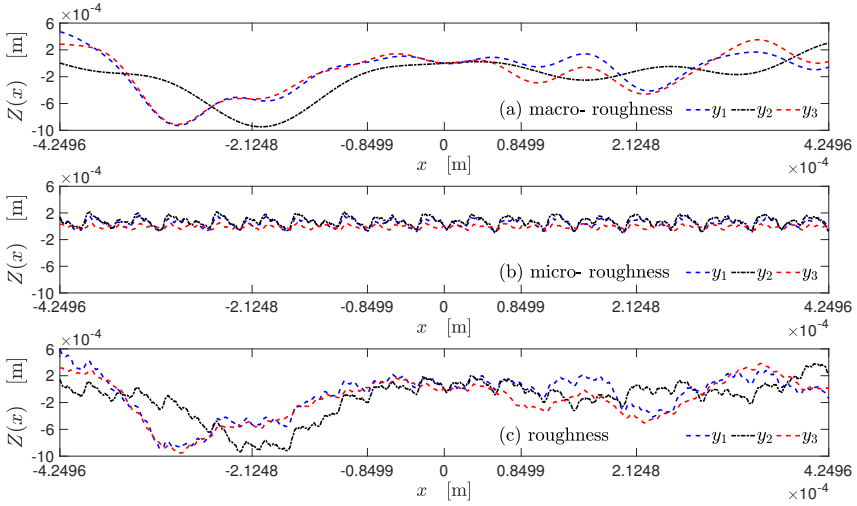

Figure 69: Results of the M-CCO algorithm with y_t^1 and y_t^3 targets. (a) shows the macro-roughness (b) shows the micro-roughness (c) shows the complete profile.

Looking at the solutions y_1 and y_3, who showed a similar mechanical response and topography, they presents also a close PSD in the low frequencies part. The high frequency regions are different, because it it composed by different genomes.

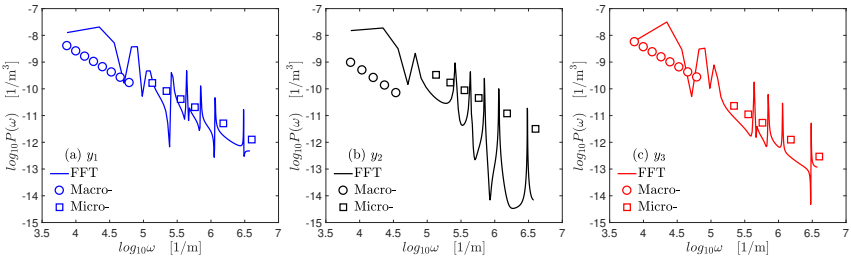

Figure 70: Logarithmic (base 10) evolution of the power spectral densities of the obtained new genomes, whose associated profiles are shown in Fig. 69.

It is possible to conclude that a particular class of genomes can be identified to be combined with other genomes to match both the $K(p)$ and $A(p)$ targets. The M-CCO algorithm has to be improved, mainly in the selection of the chromosomes to be combined.

Chromosomes leading to macro-roughness are therefore fundamental for this kind of problem. The contact area morphology is determined by the short wavelengths composing the PSD, as confirmed by many authors and discussed in Chapter 1. However, the coupling between macro- and micro-scale roughness is also crucial in the determination of the $A(p)$ curve, see e.g. Paggi and Ciavarella [2010] where the $A(p)$ curve is discussed for small compenetrations.

Chapter 5

Conclusion and future developments

In this last Chapter, the methods presented in this dissertation are summarized. Then, the implication on the current technology of this research is discussed, considering also possible the future developments.

5.1 Summary and future developments

In Chapter 2 the problem of fractal surfaces modeling and the frictionless normal contact between rough surfaces has been addressed. Particular attention has been given to the thin film approximation of fluids in small channels. This approximation, that can be exploited at different level of accuracy, is very useful to model th fluid-structure interaction in contact mechanics. At the end, an algorithm have been proposed to identify the percolating and non percolating networks of the free volume generated by rough surfaces in contact.

The morphological features characterizing the evolution of the real contact area over compenetration are the same that control the percolating characteristics of rough surfaces in contact. Furthermore, the network of channels is strongly affected by the surface resolution, but its

percolating characteristic does not depend on the variation of the distribution of slopes for the whole range of fractal dimension herein investigated. Particularly, the level of compenetration affect the percolating and non-percolating properties of the free volume, but its effect it is mitigated when a surface has a fractal dimension $D > 2.5$. At the contrary, it is quite pronounced for $D < 2.5$.

Another significant effect of the fractal dimension D is on the r.m.s. of slope m_2, which affect in its turn the normal contact stiffness K Paggi and Ciavarella [2010]; Dapp and Muser [2015]; Yastrebov et al. [2015]. This leads to a different distribution of contact pressures, which leads to a different formation of constriction or saddle points Bottiglione et al. [2009b]; Dapp et al. [2012]; Dapp and Muser [2015].

This observation is consistent with a fluid-dynamics model of permeability, that predicts a reduction of the pressure-loss for a generic fluid in a wider channel, if the Reynolds number of the system is less than 20 Darcy [1857]; Yu and Cheng [2002]. The Reynolds number defines the resistance of this network, according to the problem size, as investigated by Dapp Dapp and Muser [2015].

The algorithm proposed in the present dissertation does not predict the network permeability and the pressure loss, since it primarily focuses on the network description. Future development will have to focus on the determination of the critical section size and the length of the parent channel.

In Chapter 3, a sequencing algorithm has been proposed to identify the co-sinusoids, that characterize the surface roughness genome. According to the MWM function herein used as a base model, surface roughness has been reconstructed according to a top-down and bottom-up approach, via the definition of chromosomes.

The mechanical of chromosomes interaction has been investigated via BEM for the elastic frictionless normal contact problem, showing that the TD approach is more suitable to reconstruct a profile, that has $K(p)$ and $A(p)$ relations closer to the real one. Therefore, some dominant chromosomes have been identified in the contact problem.

The main result observed for the TD approach is that the waviness of the profile is dominant not only for the $K(p)$ evolution (Paggi and Barber [2011]), but also for $A(p)$. However, for $A(p)$ evolution, all the chromosomes in the frequency spectrum may play an important role.

The extension to the 3D case is fundamental, since in this case more analysis and simulation are needed to understand the effective role of chromosomes in the mechanical response. The know-how herein discussed is fundamental to reconstruct prototype surfaces, whose characteristics have to satisfy specific mechanical requirement.

The key point of this dissertation was to provide a methodology to obtain new surface topologies with target contact responses based on the specific application at hand, and it has been discussed in Chapter 4. First of all, the problem of the interaction among different length scales composing the surface roughness has been investigated. Roughness have been categorized in two contributions that realize a surface at a given observation length L. This is done according to Paggi and Barber [2011] about the essential role of waviness for the $K(p)$ relation.

Thus, the macro-scale roughness has been defined as the set of chromosomes determining the $K(p)$ relation, i.e. the profile waviness. The set of remaining chromosomes composes the micro-scale roughness. To assets the profile waviness, the correlation coefficient c_n between the mechanical $K(p)$ evolution of the chromosomes with the one of the complete profile. The sum of al chromosomes with $c_n > 0.95$ determined the profile waviness.

Thanks to these results, three methods have been proposed to achieve a target mechanical response. The first method optimizes the value of genes of a known genome, it is a Simple optimization of Genome (SOG). The second and third methods consist in a crossing-over of genomes (GCO) or chromosomes (CCO), selected by dividing the target curve in references intervals.

Methods based on crossing-over led to profiles that almost fully reproduce the $K(p)$ curve. Moreover, the CCO algorithm approximates the target response in a good way with a small number of chromosomes.

The CCO algorithm is more suitable for particular mechanical and engineering request, such us in-line control of morphology. This in-line control can be achieved by using deformable stripes, for example with an electrical impulse, of length equal to the wavelength of the chromosome chosen to be controlled.

A modified version of the CCO algorithm is finally proposed to design roughness achieving two targets respect to two different mechanical evolutions. This algorithm, namely the mixed chromosome cross-over (M-CCO), mixes the macro-roughness and the micro-roughness of two different genomes. A representative example is shown, which highlight that some details of the methodologies herein proposed has to be improved to achieve completely these two targets. Furthermore, a much wider set of surface topographies is planned to be explored, increasing the pace to discovery of optimal patterns and textures based on the need.

5.2 Implications in current research and technology

Surface genomics aims at providing universal description of multi-scale roughness, to accelerate the discovery of innovative surfaces. In this ambitious context, this work is a first attempt to perform a genetic characterization of rough surfaces. The multi-scale characterization of roughness permits to isolate the elementary co-sinusoidal waves which characterize its fundamental features. By combining these waves, it is possible to replicate any kind of mechanical response by generating an *ad-hoc* surface topographies for the frictionless normal contact problem.

A partial answer to fundamental questions regarding the interaction of different length scales of roughness has been attended in this dissertation, but only in few representative cases. Such known solutions are used as benchmark for the proposed methodology to assess the feasibility of the idea and validate predictions. For instance, it is known from linear elastic contact mechanics of rough surfaces that thermal/electric contact conductance are mostly influenced by waviness, rather than by roughness on finer scales Paggi and Barber [2011].

This is herein confirmed thanks to the multi-scale roughness description proposed. Furthermore, our approach is able to determine the waviness of the profile and to define the separation of length scale efficiently by mechanical considerations. It is important to notice that, in certain cases, wavelengths who theoretically compose the macro-scale roughness are in fact influencing also the micro-scale roughness.

The contact area morphology is ruled by the interaction of both the macro-scale and the micro-scale roughness. The overall frequency spectrum determines the load-area relation, without a specific impact of the spectral moments related to the PSD. This might confirm the efficiency of the Persson's theory of contact, although it opens the question related to correct resolution with which the contact area morphology has to be observed and investigated.

It is clear that adding features to the power spectrum modifies the morphology of the contact area and the parent network of channels determining the fluid leakage between rough surfaces. For instance, for a given imposed far-field displacement Δ, the probability to have closed paths or zones where the fluid is trapped vanishes by increasing the number of points approximating the rough surface, as observed in the lacunarity behavior of the real contact area in fractal models. The influence of the resolution suggests that studies relating the area morphology with the percolating properties of the parent network have to be done carefully, also for the determination of the percolation threshold. Thus, the importance of resolution chosen is not simply crucial, it is fundamental to properly interpreter the relation between the applied pressure and the contact area morphology.

Persson's theory might be used to determine the proper resolution to investigate the morphology changes over contact. For example, it might be imposed that the proper resolution is the one where the critical constriction appears. This fact does not mean that fluid leakage occurs, as it might also depends on the physical and dynamical characterization of the fluid.

The thermal/electric contact conductance is given by the profile waviness, that is treated separately from the micro- scale roughness in the problem. This problem was firstly addressed by Barber thanks to the bounds theorem Barber [2003]. Then, the role of the lower cut-off of the PSD has then investigated by Paggi and Barber [2011], showing that the thermal/electric contact conductance is not affected by the short wavelengths. A similar result has been found by Popov et al. [2013] for random self-affine surfaces, who supposed a division in tow sides of the PSD to define contact stiffness (longest waves) and friction (shortest waves). He obtained these results neglecting the central part of a continuum PSD although here a the longest waves of a discrete spectrum are considered.

Here, the parameters that identifies the waviness of the profile are isolated and empathized, showing that the simple division proposed by Popov et al. [2013] might be done but it is not universal. Here, it is shown that not only long waves determine the contact stiffness of a rough profile and, vice-versa, short waves do not determines completely the contact area behavior. Moreover, the mechanical separation of length-scales herein proposed is applicable in all contest and for all material.

Another significant step forward with respect to the state-of-the-art regards the numerical methods to predict emergent tribological properties. Future work will concern the introduction of the non-linear interactions between rough surface in contact, such as friction, adhesion, wear and so on. Those mechanical interactions are difficult to be predicted with BEM formulation. Indeed, it is necessary to move from BEM to FEM, to tackle nonlinear multi-field coupled contact and fracture problems with complex and realistic geometries.

Further application of surface genomics will open the possibility to generate infinite combinations of roughness, without any pre-model assumption. The repetition of sequencing for a wide range of natural or artificial surfaces available in nature and technology (at least 100) will constitute a wide database of surface genomes.

After this work, any surface resulting from the superposition of a random selection of such genome components can be realized and characterized. Clearly, this opens the path to generate infinite combinations with different roughness features, instead of focusing on specific model geometries. Moreover, this revolutionary methodology is able to identify emergent responses and recursive patterns, and finally produce demonstrators by the new technologies of this era of Industry 4.0, such as 3D printing prototyping or additive manufacturing technologies.

Finally, the topic of surface morphing, to modify roughness in time based on external stimuli for additive manufacturing such as 3D printing, will be addressed by acting on the deformation of a sub-surface material micro structure. Morphing is a novel concept that had applications to smart structures and devices, while its application to surfaces is a very new research area.

As far as rapid prototyping is concerned, to produce innovative surfaces based on the model results, 3D printing is the most fascinating and reliable existing technology, for its very fast progress and impact on several industrial sectors, to maximize technology transfer and patent applications. Dimensional analysis considerations will be invoked to assure physical similitude of the scaled prototypes, see Paggi and Barber [2011].

The new interdisciplinary framework proposed in this dissertation integrates tribology, contact, numerical methods, control theory and rapid prototyping techniques. Thus, it is clear that there are many man-years of future science with connected publications to develop the suggested methodologies further. This methodology presents presents therefore a significant complexity proper of a high risk/high gain frontier research project and it is opening a wide time.

References

Almqvist, A., Fabricius, J., Larsson, R., and Wall, P. (2014). A new approach for studying cavitation in lubrication. *Proceedings of Royal Society London*, 136(011706):1–6.

Almqvist, N. (1996). Fractal analysis of scanning probe microscopy images. *Surface Science*, 355:221–228.

Almuramady, N. and Borodich, F. (2017). Hierarchical models of engineering rough surfaces and bio-inspired adhesives. *Proceedings of the 25th UKACM Conference on Computational Mechanics*, 12:13.

Anciaux, G. and Molinari, J. (2009). Contact mechanics at the nanoscale, a 3D multiscale approach. *International Journal for Numerical Methods in Engineering*, 79:1041–1067.

Anvir, D., Biham, O., Lidar, D., and Malcai, O. (1998). Is the geometry of nature fractal? *Science*, 279:39–40.

Archard, J. (1957). Elastic deformation and the laws of friction. *Proceeding of Royal Society*, A243:190–205.

Ausloos, M. and Berman, D. (1985). A Multivariate Weierstrass-Mandelbrot Function. *Proceedings of Royal Society London*, A(400):331–350.

Bacigalupo, A., Gnecco, G., Lepidi, M., and Gambarotta, L. (2017). Optimal design of low-frequency band gaps in anti-tetrachiral lattice meta-materials. *Composites Part B: Engineering*, 12:341–359.

Bacigalupo, A., Lepidi, M., Gnecco, G., and Gambarotta, L. (2016). Optimal design of auxetic hexachiral metamaterials with local resonators. *Smart Materials and Structures*, 25:054009 (19).

Bandis, S., Lumsden, A., and Barton, N. (1981). Experimental studies of scale effects on the shear behaviour of rock joints. *International Journal of Rock Mechanics and Mining Sciences & Geomechanics Abstracts*, 18:1–21.

Barber, C., Dobkin, D., and Huhdanpaa, H. (1996). The Quickhull Algorithm for Convex Hulls. *ACM Transactions on Mathematical Software*, 22(4):469–483.

Barber, J. (2003). Bounds on the electrical resistance between contacting elastic rough bodies. *Proceedings of Royal Society London*, A(459):53–66.

Barber, J. (2010). *Elasticity*. Springer, Dordrecht, 3rd Edition.

Bemporad, A. and Paggi, M. (2015). Optimization algorithms for the solution of the frictionless normal contact between rough surfaces. *International Journal of Solids and Structures*, 06:69–70.

Berry, M. and Lewis, Z. (1980). On the Weierstrass-Mandelbrot fractal function. *Proceedings of Royal Society London*, A 370:459–484.

Bhushan, B. (2009). Biomimetics: lessons from nature – an overview. *Philosophical transaction of the Royal Society*, 367:1445–1486.

Bora, C., Flater, E., Street, M., Redmond, J., Starr, M., Carpick, R., and Plesha, M. (2005). Optimal design of low-frequency band gaps in anti-tetrachiral lattice meta-materials. *Tribology letters*, 19(1):37–48.

Borodich, F. (1997). Some fractal models of fracture. *Journal of the Mechanics and Physics of Solids*, 45(2):239–259.

Borodich, F. and Mosolov, A. (1992). Fractal roughness in contact problems. *Journal of Applied Mathematics and Mechanics*, 56(5):681–690.

Borodich, F. and Onishchenko, D. (1999). Similarity and fractality in the modelling of roughness by a multilevel profile with hierarchical structure. *International Journal of Solids and Structures*, 36(17):2585–2612.

Borodich, F., Pepeyshev, A., and Savencu, O. (2016). Statistical approaches to description of rough engineering surfaces at nano- and micro- scales. *Tribology international*, 103:197–207.

Borodich, F. and Savencu, O. (2016). Hierarchical models of engineering rough surfaces and bio-inspired adhesives. In Heepe, L., Xue, L., and Gorb, S., editors, *Bio-inspired Structured Adhesives: Biological Prototypes, Fabrication, Tribological Properties, Contact Mechanics, and Novel Concepts*, volume 9 of *Biologically-Inspired Systems*, pages 179–219. Springer, Cham, Switzerland.

Borri, C., Gagliardi, M., and Paggi, M. (2017). Evolution of fatigue damage in flexible photo-voltaic module. *Photovoltaic technical conference - From advanced materials and processes to innovative applications*, Marsiglia.

Borri, C. and Paggi, M. (2015). Topological characterization of anti-reflective and hydrophobic rough surfaces: are random process theory and fractal modeling applicable? *Journal of Physics D: Applied Physics*, 48:045301.

Borri, C. and Paggi, M. (2016). Topology simulation and contact mechanics of bifractal rough surfaces. *Proceedings of the Institution of Mechanical Engineers, Part J: Journal of Engineering Tribology*, page 045301 (12pp).

Borri-Brunetto, M., Carpinteri, A., and Chiaia, B. (1999). Scaling phenomena due to fractal contact in concrete and rock fractures. *Computer Methods in Applied Mechanics and Engineering*, 95:221–238.

Borri-Brunetto, M., Chiaia, B., and Ciavarella, M. (2001). Incipient sliding of rough surfaces in contact: a multiscale numerical analysis. *Computer Methods in Applied Mechanics and Engineering*, 190:6053–6073.

Bottiglione, F., Carbone, G., Mangialardi, L., and Mantriota, G. (2009a). Leakage mechanism in flat seals. *Journal of Applied Physics*, 106(104902).

Bottiglione, F., Carbone, G., and Mantriota, G. (2009b). Fluid leakage in seals: An approach based on percolation theory. *Tribology international*, 42:731–737.

Brettel, M., Friederichsen, F., Keller, M., and Rosenberg, M. (2014). How Virtualization, Decentralization and Network Building Change the Manufacturing Landscape: An Industry 4.0 Perspective. *World Academy of Science, Engineering and Technology*, 8(1):37–44.

Bush, A., Gibson, R., and Thomas, T. (1975). The elastic contact of a rough surface. *Tribology international*, 35(1):87–11.

Campana, C. and Muser, M. (2006). Pratical Greenś function approach to the simulation of elastic semi-infinite solids. *Physic review B*, 74:075420.

Carollo, V., Reinoso, J., and Paggi, M. (2017). A 3d finite strain model for intralayer and interlayer crack simulation coupling the phase field approach and cohesive zone model. *Composite Structures*, 182:636–651.

Ciavarella, M. and Demelio, G. (2006). A "re-vitalized" Greenwood and Williamson model of elastic contact between fractal surfaces. *Journal of Mechanics and Physics of Solids*, 54:2569–2591.

Ciavarella, M., Demelio, G., Barber, J., and Jang, Y. (2000). Linear elastic contact of the Weierstrass profile. *Proceedings of Royal Society London*, 456:387–405.

Ciavarella, M., Greenwood, J., and Barber, J. (2017). Effect of Tabor parameter on hysteresis losses during adhesive contact. *Journal of the Mechanics and Physics of Solids*, 98:236–244.

Ciavarella, M., Greenwood, J., and Paggi, M. (2008). Inclusion of "interaction" in the Greenwood and Williamoson contact theory. *Wear*, 265:729–734.

Ciavarella, M., Murolo, G., Demelio, G., and Barber, J. (2004). Elastic contact stifness and contact resistance for the Weierstrass profile. *Journal of Mechanics and Physics of Solids*, 52:1247–1265.

Cinat, P. and Paggi, M. (2015). Simulation of fluid flow across rough surfaces in contact. *Conference Proceedings of the YIC GACM 2015*, 1:59–63.

Colebrook, F. (1939). Turbulent flow in pipes, with particular reference to the transition region between the smooth and rough pipe. *J. Inst. Civ. Eng. London*, 27(11):133–156.

Dapp, W., Lucke, A., Persson, B., and Muser, M. (2012). Self-affine elastic contacts: Percolation and leakage. *Physical Review Letter*, 108:244301.

Dapp, W. and Muser, M. (2015). Contact mechanics of and Reynolds flow through saddle points: On the coalescence of contact patches and the leakage rate through near-critical constrictions. *Euro Physics Letters (EPL)*, 109:4001.

Darcy, H. P. G. (1857). Recherches Experimentales relatives au mouvement de l'eau dans les Tuyaux. *Mallet-Bachelier, Paris*.

Excell, J. (2013). The rise of additive manufacturing. *The Engineer*, Retrivied:517–527.

Fillon, M., Wodtke, M., and Wasilczuk, M. (2015). Effect of presence of lifting pocket on the THD performance of a large tilting-pad thrust bearing. *Friction*, 3(4):266–274.

Gagliardi, M., Lenarda, P., and Paggi, M. (2017). A reaction-diffusion formulation to simulate EVA polymer degradation in environmental and accelerated ageing conditions. *Solar Energy Materials and Solar Cells*, 164:93–106.

Greenwood, J. (2006). A simplified elliptic model of rough surface contact. *Proceedings of the Institution of Mechanical Engineers*, 261:191–200.

Greenwood, J., Putignano, C., and Ciavarella, M. (2011). A Greenwood & Williamson theory for line contact. *Wear*, 270:332–334.

Greenwood, J. and Tripp, J. (1970). Contact of two nominally flat surfaces. *Proceedings of the Institution of Mechanical Engineers*, 1855:625–633.

Greenwood, J. and Williamson, J. (1966). Contact of two nominally flat surfaces. *Proceedings of the Royal Society of London*, 295 A:300–319.

Greenwood, J. and Wu, J. (2001). Surface Roughness and Contact: An Apology. *Meccanica*, 36:617–630.

Hamrock, B., Schmid, S., and Jacobson, B. (2004). *Fundamentals of Fluid Film Lubrication*. Marcel Dekker, New York, 2rd Edition.

Hartl, D. and Jones, E. (2002). *Genetics: analysis of genes and genomes*. 6th ed, Jones & Bartlett.

Johnson, K. (2003). *Contact mechanics*. Cambridge University press.

Judy, J., Maynes, D., and B.W., W. (2007). Characterization of frictional pressure drop for liquid flow through micro-channels. *International Journal of Heat and Mass transfer*, 45:3477–3489.

King, R., Stansfield, W., and Mulligan, P. (2006). *A dictionary of genetics*. 7th ed. Oxford.

Kloppel, T., Popp, A., Kuttler, U., and Wall, W. (2011). Fluid–structure interaction for non-conforming interfaces based on a dual mortar formulation. *Computer Methods in Applied Mechanics and Engineering*, 200(45):3111–3126.

Komvopoulos, K. and Yan, W. (1997). A Ffractal analysis of stiction in microelectromechanical systems. *Journal of Tribology*, 119(3):391–40.

Lopez, J., Hansali, G., Le Bosse, J., and Mathia, T. (1994). Caracterisation fractale de la rugositeŕidimensionelle d'une surface. *Journal de Physique*, 4:2501–2219.

Lorenz, B. and Persson, B. (2009). Leak rate of seals: Comparison of theory with experiment. *Europhysics Letters*, 86:44006.

Lucchini, R., Cattarinuzzi, E., Gastaldi, D., Picenoni, D., Lorenzelli, L., and Vena, P. (2015). Buckling waves in aluminum on a polyimide sea: In situ analysis towards a reliable design strategy for stretchable electronics. *Materials Today*, 18:299–300.

Majumbdar, A. and Bhushan, A. (1990). Role of fractal geometry in roughness characterization and contact mechanics surfaces. *Journal of Tribology*, 112:205–216.

Majumbdar, A. and Bhushan, A. (1991). Fractal model of elasto-plastic contact between rough surfaces. *Journal of Tribology*, 113:1–11.

Malcai, O., Lidar, D., and Biham, O. (1997). Scaling range and cutoffs in empirical fractals. *Physical review E*, 56(3):2817–2828.

Mandelbrot, B. (1977). *Fractals: form, chance, and dimension.* W. H. Freeman, San-Francisco.

Mandelbrot, B. (1982). *The fractal geometry of nature*. W. H. Freeman, San-Francisco.

Mandelbrot, B. (1985). Self affinne fractals and fractal dimension. *Physica Scripta*, 32(4).

Mannners, W. and Greenwood, J. (2006). Some observations on Persson's diffusion theory of elastic contact. *Wear*, 261:600–610.

Matlab (2016). *version 9.0.0.341360 (R2016a)*. The MathWorks Inc., Natick, Massachusetts.

Moody, L. (1944). Friction factors for pipe flow. *Tansaction of the ASME*, 66:671–683.

Morag, Y. and Etsion, I. (2007). Resolving the contradiction of asperities plastic to elastic mode transition in current contact models of fractal rough surfaces. *Wear*, 262:624–629.

Muser, M., Dapp, W., Bugnicourt, R., Sainsot, P., Lesaffre, N., Lubrecht, T., Persson, B., Harris, K., Bennett, A., Schulze, K., Rohde, S., Ifju, P., Sawyer, W., Angelini, T., Esfahani, H., Kadkhodaei, M., Akbarzadeh, S., Wu, J., Vorlaufer, G., Vernes, A., Solhjoo, S., Vakis, A., Jackson, R., Xu, Y., Streator, J., Rostami, A., Dini, D., Medina, S., Carbone, G., Bottiglione, F., Afferrante, L., Monti, J., Pastewka, L., Robbins, M., and Greenwood, J. (2017). Meeting the Contact-Mechanics Challenge. *Tribology letters*, December:65–118.

Nayak, P. (1971). Random process model of rough surfaces. *Journal of Lubricated Technology*, 93:398–407.

Niederreiter, H. (1992). *Random Number Generation and Quasi-Monte Carlo Methods*. SIAM.

Noceda, J. and Wright, S. (2006). *Numerical Optimization*. Springer.

Nosonovsky, M. (2007). Multiscale roughness and stability of superhydrophobic biomimetic interfaces. *Langmuir*, 3157-3161(23).

Nosonovsky, M. and Bushan, B. (2008). *Multiscale dissipative mechanisms and hierarchical surfaces: friction, superhydrophobicity, and biomimetics*. Springer.

Paggi, M. and Barber, J. (2011). Contact conductance of rough surfaces composed of modified RMD patches. *International Journal of Heat and Mass Transfer,*, 54:4664–4672.

Paggi, M. and Ciavarella, M. (2010). The coefficient of proportionality k between real contact area and load, with new asperity models. *International Journal of Solids and Structures*, 56:1020–1029.

Paggi, M. and He, Q. (2015). Evaluation of the free volume between rough surfaces in contact. *Wear*, 05:336–337.

Paggi, M. and Reinoso, J. (2015). An anisotropic large displacement cohesive zone model for fibrillar and crazing interfaces. *International Journal of Solids and Structures*, 69–70:106–120.

Papautsky, I., Ameel, T., and Bruno Frazier, A. (2001). A review of laminar single-phase flow in microchannels. *International Mechanical Engineering Congress and Exposition*, 56.

Patir, N. and Cheng, H. (1978). An average flow model for determining effects of three-dimensional roughness on partial hydrodynamic lubrication. *Journal of Tribology*, 100:12–17.

Patir, N. and Cheng, H. (1979). Application of average flow model to lubrication between rough sliding surfaces. *Journal of Tribology*, 101:220–230.

Peitgen, H. and Saupe, D. (1988). *The Science of Fractal Images*. Springer-Verlag, New York.

Persson, B. (2001). Theory of rubber friction and contact mechanics. *Journal of Chemcal Physics*, 115:3840–3861.

Persson, B. (2014). On the Fractal Dimension of Rough Surfaces. *Tribology letter*, 54:99–106.

Pohrt, R. and Popov, V. (2014). Adhesive contact simulation of elastic solids using local mesh-dependent detachment criterion in Boundary Elements Method. *Mechanical Engineering*, 13(1):3–10.

Popov, V., Dimaki, A., Psakhie, S., and Popov, M. (2013). On the role of scales in contact mechanics and friction between elastomers and randomly self-affine surfaces. *Scientific Reports*, 5(11139).

Popp, A. (2012). *Mortar methods for computational contact mechanics*. PhD thesis, Universitätsbibliothek der TU München.

Popp, A., Gee, M., and Wall, W. (2009). A finite deformation mortar contact formulation using a primal–dual active set strategy. *Numerical methods in engineering*, 79(11):1354–1391.

Putignano, C., Afferrante, L., Bottiglione, F., Carbone, G., and Demelio, G. (2012a). A new efficient numerical method for contact mechanics of rough surfaces. *Journal of Solid and Structures*, 49:338–343.

Putignano, C., Afferrante, L., Carbone, G., and Demelio, G. (2012b). The influence of the statistical properties of self-affine surfaces in elastic contact: a numerical investigation. *Journal of Mechanics and Physics of Solids*, 60:973–982.

Putignano, C., Afferrante, L., Carbone, G., and Demelio, G. (2013). A multiscale analysis of elastic contact and percolation threshold fo numerically generated and real rough surfaces. *Tribology international*, 64:148–154.

Pérez-Ràfols, F., Larsson, R., and Almqvist, A. (2016a). Modelling of leakage on metal-to-metal seals. *Tribology international*, 94:421–427.

Pérez-Ràfols, F., Larsson, R., Lundstrom, S., Wall, P., and Almqvist, A. (2016b). A stochastic two-scale model for pressure-driven flow between rough surfaces. *Proceedings of the Royal Society A*, 472.

Reinoso, J., Blazquez, A., Estefani, A., Paris, F., Canas, J., Arevalo, E., and Cruz, F. (2012). Experimental and three-dimensional global-local finite element analysis of a composite component including degradation process at the interfaces. *Composites Part B: Engineering*, 43:1929–1942.

Reinoso, J., Paggi, M., and Rolfes, R. (2016). A computational framework for the interplay between delamination and wrinkling in functionally graded thermal barrier coatings. *Computational Material Science*, 116:82–95.

Ridley, M. (2006). *Genome: the autobiography of a species in 23 chapters*. New York: Harper Perennial.

Rubinstein, J. and Torquato, S. (1989). Flow in random porous media: mathematical formulation, variational principles, and rigorous bounds. *Journal of Fluid Mechanics*, 206:25–46.

Rubinstein, S., Cohen, G., and Fineberg, J. (2004). Detachment Fronts and the onset of friction. *Nature*, 430:1005–1009.

Sahlin, F., Almqvist, A., Larsson, R., and Glavatskikh, S. (2007). A Cavitation Algorithm for Arbitrary Lubricant Compressibility. *Tribology international*, 40:1294–1300.

Sahlin, F., Glavatskikh, S., Almqvist, A., and Larsson, R. (2005). Two-Dimensional CFD-Analysis of Micro-Patterned Surfaces in Hydrodynamic Lubrication. *Journal of Tribology*, 127:96–102.

Sahlin, F., Larsson, R., Marklund, P., Almqvist, A., and Lugt, P. (2010). A mixed lubrication model incorporating measured surface topography. Part 2: roughness treatment, model validation, and simulation. *Journal of engineering Tribology*, 224:353–366.

Sayles, R. and Thomas, T. (1978). Surface topography as a non stationary random process. *Nature*, 271:431–434.

Sherge, M. and Gorb, S. (2001). *Biological Micro- and Nano- Tribology & Nature's Solutions*. Springer, Berlin.

Solhjoo, A. and Vakis, A. (2015). Definition and detection of contact in atomistic simulations. *Computational Materials Science*, 109(November):172–182.

Song, H., Vakis, A., Liu, X., and der Giessen, V. (2017). Statistical models of rough surfaces contact for size-dependent plasticity and asperity interaction. *Journal of Applied Mechanics-Transactions of the Asme*, 81(4).

Svanberg, K. (1987). The method of moving asymptotes - a new method for structural optimization. *International Journal for Numerical Methods in Engineering*, 24:555–573.

Svanberg, K. (2002). A class of globally convergent optimization methods based on conservative convex separable approximations. *SIAM Journal on Optimization*, 12:555–573.

Svanberg, K. (2007). MMA and GCMMA – two methods for nonlinear optimization. Technical report, KTH, Stockholm, Sweden, 15 pages.

Taufik, M. and Jain, P. (2014). Role of build orientation in layered manufacturing: a review. *International Journal of Manufacturing Technology and Management*, 27(1/2/3):266–274.

Vakis, A. (2009). Dynamic Head-Disk interface instabilities with friction for light contact (surfing) recording. *IEEE Transaction on magnetics*, 45(4):10.

Vakis, A. (2014). Asperity interaction and substrate deformation in statistical summation models of contact between rough surfaces. *Journal of Applied Mechanics-Transactions of the ASME*, 81(4).

Vakis, A., Meijer, H., and Prins, W. (2014). First Steps in the Design and Construction of the Ocean Grazer. *ASME 2014 12th Biennial Conference on Engineering Systems Design and Analysis*, 2:V002T09A004.

Van Roij, M., Meijer, H., Prins, W., and Vakis, A. (2015). Experimental performance evaluation and validation of dynamical contact models of the Ocean Grazer. *OCEANS 2015 - Genova, IEEE Xplore*, pages 978–1–4799–8736–8.

Versteeg, H. and Malaskera, W. (1995). *An introduction to computational fluid dynamics. The finite volume method.* Longman Scientific and Technical.

Wang, L., Tomgren, M., and Onori, M. (2015). Current status and advancement of cyber-physical systems in manufacturing. *Journal of Manufacturing Systems*, 37(2):517–527.

Wang, S. and Komvopoulos, K. (1994a). A Fractal Theory of the Interfacial Temperature Distribution in the Slow Sliding Regime: Part I—Elastic Contact and Heat Transfer Analysis. *Journal of Tribology*, 116(4):812–822.

Wang, S. and Komvopoulos, K. (1994b). A Fractal Theory of the Interfacial Temperature Distribution in the Slow Sliding Regime: Part II—Multiple Domains, Elastoplastic Contacts and Applications. *Journal of Tribology*, 116(4):824–832.

Wendt, U., Stiebe-Lange, K., and Smid, M. (2002). On the influence of imaging conditions and algorithms on the quantification of surface topography. *Journal of Microscopy*, 207(3):169–179.

Whitaker, S. (1986). Flow in porous media I: a theoretical derivation of Darcy's Law. *International Journal of Solids and Structures*, 1:3–25.

Winkler, H. (1920). *Verbreitung und Ursache der Parthenogenesis im Pflanzen - und Tierreiche*. Verlag Fischer.

Wu, J. (2000). Simulation of rough surfaces with FFT. *Tribology international*, 33:47–58.

Wu, J. (2001). Structure function and spectral density of fractal pro®les. *Chaos, Solitons and Fractals*, 12:2481–2492.

Wu, J. and Yu, B. (2007). A fracteal resistance model for flow through porous media. *International Journal of Heat and Mass transfer*, 50:3925–3932.

Yan, W. and Komvopoulos, K. (1998). Contact analysis of elastic-plastic fractal surfaces. *Journal of Applied Physics*, 84(7):3617–3624.

Yastrebov, V. (2013). *Numerical methods in contact mechanics*. John Wiley & Sons.

Yastrebov, V., Anciaux, G., and Molinari, J. (2012). Contact between representative rough surfaces. *Physical review letter*, 86(3):035,601(R).

Yastrebov, V., Anciaux, G., and Molinari, J. (2015). From infinitesimal to full contact between rough surfaces: evolution of the contact area. *International Journal of Solids and Structures*, 52:83–102.

Yastrebov, V., Anciaux, G., and Molinari, J. (2017a). On the accurate computation of the true contact-area in mechanical contact of random rough surfaces. *Tribology international*, 114:161–171.

Yastrebov, V., Anciaux, G., Shvarts, A., Molinari, J., and Cailletaud, G. (2017b). Modeling creeping flow through a closed crack with a self-affine geometry and an extension to permeability of cracked media. *Poromechanics VI*.

Yin, B., Li, X., and Fu, Y. Yun, W. (2012). Effect of laser textured dimples on the lubrication performance of cylinder liner in diesel engine. *Lubrication Science*, 24:293–312.

Yu, B. and Cheng, P. (2002). A fractal permeability model for bi-dispersed porous media. *International Journal of Heat and Mass transfer*, 45:2983–2993.

Yu, B., Li, J., Li, Z., and Zou, M. (2003). Permeabilities of unsuturated fractal porous media. *Multiphase flow*, 29:1625–1642.

Zavarise, G., Borri-Brunetto, M., and Paggi, M. (2007). On the resolution dependence of micromechanical contact models. *Wear*, 262:42–54.

Zhao, H., Yu, Z., and Wadley, H. (2014). The influence of coating compliance on the delamination of thermal barrier coatings. *Surface Coating Technology*, 204:2432–2441.